Deceleration of Antiprotons for High-Efficiency Accumulation at PUMA

Entschleunigung von Antiprotonen für hocheffizientes Akkumulieren bei PUMA
Zur Erlangung des Grades eines Doktors der Naturwissenschaften (Dr. rer. nat.)
Genehmigte Dissertation von Jonas Ludwig Fischer aus Darmstadt
Tag der Einreichung: 16.04.2024, Tag der Prüfung: 15.05.2024

1. Gutachten: Prof. Dr. Alexandre Obertelli
2. Gutachten: Prof. Dr. Tetyana Galatyuk
Darmstadt, Technische Universität Darmstadt

TECHNISCHE
UNIVERSITÄT
DARMSTADT

Physics Department
Institut für Kernphysik
AG Obertelli

Deceleration of Antiprotons for High-Efficiency Accumulation at PUMA
Entschleunigung von Antiprotonen für hocheffizientes Akkumulieren bei PUMA

Accepted doctoral thesis by Jonas Ludwig Fischer

Date of submission: 16.04.2024
Date of thesis defense: 15.05.2024

Darmstadt, Technische Universität Darmstadt

Bitte zitieren Sie dieses Dokument als:
URN: urn:nbn:de:tuda-tuprints-273798
URL: http://tuprints.ulb.tu-darmstadt.de/27379
Jahr der Veröffentlichung auf TUprints: 2024

As I gaze out at the stars, I am struck by the fact that every speck of light we see represents a vast, complex system of matter and energy, held together by the laws of physics.

ChatGPT about antimatter in the style of Werner Herzog

Erklärungen laut Promotionsordnung

§ 8 Abs. 1 lit. c PromO

Ich versichere hiermit, dass die elektronische Version meiner Dissertation mit der schriftlichen Version übereinstimmt.

§ 8 Abs. 1 lit. d PromO

Ich versichere hiermit, dass zu einem vorherigen Zeitpunkt noch keine Promotion versucht wurde. In diesem Fall sind nähere Angaben über Zeitpunkt, Hochschule, Dissertationsthema und Ergebnis dieses Versuchs mitzuteilen.

§ 9 Abs. 1 PromO

Ich versichere hiermit, dass die vorliegende Dissertation selbstständig und nur unter Verwendung der angegebenen Quellen verfasst wurde.

§ 9 Abs. 2 PromO

Die Arbeit hat bisher noch nicht zu Prüfungszwecken gedient.

Darmstadt, 16.04.2024

J. Fischer

Abstract

The PUMA (antiProton Unstable Matter Annihilation) experiment at CERN seeks to determine the ratio of neutrons to protons in the nuclear density tail of stable and unstable isotopes, utilizing the ratio of annihilated neutrons and protons following the capture of low-energy antiprotons as a novel nuclear structure observable. The experiment relies on the efficient deceleration and accumulation of antiprotons in a Penning trap at CERN's ELENA (Extra-Low ENergy Antiproton) ring and on storage times sufficient for transport and experiments at the ISOLDE (Isotope Separation On-Line DEvice) facility.

The antiproton deceleration beamline and the cold field emission electron source designed, built and validated in this work are both used to control the kinetic energy of the antiprotons to allow for trapping and transport.

Antiprotons were used to validate the beamline at ELENA and decelerated with a pulsed drift tube from a kinetic energy of 100 keV to (3898 ± 3) eV, reaching a transmission of (55 ± 3)%. The standard deviation of the energy distribution is (127 ± 4) eV, putting 88% of the antiprotons in an energy range suitable for trapping. Careful consideration with regards to the vacuum compatibility of all materials and of vacuum pumps makes a pressure of less than 10^{-10} mbar at the end of the beamline possible, necessary to suppress annihilations of antiprotons with residual gas molecules.

In the PUMA experiment electrons will be co-trapped with antiprotons to provide cooling by Coulomb collisions, both after the initial trapping to reduce the antiproton's kinetic energy further as well as during plasma manipulation. The cold field emission electron source built for this purpose produces a current of around 100 nA with an extraction voltage of less than 1 kV. One is used in the PUMA test trap, and two more have been built for the installation in the PUMA Penning trap assembly.

Zusammenfassung

Das PUMA-Experiment (antiProton Unstable Matter Annihilation) am CERN zielt darauf ab, das Verhältnis von Neutronen zu Protonen im Kerndichteschweif von stabilen und instabilen Isotopen zu bestimmen. Dabei wird das Verhältnis von annihilierten Neutronen und Protonen nach dem Einfang von niederenergetischen Antiprotonen als neue Observable genutzt. Das Experiment beruht auf der effizienten Entschleunigung und Akkumulation von Antiprotonen in einer Penning-Falle am ELENA-Ring (Extra-Low ENergy Antiproton) des CERN und auf ausreichenden Speicherzeiten für den Transport und Experimente in der ISOLDE-Anlage (Isotope Separation On-Line DEvice).

Die Antiprotonen-Entschleunigung-Beamline und die Feldemissions-Elektronenquelle, die im Rahmen dieser Arbeit entworfen, gebaut und validiert wurden, dienen dazu, die kinetische Energie der Antiprotonen zu kontrollieren, um das Einfangen und den Transport zu ermöglichen.

Zur Validierung der Beamline bei ELENA wurden Antiprotonen verwendet, die mit einer gepulsten Driftröhre von einer kinetischen Energie von 100 keV auf (3898 ± 3) eV abgebremst wurden und dabei eine Transmission von (55 ± 3)% erreichten. Die Breite der Energieverteilung beträgt (127 ± 4) eV, womit 88% der Antiprotonen in einem für den Einfang geeigneten Energiebereich liegen. Sorgfältige Überlegungen zur Vakuumverträglichkeit der Materialien und der Vakuumpumpen ermöglichen einen Druck von weniger als 10^{-10} mbar am Ende der Beamline, der notwendig ist, um Annihilationen von Antiprotonen mit Restgasmolekülen zu unterdrücken.

Im PUMA-Experiment werden Elektronen zusammen mit Antiprotonen eingefangen, um Kühlung durch Coulomb-Kollisionen zu gewährleisten, sowohl direkt nach dem Einfang, um die kinetische Energie des Antiprotons weiter zu reduzieren, als auch während der Manipulation des Plasmas. Die für diesen Zweck gebaute Feldemissions-Elektronenquelle erzeugt einen Strom von etwa 100 nA bei einer Extraktionsspannung von weniger als 1 kV. Eine solche Quelle wird in der PUMA-Testfalle verwendet, und zwei weitere wurden für den Einbau in die PUMA-Penning-Falle gebaut.

Contents

1. Introduction

1.1. Nuclear Physics

The beauty of nuclear physics stems from the emergence of incredible complexity and diversity from very simple building blocks*. From only protons and neutrons thousands of nuclei can be formed, some stable, most of them unstable. As the simple rules of chess lead to a complex game, so does the nuclear interaction govern the nuclear properties. It is one of these properties, namely the neutron-proton asymmetry on the nuclear surface, to be measured by the PUMA collaboration, to which this work hopes to contribute.

Features of the nuclear and underlying nucleon-nucleon (NN) interaction have been extracted from nucleon-nucleon scattering experiments and studies of nuclear characteristics. At distances below about 0.5 fm, the NN interaction is strongly repulsive, manifesting in the small but non-zero size of nuclei. Above that, the potential is attractive, hence the existence bound systems of nucleons. Beyond 2 fm, the potential rapidly diminishes to zero. This characteristic can be inferred by examining the binding energy per nucleon across stable nuclei. The binding energy reaches 7 MeV per nucleon for ^{4}He, only slightly increasing to 8.8 MeV per nucleon for ^{62}Ni, and then slightly decreasing towards uranium [1]. This implies that the attractive part of the nuclear potential is within a range comparable to the size of the ^{4}He nucleus. Figure 1.1 shows the potential for the dominant $^1S_0$ partial wave as parameterized by Reid [2].

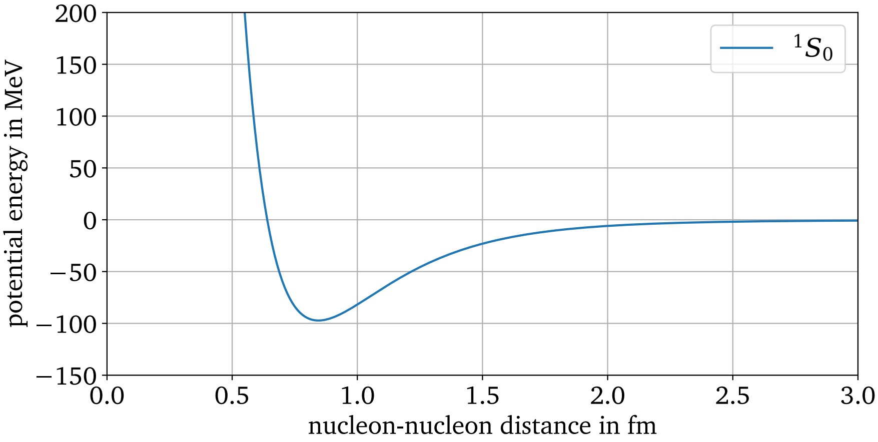

Figure 1.1.: Reid potential for the $^1S_0$ partial wave [2]. At distances below about 0.5 fm, the interaction is strongly repulsive. At larger distances, the potential is attractive and beyond 2 fm, the potential rapidly diminishes to zero.

In addition to this central interaction, a non-central tensor component, essential for the non-zero quadrupole moment of the deuteron [3], contributes. Further, a spin-orbit-coupling component explains

---

*In the author's humble opinion.

the observed polarization in NN scattering [4, 5]. From this, a simple two-body interaction potential

$$V_{\mathrm{NN}} = V_{\mathrm{C}} + V_{\mathrm{T}} + V_{\mathrm{LS}} \tag{1.1}$$

with the central part V_{C}, the tensor part V_{T} and the spin-orbit term V_{LS} can be derived. An example is the Paris potential [6], where spin-orbit term depends linearly on the relative momentum. In realistic NN potentials, meaning they reproduce scattering data and bound two- and three-body states, more terms and with quadratic dependencies are included, such as the Argonne-v18 potential [7]. The realistic potentials are grounded in the effective meson exchange model, assuming that the interaction between two nucleons is mediated by the exchange of massive mesons. It thereby restricts the effective range of the interaction, a concept first proposed by Yukawa [8]. For the description of different parts of the NN-interaction potential different mesons are used. Pions, the lightest mesons, dominate the long-range behavior of the central and tensor components, σ-mesons induce the attractive part between 0.5 fm and 2 fm, and heavier mesons contribute to short-range repulsion [9]. To reproduce measured energies of ground or low-lying excited states of light nuclei the aforementioned two-body potentials need to be expanded to include three-body interactions [10, 11].

A method to derive the interaction potentials including three- and more body interactions in a systematic manner is chiral effective field theory (ChEFT) [12, 13]. Here, pions and nucleons are considered as the relevant degrees of freedom and the interaction adopts the chiral symmetry from quantum chromodynamics (QCD). To get a perturbative theory from the non-perturbative QCD, the NN interaction potential is expanded in powers ν of $Q/\Lambda \ll 1$:

$$V_{\mathrm{NN}} = \sum_{\nu} \left(\frac{Q}{\Lambda}\right)^{\nu} f_{\nu}(Q, \Lambda). \tag{1.2}$$

The soft scale Q is typically set to an external momentum or the pion mass ($\sim$ 140 MeV) and the hard scale Λ (chiral symmetry breaking) is somewhat arbitrarily set between $\sim$ 350 MeV and 1 GeV [14, 15]. All contributing terms f_{ν} must be invariant under translation, change of reference frame, rotation, isospin rotation, parity transformation and time reversal. Additionally, it must obey chiral symmetry. The hierarchy of nuclear forces in ChEFT up to $\nu = 3$ are depicted in Fig. 1.2. For $\nu = 0$, the so-called leading order (LO), a contact term and one-pion exchange appear. The contact terms encompass the interactions not resolved by the theory and contribute to the short-range interaction. The one-pion term adds to the long-range part of the interaction. Terms of $\nu = 1$ are forbidden by time reversal and parity invariance, therefore the next-to-leading order (NLO) is $\nu = 2$. The new two-pion exchange terms contribute to the intermediate-range interaction. Also, their operator structure includes tensor and spin-orbit terms, therefore reproducing the essential terms for the description of the nuclear interaction potential. The N^{2}LO terms include the emergence of three-body forces, needed to accurately describe the intermediate range of the interaction, and at the level of N^{3}LO four-body terms emerge. With these terms the experimental data can be well reproduced [13].

Independent of the choice of potential, when describing a nucleus with $A > 2$, *i.e.*, other than a deuteron, one faces the difficulty of a many-body problem. The problem can be simplified by describing the propagation of one nucleon in the mean field created by the other nucleons. One widely used parametrization of the nuclear mean field is the Skyrme potential [16, 17]. An approximate solution to the many-body problem can be found with Hartree-Fock models, where the assumption is, that the wave function of the system can be approximated by one Slater determinant. This works well for closed-shell nuclei like ^{16}O, ^{40}Ca and ^{208}Pb [18], but for open-shell nuclei the correlations induced by the residual interaction of the unpaired nucleons need to be included to reproduce observables. These pairing correlations can be included by changing the zero-range interaction terms in the Skyrme potential to finite range terms as done by Gogny and solve it using the Hartree-Fock-Bogolyubov formalism [19].

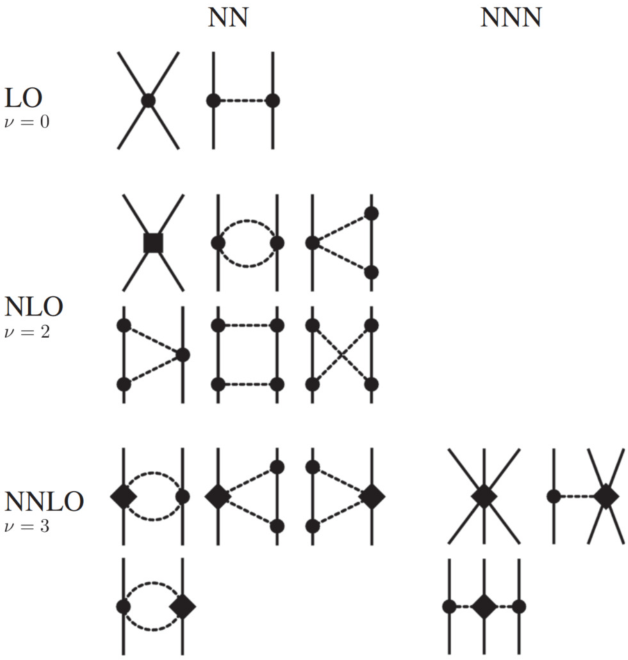

Figure 1.2.: Hierarchy of nuclear forces in ChEFT. Solid lines represent nucleons and dashed lines pions. Dots and diamonds denote interaction vertices. Figure from [20] under CC BY 3.0.

Nonetheless, a limitation of this phenomenological approach is the lack of a connection to any perturbation theory that enables the calculation of potential higher-order corrections, as well as the fact that uncertainties cannot be derived or propagated.

Methods that solve the nuclear many-body problem from first principles (underlying nucleon-nucleon interaction) are called *ab initio*. These methods solve the Schrödinger equation exactly, though only in the infinite limit. Still, this allows for a systematic treatment of uncertainties that come from the truncation necessary to have a computable problem. Ideally, ChEFT NN interactions are used, as their perturbative nature allows additional control over the uncertainties stemming from the interaction itself. Initially not feasible due to the high computational effort involved in these methods the last 20 years have seen great progress and the development of several different methods. Examples are coupled cluster models [21], the Green's function Monte Carlo method [22], many-body perturbation theory methods [23], the no-core shell model (NCSM) [24] and the variational Monte Carlo method [25]. These methods are usually limited by the available computational power to nuclei around $A \sim 20$, with an exception for magic nuclei, where even properties of ^{208}Pb have been calculated [26]. However, it is important to note that no model can fully describe the nucleus. For instance, models that accurately reproduce nuclear charge radii may not predict masses as accurately and vice versa.

From NN interactions and measured nuclear properties one can also construct a so-called nuclear equation of state (EoS) [27]. It gives the energy per nucleon E/A at a given density ρ for infinite nuclear matter. Because the NN interaction is short-ranged compared to the size of most nuclei, the EoS is a good approximation for the interior of nuclei, but also for the interior of neutron stars [28]. Figure 1.3 shows one possible parametrization of the EoS in the form of $\frac{E}{A}(\rho, \delta)$ from [29], depending on the asymmetry δ

which is defined as $\delta = (\rho_\mathrm{n} - \rho_\mathrm{p})/\rho$, with $\rho = \rho_\mathrm{n} + \rho_\mathrm{p}$, the sum of neutron and proton density. For $\delta = 0$ (nuclear matter) the EoS has a minimum at the saturation density $\rho_0 = 0.16\,\mathrm{fm}^{-3}$.

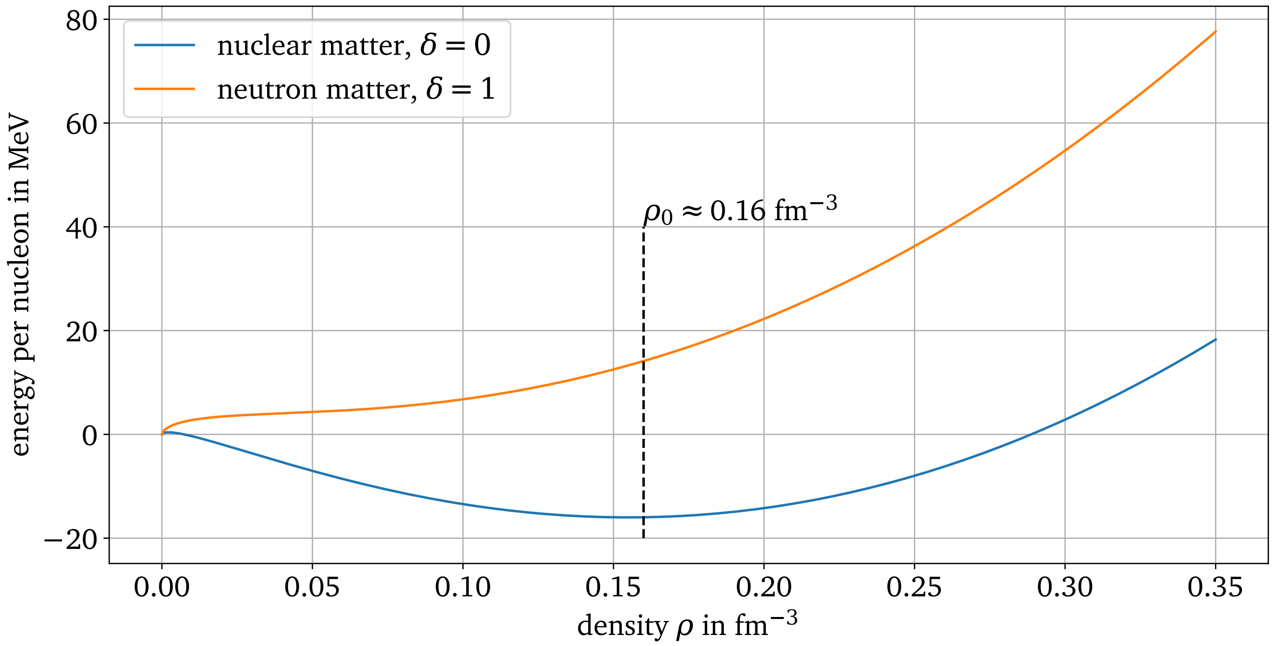

Figure 1.3.: Equation of state as parameterized by [29]. The asymmetry δ is defined as $\delta = (\rho_\mathrm{n} - \rho_\mathrm{p})/\rho$, with $\rho = \rho_\mathrm{n} + \rho_\mathrm{p}$, the sum of neutron and proton density. $\delta = 0$ denotes equal fractions of neutron and protons, as found in nuclear matter. For $\delta = 0$, the EoS has a minimum at the saturation density $\rho_0 = 0.16\,\mathrm{fm}^{-3}$.

For $\delta = 1$ (pure neutron matter), the energy per nucleon increases with increasing density. In a neutron star, this causes an outwards pressure that is in balance with gravity and prevents neutron stars from collapsing into black holes. The pressure is given by

$$P(\rho) = \rho^2 \frac{\partial(E/A)}{\partial\rho} \tag{1.3}$$

$$P(\rho_0, \delta = 1) = \frac{\rho_0}{3} L. \tag{1.4}$$

The L parameter, among others, is often used to characterize different parametrizations of the EoS, as it is proportional to the slope at saturation density and asymmetry equal 1. As it is also proportional to the pressure produced by the nucleons pushing against gravity, its value governs the size of neutron stars. Parametrization of the EoS constraining those parameters is an active area of research including theoretical calculations [30–32] and terrestrial experiments [33], as well as astrophysical observables such as supernovae [34], neutron star radii and masses [35–37], and gravitational waves from neutron star mergers [38].

In the nucleus, the EoS governs the distribution of neutrons and protons. In nuclei with neutron excess, and therefore an asymmetry $\delta > 0$, the neutron density increases slightly over that of the protons in the core of the nucleus. Also, at the surface of the nucleus, the neutron distribution extends to larger radii, leading to a layer of mostly neutrons, characterized by the neutron skin thickness

$$\Delta r_{\mathrm{np}} = \langle r_{\mathrm{n}}^2\rangle^{1/2} - \langle r_{\mathrm{p}}^2\rangle^{1/2}, \text{ with} \tag{1.5}$$

$$\langle r^2\rangle^{1/2} = \sqrt{\int r^2 \rho\left(\vec{r}\right)\, \mathrm{d}^3\vec{r}}, \tag{1.6}$$

the difference of the root-mean-square (rms) radii of the nucleon distributions. The neutron and proton distribution of ^{208}Pb and the corresponding rms radii and neutron skin thickness are shown in the left panel of Fig. 1.4. Remarkably, the neutron skin thickness correlates linearly with the L parameter, as demonstrated in the right panel of Fig. 1.4. A precise determination this property of ^{208}Pb therefore allows to constrain the L parameter in the equation of state, in turn putting tighter constrains on the physics of neutron stars, connecting two extremes of the universe via the nuclear force.

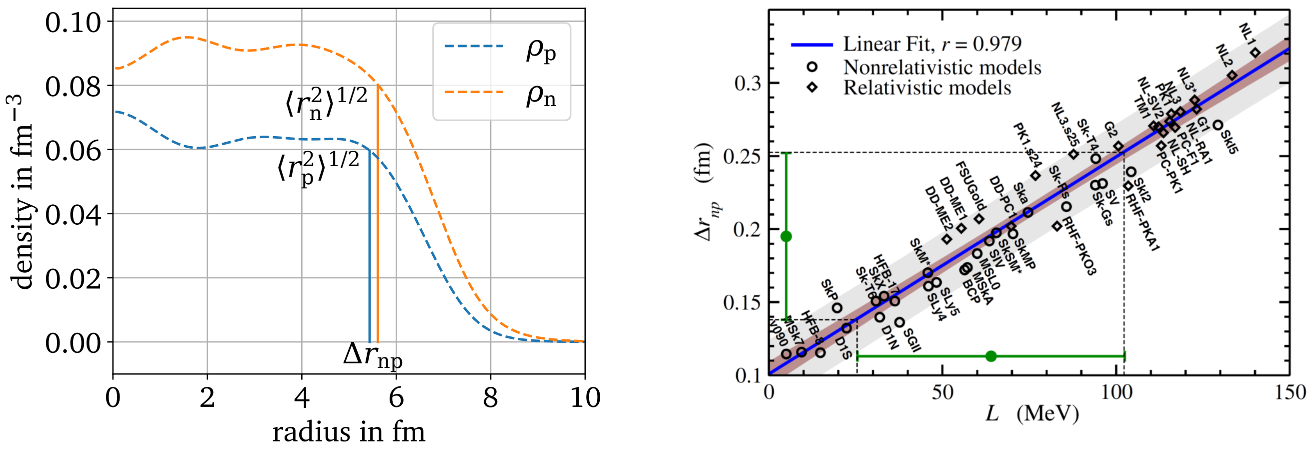

Figure 1.4.: Left: the proton and neutron density of ^{208}Pb calculated with the SKM interaction at the mean field level. The rms radii are calculated from $\langle r^2\rangle = \frac{1}{N}\int r^2\rho(r)4\pi r^2\,\mathrm{d}r$, with $N = \int \rho(r)4\pi r^2\,\mathrm{d}r$. From this calculation, the neutron skin thickness is $\Delta r_{\mathrm{np}} = 0.17\,\mathrm{fm}$. Right: Neutron skin thickness of ^{208}Pb against L parameter. Reprinted figure with permission from [39] Copyright 2011 by the American Physical Society.

The neutron skin thickness can be determined from the calculated rms radii of measured nuclear density distributions or from directly measured rms radii. The next section gives an overview of the methods employed for their determination.

1.2. Nuclear Density Distributions

1.2.1. Charge Distributions

The distribution of charges inside the nucleus can be seen as equivalent to the distribution of protons, since neutrons carry no electric charge. For stable nuclei, it can be measured with high precision by electron Coulomb scattering [40, 41], and with little interference from the neutrons interacting via the weak interaction. With an incident electron momentum between 200 and 800 MeV/c, the electron probes the structure of the nucleus with minimal inelastic scattering. From the experimental cross section the charge distribution ρ_c can be extracted in the following way. The experimental cross section is split into two parts

$$\left(\frac{\mathrm{d}\sigma}{\mathrm{d}\Omega}\right)_{\mathrm{exp}} = \left(\frac{\mathrm{d}\sigma}{\mathrm{d}\Omega}\right)_{\mathrm{Mott}} \cdot \left|F_c\left(\vec{q}^2\right)\right|^2, \tag{1.7}$$

where the Mott cross section that assumes a point-like nucleus is modified by a form factor

$$F_c\left(\vec{q}^2\right) = \int \rho_c\left(\vec{r}\right) \mathrm{e}^{i\vec{q}\vec{r}}\, \mathrm{d}^3\vec{r} \tag{1.8}$$

due to the internal charge distribution. Note that this is the (inverse) Fourier transform of the charge distribution. Figure 1.5 depicts the form factors and corresponding charge distributions, with examples. An experimental cross sections for ^{208}Pb is shown in Fig. 1.6.

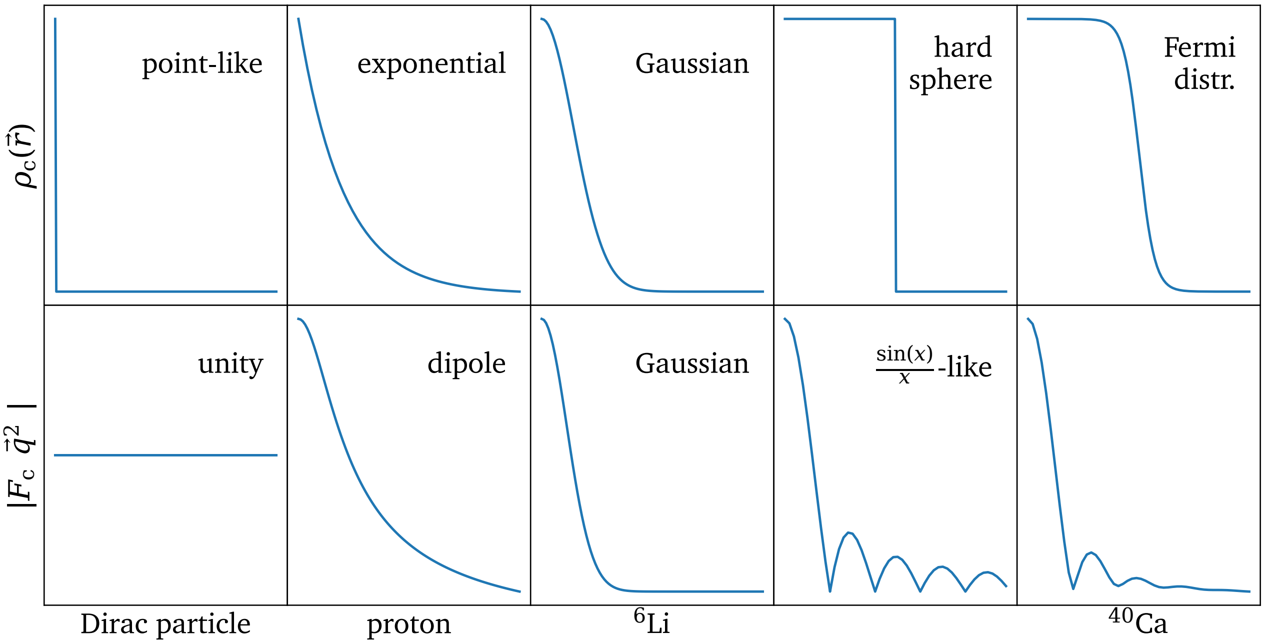

Figure 1.5.: Different charge distributions and corresponding form factors (Fourier transform) are shown. The form factors are calculated from experimentally measured electron-scattering cross-sections.

So far, this technique could only be applied to stable nuclei due to the need for a target. The self-confining radioactive-isotope (RI) ion target (SCRIT) plans to tackle this problem [42]. Unstable nuclei are trapped in an electron storage ring, longitudinally by confining electrodes and radially by the electron beam itself. This way, a high luminosity can be achieved with a relatively low number of ions, and the charge distribution of unstable nuclei can be measured.

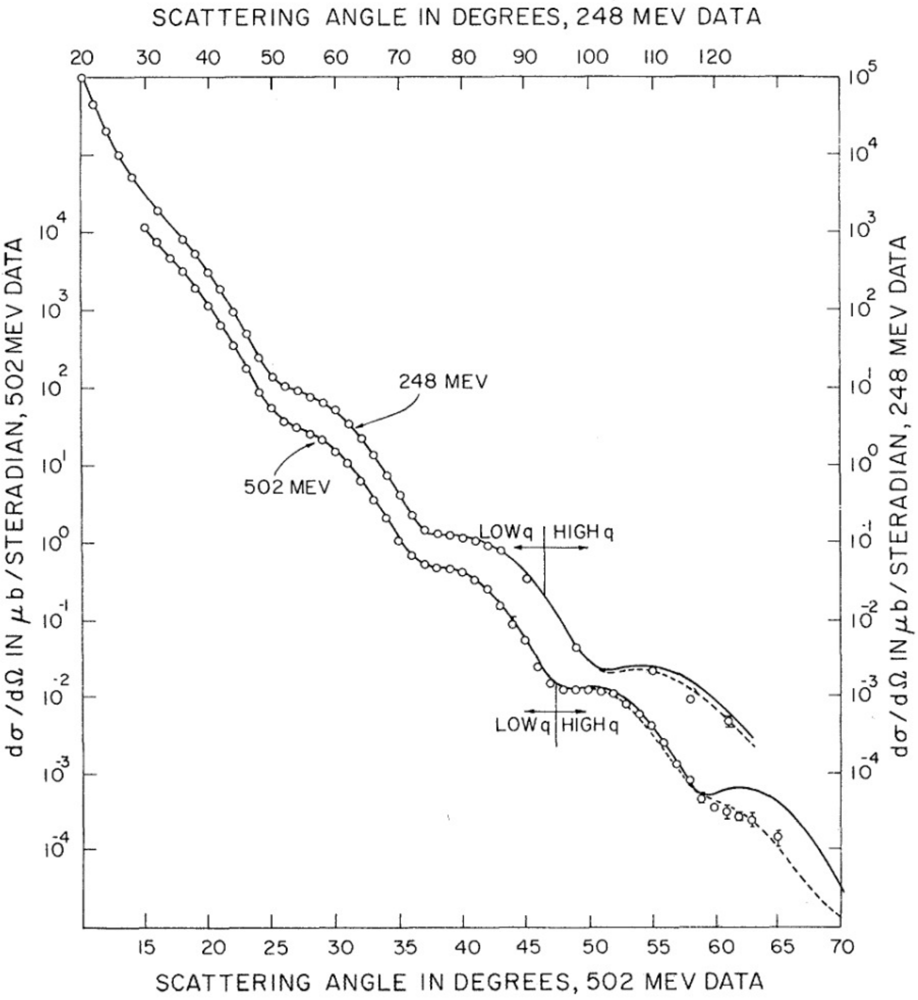

Figure 1.6.: Experimental elastic electron scattering cross sections of ^{208}Pb for beam energies of 248.2 and 502.0 MeV (circles) compared to theoretical cross sections (lines). Note the logarithmic scale on the ordinate. The distribution resembles the one of ^{40}Ca in Fig. 1.5. Reprinted figure with permission from [40] Copyright 1969 by the American Physical Society.

Currently, only moments of the charge distribution of short-lived nuclei, not the whole distribution are accessible experimentally, such as the root mean square (rms) radius as the defined as the square root of the second moment of the density distribution (see Eq. 1.6). The rms radius of the charge distribution can be measured with laser spectroscopy [43–45]. Shifts in the hyperfine transition frequencies compared to stable isotopes are measured, from which the rms charge radius can be calculated. The difference between the mean-square charge radii of two isotopes A and A'

$$\delta \left\langle r_{\mathrm{c}}^2 \right\rangle^{A,A'} = \left\langle r_{\mathrm{c}}^2 \right\rangle^{A'} - \left\langle r_{\mathrm{c}}^2 \right\rangle^{A}, \tag{1.9}$$

is related to the shift in hyperfine transition frequencies like

$$\delta\nu_{\mathrm{IS}}^{A,A'} = \nu^{A'} - \nu^{A} = K_{\mathrm{MS}} \cdot \frac{M_{A'} - M_A}{(M_A + m_{\mathrm{e}})(M_{A'} + m_{\mathrm{e}})} + F \cdot \delta \left\langle r_{\mathrm{c}}^2 \right\rangle^{A,A'}. \tag{1.10}$$

The shift arises from two contributions, the mass shift (different nuclear masses of the isotopes) and the volume of field shift (different nuclear volumes). A larger charge radius decreases the potential inside the nucleus, thereby shifting the lower levels up more than the higher ones, decreasing the transition energy. The shifts in transition frequencies caused by the change in nuclear volume (by varying the number of neutrons in Ni isotopes) are shown in Fig. 1.7. They correspond to a variation of the nuclear charge radius of 0.04 to 0.08 fm compared to ^{60}Ni. The mass shift constant K_{MS} and the field shift constant F must be known to a high precision to allow for the determination of the charge radius. Therein lies one of the difficulties of the method.

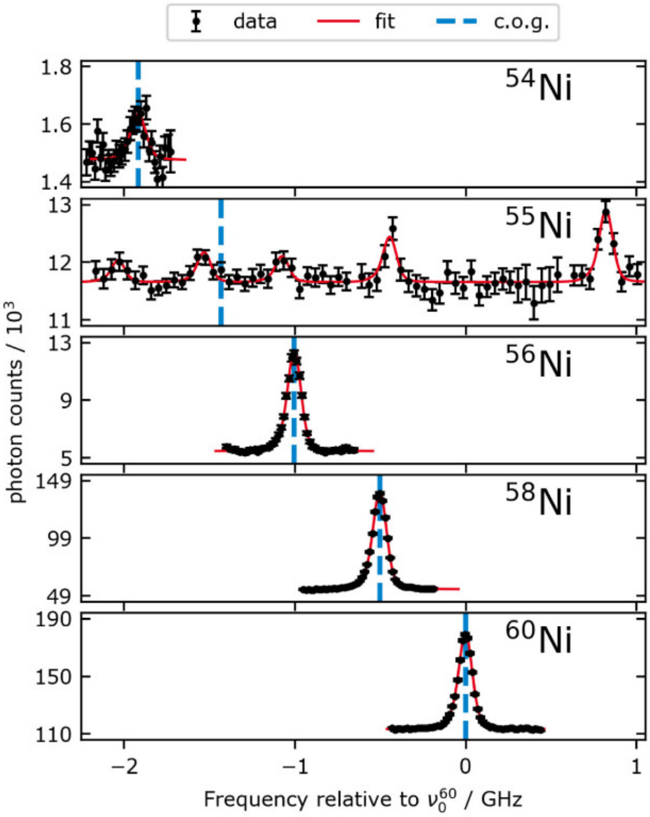

Figure 1.7.: The shifts in transition frequencies caused by the change in nuclear volume, by varying the number of neutrons. From the measurement of this shift, the rms charge radius can be extracted. Reprinted figure with permission from [46] Copyright 2022 by the American Physical Society.

By replacing an atomic electron with the heavier muon one can produce what is called an exotic atom to investigate the nucleus. Due to the lifetime of the muon in the order of 2 µs, only stable nuclei are investigated. Because of its greater mass compared to the electron, the overlap with the nucleus is greater and therefore more sensitive to the nuclear structure. Also, the transitions are shifted to laser-accessible frequencies allowing for high precision measurements of nuclear charge radii [47–49]. The spectroscopy of muonic X-rays also provides information on the structure of the nucleus. The X-rays are produced by the cascade of the muon towards the nucleus after capture. Because the spectroscopy does not rely on laser-accessible transitions, it was used on the majority of stable nuclei [50]. It should be noted here, that the X-ray spectroscopy does not allow for a model-independent extraction of the rms charge radius, as opposed to the laser spectroscopy. More detail on nuclear charge radii can be found in [51].

1.2.2. Neutron and Matter Distributions

Elastic electron scattering can not only be used to measure the distribution of protons but also of neutrons [39, 52–54]. Because the contribution to the weak charge of a nucleus is -0.989 per neutron compared to 0.071 per proton [55], the weak interaction couples mostly to the neutrons. Unfortunately for this measurement, the electromagnetic interaction dominates the cross section, but due to the parity-violating nature of the weak interaction an asymmetry in the cross sections can be observed when scattering electrons with forward (f) and backward (b) helicity

$$A_{\mathrm{PV}} = \frac{\sigma_{\mathrm{f}} - \sigma_{\mathrm{b}}}{\sigma_{\mathrm{f}} + \sigma_{\mathrm{b}}}, \tag{1.11}$$

with the scattering cross section σ_{f} and σ_{b} of longitudinally polarized electrons. The asymmetry is proportional to the weak form factor F_{w}, which in turn is the inverse Fourier transform of the weak density (see Eq. 1.8)

$$A_{\mathrm{PV}} \approx \frac{1}{4\sqrt{2}\pi} \frac{G_{\mathrm{F}}}{\alpha} \frac{|Q_{\mathrm{w}}|}{Z} \frac{F_{\mathrm{w}}\left(\vec{q}^{2}\right)}{F_{\mathrm{c}}\left(\vec{q}^{2}\right)} \vec{q}^{2}, \tag{1.12}$$

where G_{F} and α are the Fermi coupling and the fine-structure constant, Q_{W} and Z are the weak and electric charge of the target nucleus, respectively. The PREX-2 experiment has measured the asymmetry for a scattering angle of 5° on ^{208}Pb and determined $A_{\mathrm{PV}} = 550 \pm 16(\mathrm{stat.}) \pm 8(\mathrm{syst.})$ parts per billion [56]. Even though only one single momentum transfer $\vec{q}^{2}$ was measured, and therefore the full distribution cannot be extracted, the rms radius can be estimated because of the linear dependence of the rms radius on the asymmetry (see Fig. 1.8). The rms radius of the weak charge distribution ($\approx$ neutron distribution) in ^{208}Pb from this measurement is $R_{\mathrm{w}} = 5.8\,\mathrm{fm}$, compared to $R_{\mathrm{ch}} = 5.5\,\mathrm{fm}$ of the electric charges (= proton distribution).

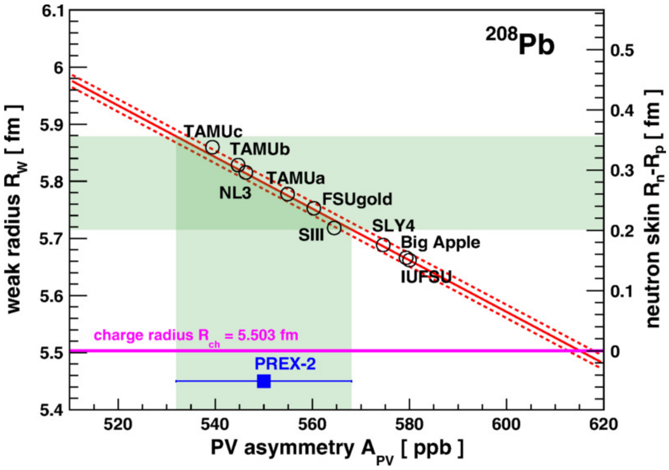

Figure 1.8.: Extraction of the weak radius (left vertical axis) or neutron skin (right vertical axis) for the ^{208}Pb nucleus. R_{ch} [57] is shown for comparison. Reprinted figure with permission from [56] Copyright 2021 by the American Physical Society.

For elastic scattering with protons, at intermediate energies in the range of tens to hundreds of MeV, the dominant influence on the scattering process is the strong interaction [58–61]. Because the strong interaction is isospin-independent, the overall nuclear matter distribution, rather than the weak or electric charge distribution, is probed. Then, it is simply a matter of subtracting the charge distribution (see

Subsec. 1.2.1) to obtain the neutron distribution. The primary source of uncertainties in this approach comes from the optical potentials used to model the strong interaction.

Coherent π^0 photoproduction also probes the matter distribution of the whole nucleus. The incoming photon of 200 to 300 MeV excites a collective Δ resonance in the nucleus. This resonance decays into a π^0. Because the excitation energy of the Δ resonance of neutron and proton are identical in the energy range of the photon [62], the nucleus as a whole contributes to the reaction. The measured cross sections can be reproduced with optical potentials and the matter distribution is determined from the form factor in the same way as for the elastic proton scattering. It has been argued that this method is not sensitive to isovector properties, such as the neutron skin thickness, but only the isoscalar matter distribution [63].

1.2.3. On the Outskirts of the Nuclear Distributions

With the above mentioned methods, one can determine the rms radii of the proton and neutron distribution, whose difference defines the neutron skin thickness Δr_{np}. Neutron skins occur in virtually any nucleus with an excess of neutrons, in the range of up to 0.4 fm in light neutron-rich nuclei [64, 65].

In heavy nuclei, the most well-studied isotope is ^{208}Pb with a neutron skin thickness of around 0.2 fm, with an uncertainty of about 0.05 fm, depending on the measurement method (see Fig. 1.9) [26, 56, 66–70]. As argued in the previous section, this quantity is relevant to probe neutron matter due to its pronounced neutron-to-proton asymmetry (see Fig. 1.4).

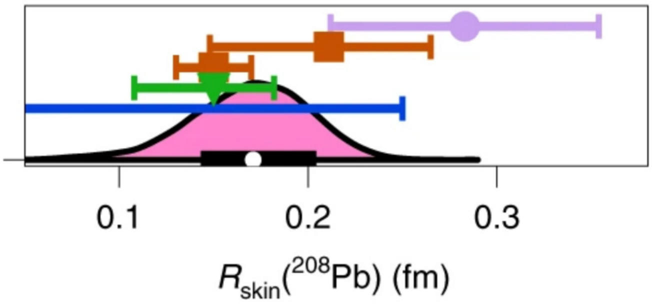

Figure 1.9.: Ab initio prediction for $R_{\text{skin}}(^{208}\text{Pb})$ [26] compared to experimental results using electroweak [56] (purple), hadronic [67, 71] (red), electromagnetic [66] (green) and gravitational wave [72] (blue) probes. Figure from [26] under CC BY 4.0.

Moving away from stability and towards the driplines, beyond which an additional nucleon no longer leads to a bound system, measurements of the interaction cross section can reveal a matter radius significantly larger than that of other nuclei along the isotopic chain. This phenomenon was initially observed by Tanihata et al. [73]. It was discovered that the determined rms matter radius of ^{11}Li (3.3 fm) is approximately 0.8 fm larger than the matter radii of ^{6,7,8,9}Li, while the charge radius of the Li isotopic chain remains mostly constant at around 2.5 fm. The difference in matter and charge radius of ^{11}Li is interpreted as a two-neutron halo. Here, two neutrons are weakly bound to the ^{9}Li core, with a separation energy of only 0.3 MeV, leading to a large spacial extension of the two halo neutron wave functions. ^{11}Li as also what is called a Borromean nucleus, because removing one of the constituents leaves an unbound system: removing a neutron results in the unbound ^{10}Li, and removing the ^{9}Li core would produce an unbound dineutron.

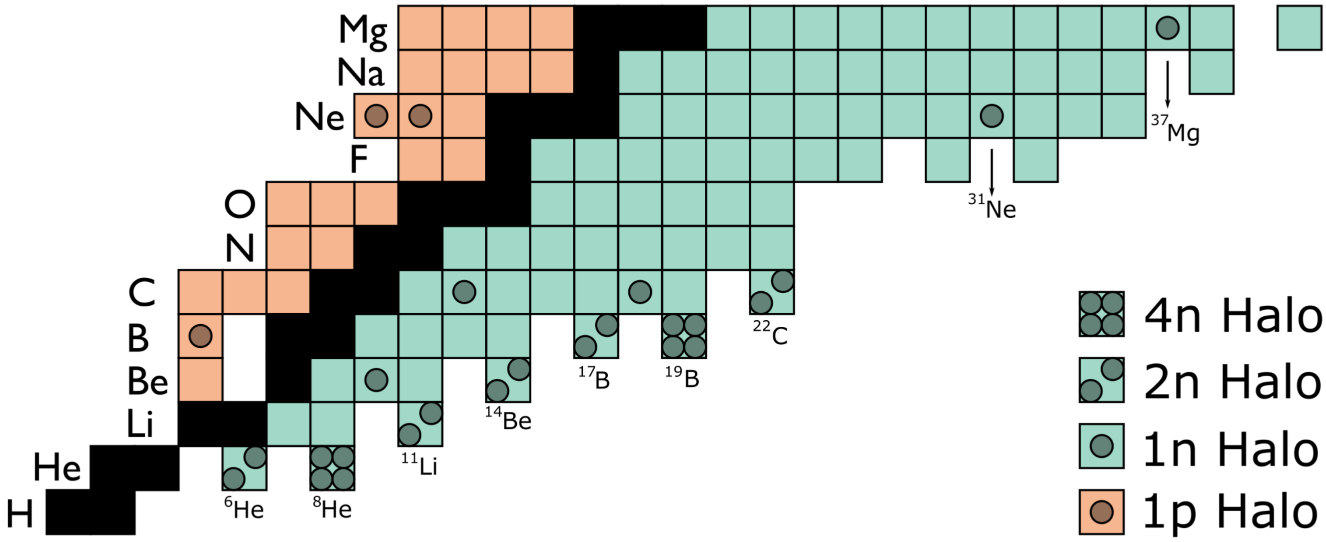

Figure 1.10.: Low-mass region of the nuclear chart. Isotopes marked with a circle correspond to nuclei which show indications of a proton or a neutron halo. While few of the highlighted nuclei have been extensively studied, several of them have been claimed to be halo candidates based on limited experimental evidence. Figure from [74] under CC BY 4.0.

Since the first neutron halo nucleus ^{11}Li, others have been observed in light nuclei and there are indications for more in medium-mass nuclei [75–78] (see Fig. 1.10). Analogous to neutron halos, proton halos require an excess of protons to populate states with very small single-particle energies. In contrast, proton halos are suppressed compared to neutron halos due to the additional Coulomb barrier, inhibiting loose binding of protons to a core. This confines possible proton halo nuclei to the very light and neutron-deficient region of the nuclear chart. An example is ^{8}B, where the matter distribution indicates a proton halo [79], although the rms charge radius remains to be measured [80].

Theoretical descriptions of halo nuclei can be accomplished within the framework of a halo effective field theory (EFT) [81]. In this approach the core is considered structure-less in leading order, and the nucleus is treated as a few-body system of the core and valence nucleons. Similarly, ab initio approaches can be applied to halo nuclei [82], offering complementary information to the halo EFT.

Both nuclear halos and neutron skins manifest in the density tails of nuclei with significant proton-to-neutron asymmetry. Their investigation through experiments proves challenging due to the elusiveness of neutrons, and, for halos, due to the short lifetimes and low production rates near the driplines. Simultaneously, nuclear theory, focused on the description of the nuclear core, encounters difficulties in providing consistent predictions due to a lack of precise and diverse data for fitting the free parameters of models. More, and more precise measurements of properties relating to the outskirts of the nuclear density distributions are essential to establish accurate references for nuclear theory.

1.3. Antiprotonic Atoms

Antiprotons offer an additional way to investigate nuclear density distributions [69, 71]. Due to their negative charge it is possible to form antiprotonic atoms. Here, an antiproton is bound to the nucleus due the electromagnetic force, in the same way an electron is in a normal atom or a muon is in a muonic atom. Antiprotonic atoms can be produced when antiprotons interact with atoms or ions at low relative momentum. The antiproton loses energy through collisions with atomic electrons and if the antiproton's energy is sufficiently low, it can be captured by knocking out one or more atomic electron. The capture cross section is predicted to be in the order of 10^6 barn for center-of-mass energies in the order of $10\,\mathrm{eV}$ [83]. This capture typically occurs in an antiprotonic orbital at about distances of the outermost electron shell. Due to energy and momentum conservation the principal quantum number of the antiprotonic orbital is $n_{\bar{\mathrm{p}}} \approx n_{\mathrm{e}} \sqrt{\frac{m_{\bar{\mathrm{p}}}}{m_{\mathrm{e}}}}$, where n_{e} is the principal quantum number of the knocked-out electron, m_{e} is the electron mass, and $m_{\bar{\mathrm{p}}}$ is the antiproton mass [84]. After the capture, the antiproton undergoes deexcitation by radiative electric dipole transitions ($\Delta n = 1,\ \Delta l = \pm 1$) and Auger transitions [84, 85]. As long as there are electrons left and there is an overlap of the orbitals Auger transitions dominate. Once the antiproton passes the last electron shell ($n_{\bar{\mathrm{p}}} \approx 42$), only X-ray transitions are possible. A schematic representation can be seen in Fig. 1.11.

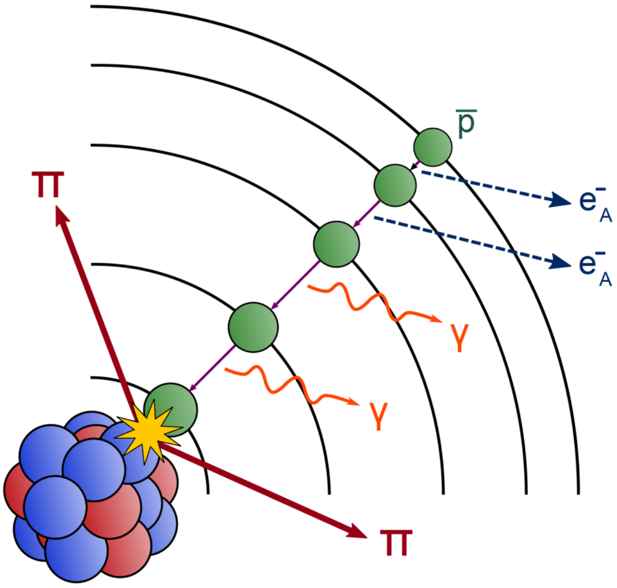

Figure 1.11.: Schematic depiction of the antiprotonic cascade and annihilation following the production of an antiprotonic atom. Figure from [86] under CC BY 4.0.

Due to the contracted radial wave functions ($m_{\bar{\mathrm{p}}} \gg m_{\mathrm{e}}$), the antiproton orbitals overlap significantly with the nuclear wave function for principal quantum numbers $n_{\bar{\mathrm{p}}} \approx 2 \ldots 9$. The proximity of the antiproton to the nucleus induces shifts and broadening in the transition frequency caused by the strong interaction for low-lying transitions with very small overlap [87, 88]. These shifts, compared to pure EM transitions, are be utilized to deduce properties of the p̄N interaction. The annihilation, due to the antiparticle nature of the antiproton, is characterized by an imaginary part of the optical potential. Moreover, the interaction is highly localized to the nuclear periphery with weak sensitivity to the nucleus' core [89–92].

As the overlap between the antiprotonic and nuclear wavefunctions increases, so does the annihilation probability and only a few percent of the antiprotons reach the lowest orbitals [93].

Knowing the orbital where the annihilation occurs, for example from X-ray measurements, one can calculate the annihilation probability density as a function of the radius [94]

$$f(r) \propto \rho(r)_{\mathrm{p,n}} \left|R_{nl}(r)\right|^2 , \tag{1.13}$$

with R_{nl} being the radial part of the solution to the Schödinger equation of the hydrogen atom, adjusted for the antiproton mass

$$\Psi_{nlm}(r,\theta,\phi) = R_{nl}(r)Y_{lm}(\theta,\phi), \tag{1.14}$$

with $l = n-1$ for circular states, being the most populated. Figure 1.12 shows the annihilation probability density for ^{208}Pb. The mean radius of the annihilation is roughly 2 fm from the half-density radius of the matter distribution, making antiprotonic atoms a tool to probe the density distributions very peripherally.

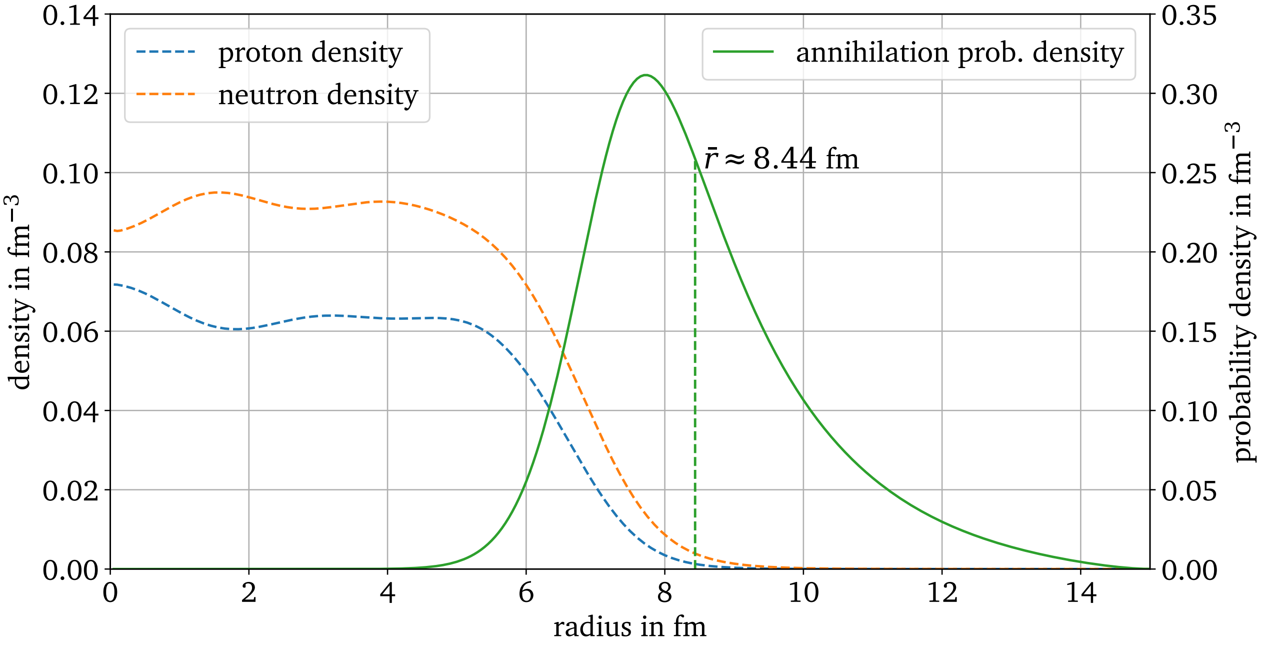

Figure 1.12.: Annihilation probability density for ^{208}Pb. The neutron and proton radius are calculated with the SKM interaction. The annihilation orbitals are $n = 10$ (30%) and $n = 9$ (70%) [69]. $\mathrm{Im}a_\mathrm{n}/\mathrm{Im}a_\mathrm{p}$ taken from [95]. For ease of readability $g(r) = \frac{r^2\rho(r)|R_{nl}(r)|^2}{\int r^2\rho(r)|R_{nl}(r)|^2\,\mathrm{d}r}$ is plotted, so that $\int g(r)\,\mathrm{d}r = 1$.

In the annihilation of the antiproton with either a proton or a neutron, the produced energy is converted into light mesons and their kinetic energy, most of them pions. The total charge of the initial particles is conserved and therefore by measuring the charge of all pions produced (Σ), one can determine whether the annihilation happened with a neutron ($\Sigma = -1$) or a proton ($\Sigma = 0$), this way determining the neutron-to-proton ratio at the nuclear surface.

One of the first experiments to utilize this was an experiment by Bugg et al. [95]. They detected charged pions coming from the annihilation of antiprotons stopped in solid targets made of copper, titanium, tantalum and lead within a hydrogen bubble chamber. For ^{208}Pb, they found that annihilation with a neutron is 2.27 times more likely than with a proton, while the ratio of neutrons to protons in the nucleus is $N/Z \approx 1.54$. The annihilation with a proton or neutron are not equally likely, characterized by unequal imaginary parts in the scattering length, $\mathrm{Im}a_\mathrm{n}/\mathrm{Im}a_\mathrm{p} \neq 1$. They determined this ratio to be 0.632 from a measurement on carbon ($N = Z$). With this the neutron-to-proton ratio in the low-density tail at $\rho < 0.2\rho_0$ is 3.59 for ^{208}Pb.

From 1982 to 1996, the Low Energy Antiproton Ring (LEAR) at CERN was used for experiments involving low-energy antiprotons, with a minimum kinetic energy of approximately 5.3 MeV. During this period, studies on antiproton scattering on hydrogen [96–98] and deuterium [99, 100], as well as investigations into the potential existence of a bound antiproton-proton baryonium atom [101], were conducted. A dedicated series of experiments aimed to explore properties of antiprotonic atoms [69, 71, 102–107].

In the first set of experiments on antiprotonic atoms, the focus was on detecting antiprotonic X-rays emitted in the cascade, particularly the last detectable X-rays before absorption [69, 102, 103, 107]. The shifts induced by the strong interaction on low-lying transitions (compared to only considering the electromagnetic interaction) were used to estimate the neutron skin thickness for various stable nuclei [107]. An antiproton optical interaction potential $V_{\text{opt}} = \bar{a}(\rho_{\text{p}} + \rho_{\text{n}})$ with a complex isospin-independent antiproton scattering length $\bar{a} = 2.5 + 3.4i$ and a simplifying two-parameter Fermi distribution for both neutron and proton density were used. The result is an approximately linear increase of the neutron skin thickness with the neutron-to-proton asymmetry $\delta = (N-Z)/A$ (see Fig. 1.13), consistent with theoretical predictions from HFB models [107], although the large uncertainties detract from the significance of this linear increase.

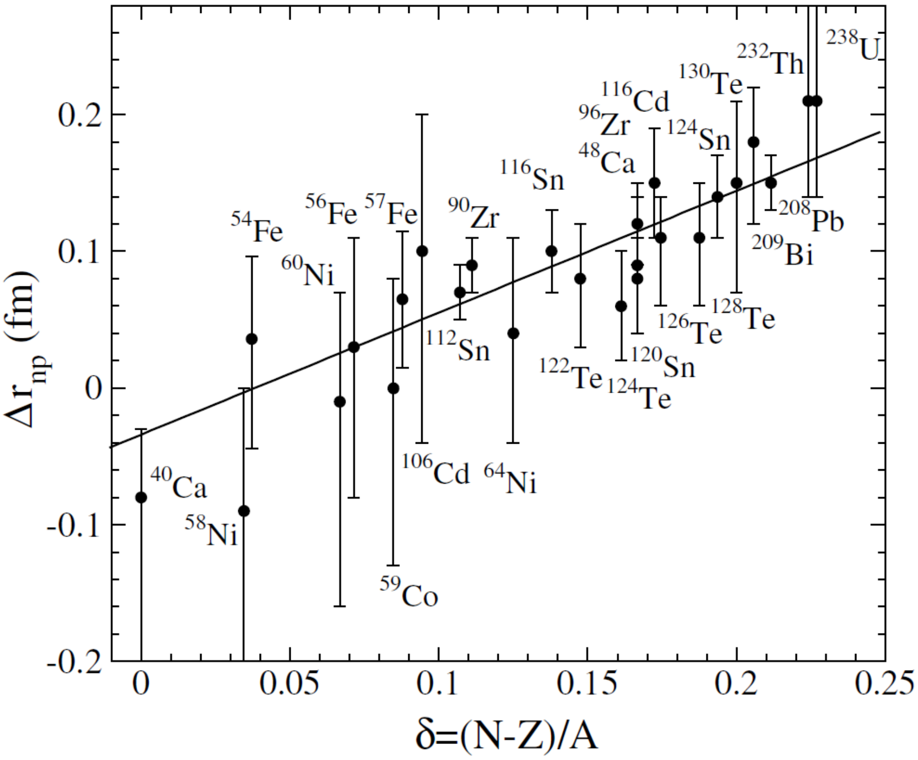

Figure 1.13.: Neutron skin thickness as deduced from antiprotonic atom X-ray data, as a function of $\delta = (N - Z)/A$. Reprinted from [107], Copyright 2004, with permission from Elsevier.

In the second set of experiments on antiprotonic atoms the residual nucleus following annihilation was studied [71, 105]. A particular focus was set on residuals with either one neutron or one proton less than the target. These nuclei are assumed to be produced in ultra-peripheral annihilations, where no pions interact with the residual nucleus. The relative yield of the one-less-neutron and one-less-proton nuclei is sensitive to the neutron-to-proton ratio in the nuclear density tail. Measurements on ^{232}Th indicated a neutron halo, as the yield of ^{231}Th was about 8 times higher than the yield of ^{231}Ac.

1.4. The PUMA Experiment

While the aforementioned experimental approaches provide valuable insights into the antiproton-nucleus interaction potential and the structure of nuclei, they are conceptually limited to stable targets. To gain additional insights into the properties of low-density asymmetric nuclear matter, particularly in short-lived nuclei with high asymmetry, the determination of the neutron-to-proton ratio on the nuclear surface is a useful observable. Moving to more exotic nuclei also allows the investigation of more pronounced neutron skins or nucleonic halos. The antiProton Unstable Matter Annihilation (PUMA) experiment at the European Organization for Nuclear Research (CERN) aims to achieve this goal [74].

Unstable isotopes are generated through nuclear reactions at radioactive ion beam facilities (RIBFs), such as the Isotope Separator On-Line DEvice (ISOLDE) facility at CERN. Given the short lifetimes of these isotopes, antiprotons must be provided at these facilities for the formation of antiprotonic atoms. As no facility exist that can provide antiprotons and radioactive ions to the same experiment for the foreseeable future, an alternative solution must be pursued. A possible solution to this conundrum is the accumulation of antiprotons produced at the Antimatter Factory at CERN and subsequent transport to the ISOLDE facility. Therefore, to investigate exotic nuclei with antiprotonic atoms, the PUMA experiment unfolds in three stages: Firstly, a sizable reservoir of antiprotons is gathered at the Antimatter Factory and stored in the PUMA setup. Subsequently, the reservoir, along with the experimental setup, is transported to ISOLDE (see Fig. 1.14). Finally, radioactive antiprotonic atoms are formed at ISOLDE, and their annihilation products are detected and identified.

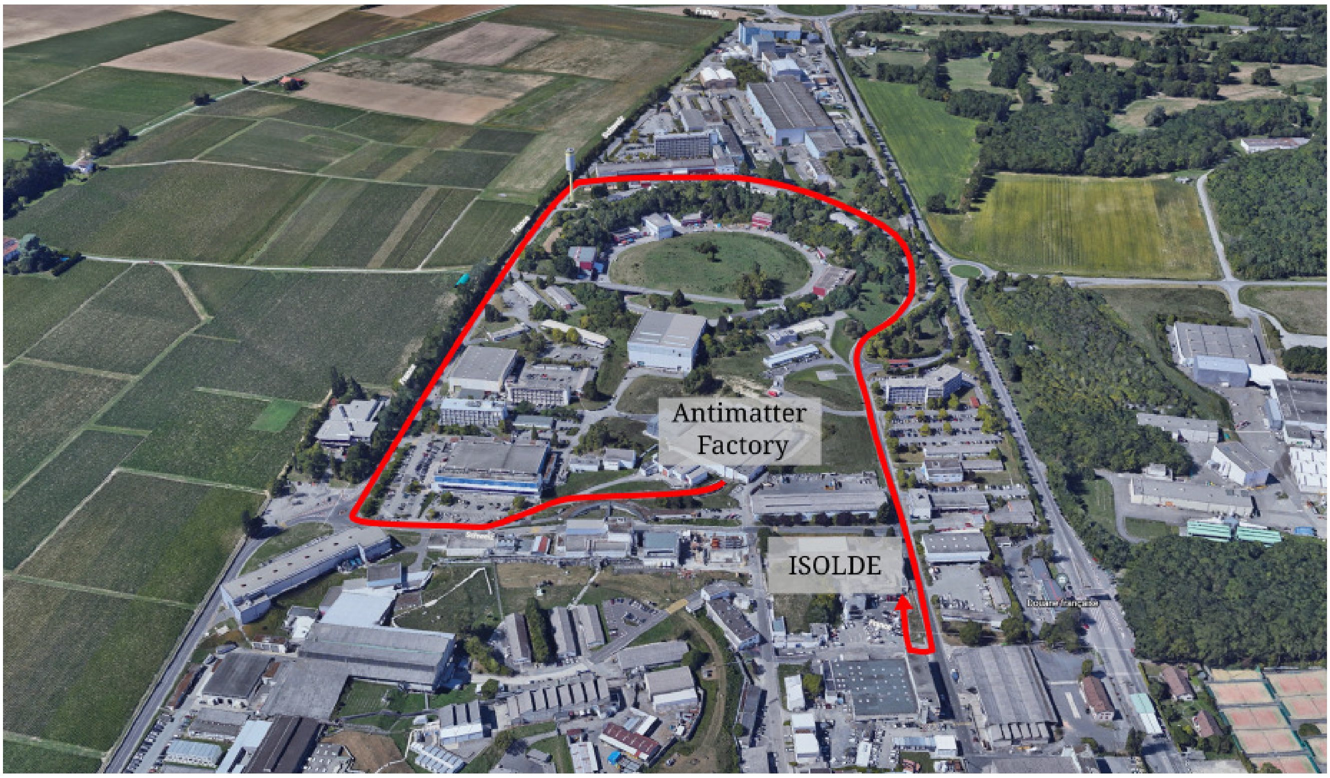

Figure 1.14.: Path from the Antimatter Factory to ISOLDE to transport antiprotons with PUMA. The path is chosen to avoid a bridge in the Route Rutherford. Figure adapted from [74] under CC BY 4.0.

At the heart of the PUMA setup is a double Penning trap, one for the storage of antiprotons (storage trap) and one for the production of antiprotonic atoms (collision trap). The collision trap is surrounded by a time projection chamber (TPC) for the detection of the pions produced in the annihilation. It in turn is itself surrounded by a plastic scintillator barrel that acts as a trigger for the TPC and also as an annihilation monitor around the storage trap. The system is housed in a 4 T warm bore solenoid, whose function is two-fold. It provides the necessary magnetic field for the Penning trap and forces the charged pions on curved trajectories, making it possible to differentiate positively and negatively charged particles from the direction of their curvature. It is depicted in Fig. 1.15.

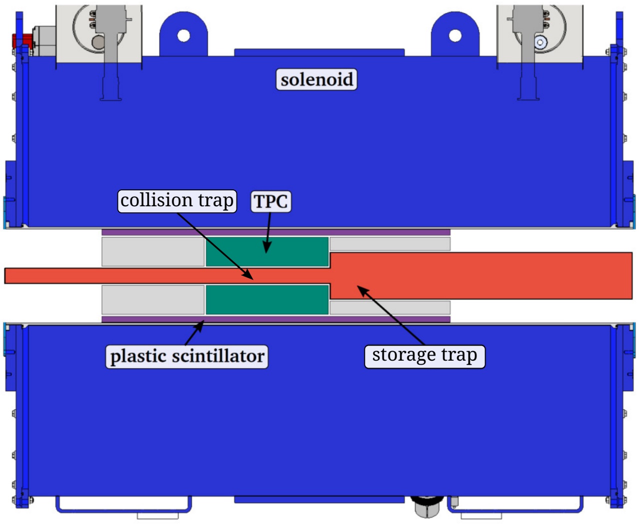

Figure 1.15.: Schematic view of the PUMA experimental setup, comprised of the double Penning trap, the TPC, plastic scintillator and solenoid. Figure adapted from [86] under CC BY 4.0.

To ensure that enough antiprotons are stored for the transport and ensuing experiments, annihilation of the antiprotons with residual gas molecules must be avoided. This makes excellent vacuum in the trap necessary, achieved by a cryogenic trap and the minimization of the pressure in the upstream beamline. Additionally, to avoid losses during storage due to expansion of the stored antiproton cloud, they must be sympathetically cooled with electrons provided by a field emission electron source located at the downstream end of the trap.

The solenoid, trap assembly and detector are transportable in operation in a stainless-steel frame measuring 3.5 by 1.9 by 2.8 meters, along with the necessary equipment to operate these components. In addition to this frame, a second smaller frame measuring 1.8 by 1.9 by 2.8 meters holds a cooling water chiller and a battery pack for powering the entire system during transportation. This secondary frame is connected to the main frame for transport and can be detached during operation at the Antimatter Factory and ISOLDE. A schematic overview of these two frames, forming the transportable experimental setup of PUMA, is illustrated in Fig. 1.16.

At the Antimatter Factory of CERN, the complete experimental setup is installed at the end of beamline LNE51 (see Fig. 1.17). LNE51 includes four ELENA-type electrostatic quadrupole doublets for beam steering. The beamline downstream of the handover point serves two important purposes. Firstly, to efficiently decelerate antiprotons from 100 keV to 4 keV and inject them into the PUMA trap setup, where they are further decelerated to a few 100 eV to be trapped. Secondly, to allow for the injection of ions from the offline ion source. These ions are used for first physics experiments with PUMA before moving to unstable nuclei at ISOLDE.

The offline ion source beamline incorporates a commercial SPECS IQE 12/38 electron impact gas ionization source, a multi-reflection time-of-flight (MR-ToF) spectrometer for isotopic purification, and a

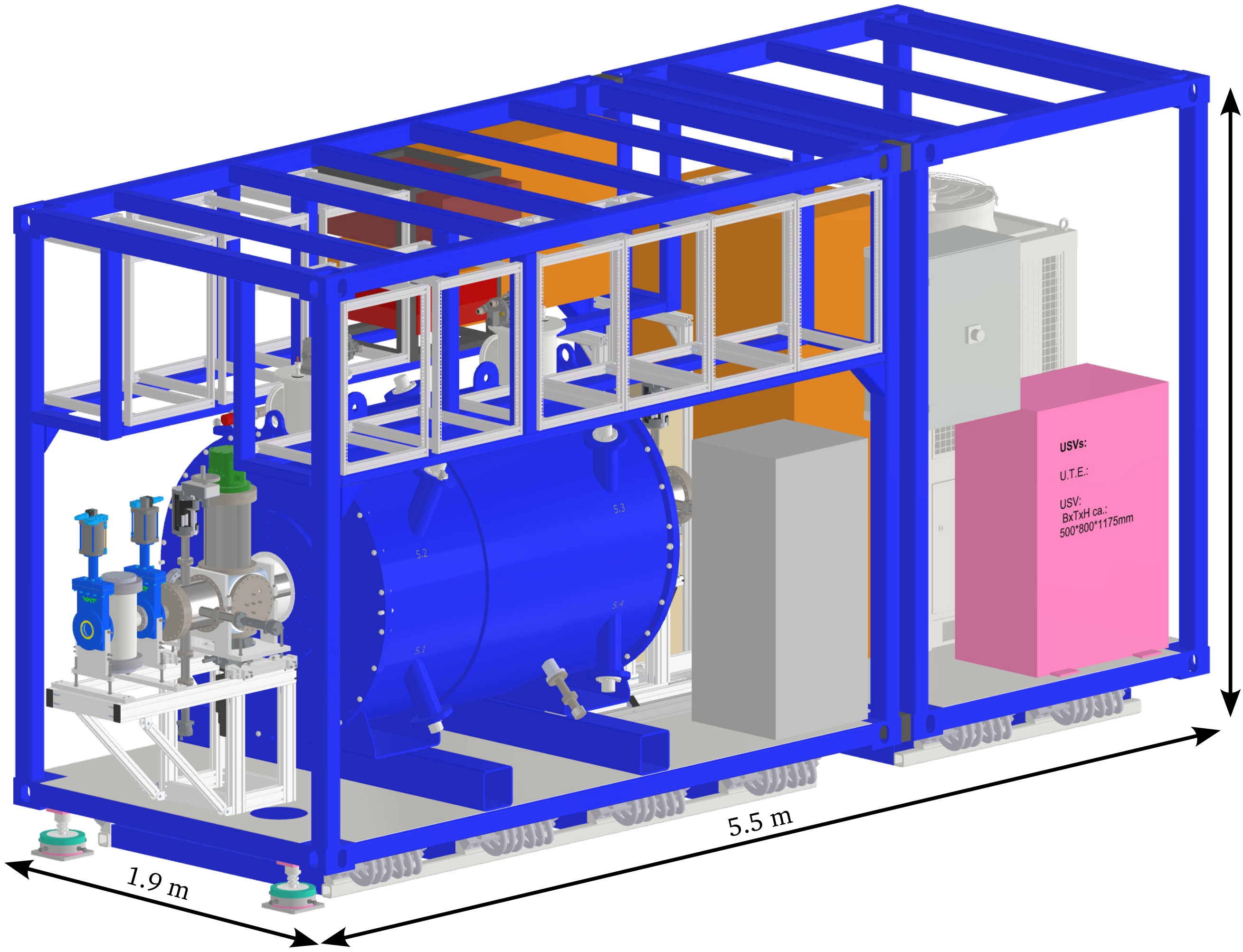

Figure 1.16.: The transportable part of the PUMA experiment. The bigger frame holds the experimental setup, the smaller one a water chiller and battery pack for transport.

radio-frequency quadrupole (RFQ) for accumulation and cooling.

The beamline must also maintain an excellent vacuum along the antiproton path to avoid annihilation with residual gas. Additionally, at the end of the beamline and the beginning of the PUMA trap setup a vacuum of better than 10^{-10} mbar must be reached to allow for long term storage in the storage trap.

The following work focuses on the design, construction and commissioning of two crucial components of the antiproton storage in PUMA: the deceleration from 100 keV to 4 keV, and the in-trap production of electrons for cooling from a few 100 eV to a few eV.

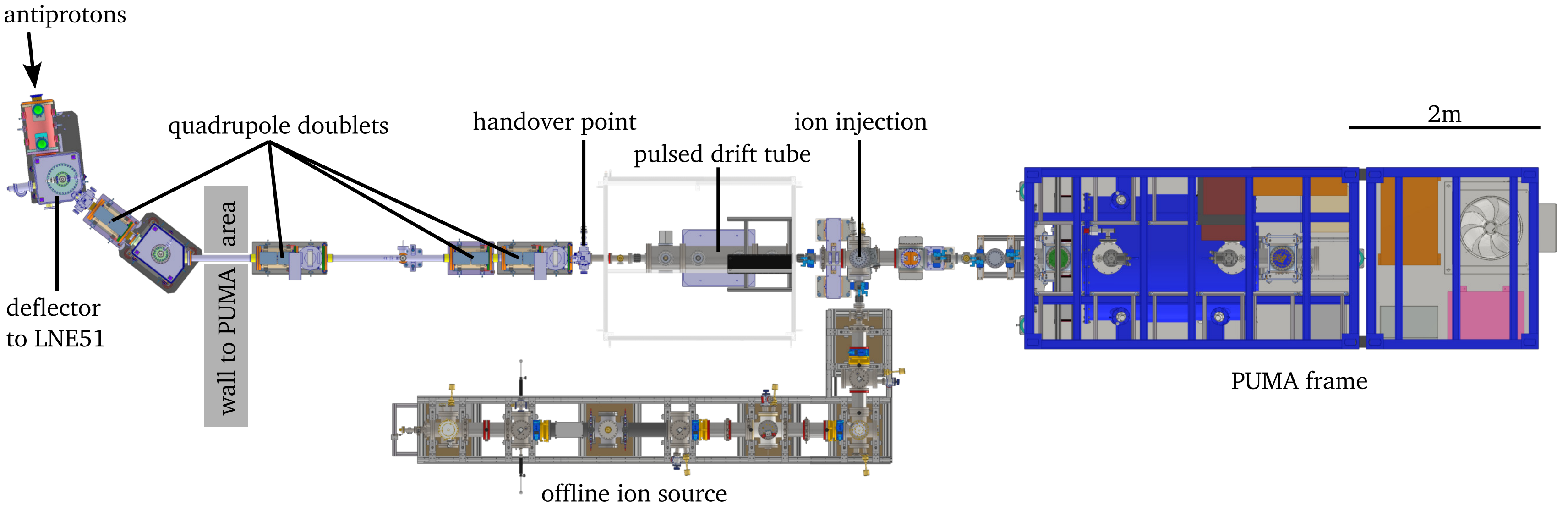

Figure 1.17.: Overview over the PUMA experimental area. Antiprotons are injected into the pulsed drift tube via LNE51 and slowed to 4 keV. The offline ion source beamline allows for the injection of stable beams into the trap.

2. The PUMA Low-Energy Antiproton Beam Line

The Extra Low ENergy Antiproton (ELENA) ring at the Antimatter Factory provides bunches of $1 \cdot 10^6$ to $1 \cdot 10^7$ antiprotons at 100 keV to up to four experiments every 110 seconds [108, 109]. To further decelerate the antiprotons energies of a few 100 eV so they can be trapped in a Penning trap, one can use a thin foil or pulsed drift tubes (PDT) [110–115]. Employing a foil for deceleration is space-efficient, but the yield is lower and the energy distribution broad [116], compared to a pulsed drift tube, which can have a transmission of 100% while conserving the width of the energy distribution. Trapping efficiencies for antiprotons with an initial energy around 100 keV range from a few percent [117] to 50% as a predicted upper limit given in [118]. However, for the PUMA experiment, which relies on the simultaneous trapping of antiprotons and stable and unstable ions, the use of a foil is unfeasible, since low-energy ions cannot penetrate the foil. Parts of this chapter are summarized and published in [119].

An established method to change the energy of a particle beam is to use a drift tube, where the potential can be changed rapidly. Here, the drift tube is set to a potential and is used to decelerate the particles to the desired energy when entering the drift tube. If the electrode is switched to a different potential, *e.g.*, ground, while the particles are still inside and in the field free region of the drift tube, they are not reaccelerated on exit. Because only the longitudinal and not the transversal kinetic energy is changed, the divergence angle α of the beam increases by a factor of

$$\frac{\alpha_{\text{out}}}{\alpha_{\text{in}}} \approx \sqrt{\frac{E_{\text{in}}}{E_{\text{out}}}}, \tag{2.1}$$

$$\text{with } E_{\text{out}} = E_{\text{in}} - E_{\text{PDT}} = E_{\text{in}} - q\,\Delta U_{\text{PDT}} \tag{2.2}$$

where E is the kinetic energy of the incoming and outgoing particles, E_{PDT} the energy due to the electric field of the pulsed drift tube, q is the charge of the particle and ΔU_{PDT} the potential difference on the pulsed drift tube. This divergence has to be compensated by additional ion optical elements or beam cooling.

Pulsed drift tubes are widely used in ion trap experiments for energies as high as 60 keV [120–123], often in combination with buffer-gas cooling to counteract the increase in transversal emittance. The GBAR experiment at CERN is confronted with similar challenges as the PUMA experiment, as they need to decelerate antiprotons from 100 keV down to 1 keV [124]. Their pulsed drift tube design [113] serves as a basis for the PUMA pulsed drift tube.

At the PUMA experiment, the antiprotons are decelerated from 100 keV to 4 keV and in a second step down to 100 eV right in front of the trap. The beam energy of 4 keV is chosen as a compromise between better capture for lower energies and better beam transport for higher energies. An energy of 4 keV also allows the use of standard SHV (safe high voltage) components for the ion optical elements, such as einzel lenses. Higher energies also allow for beam transport in pipes with smaller diameters (see Eq. 2.1), reducing the outgassing area and thereby contributing to a lower pressure.

Simulations show, that at the downstream end of the beamline a vacuum of 10^{-10} to 10^{-11} mbar is required to reach sufficient storage times of the antiprotons of more than 30 days [86], limited by the annihilation with residual gas molecules. Similarly, on the upstream end, the pressure must not exceed $5 \cdot 10^{-7}$ mbar during operation, as not to trigger the interlock protecting the ELENA vacuum. Also, the vacuum should be better than 10^{-9} mbar on the upstream end to not contaminate the vacuum of ELENA.

2.1. Overview

The transport of 100 keV particles, H^- ions or antiprotons, from the ELENA ring to the PUMA experiment is performed by the LNE51 transfer line. LNE51 branches off from the LNE50 transfer line from ELENA to the adjacent GBAR experiment. Four electrostatic quadrupole/H-V corrector units (denoted as ZQNA in Fig. 2.1) are installed in the line, to match the beam to the PUMA experiment. At the focal point, the beam spot size (rms) is approximately 2 mm and the horizontal and vertical geometric emittance ($95\% = 6\epsilon_{\mathrm{rms}}$) is 6 mm mrad and 4 mm mrad, respectively [125]. The layout of LNE51 is shown schematically in Figure 2.1. Two SEM (Secondary Emission Monitors) grids [126] are installed in LNE51 (see Fig. 2.1). They are standard equipment in the ELENA transfer lines that allow to extract the profile of the impinging beam, either H^- ions or antiprotons with a transmission of 90% [127].

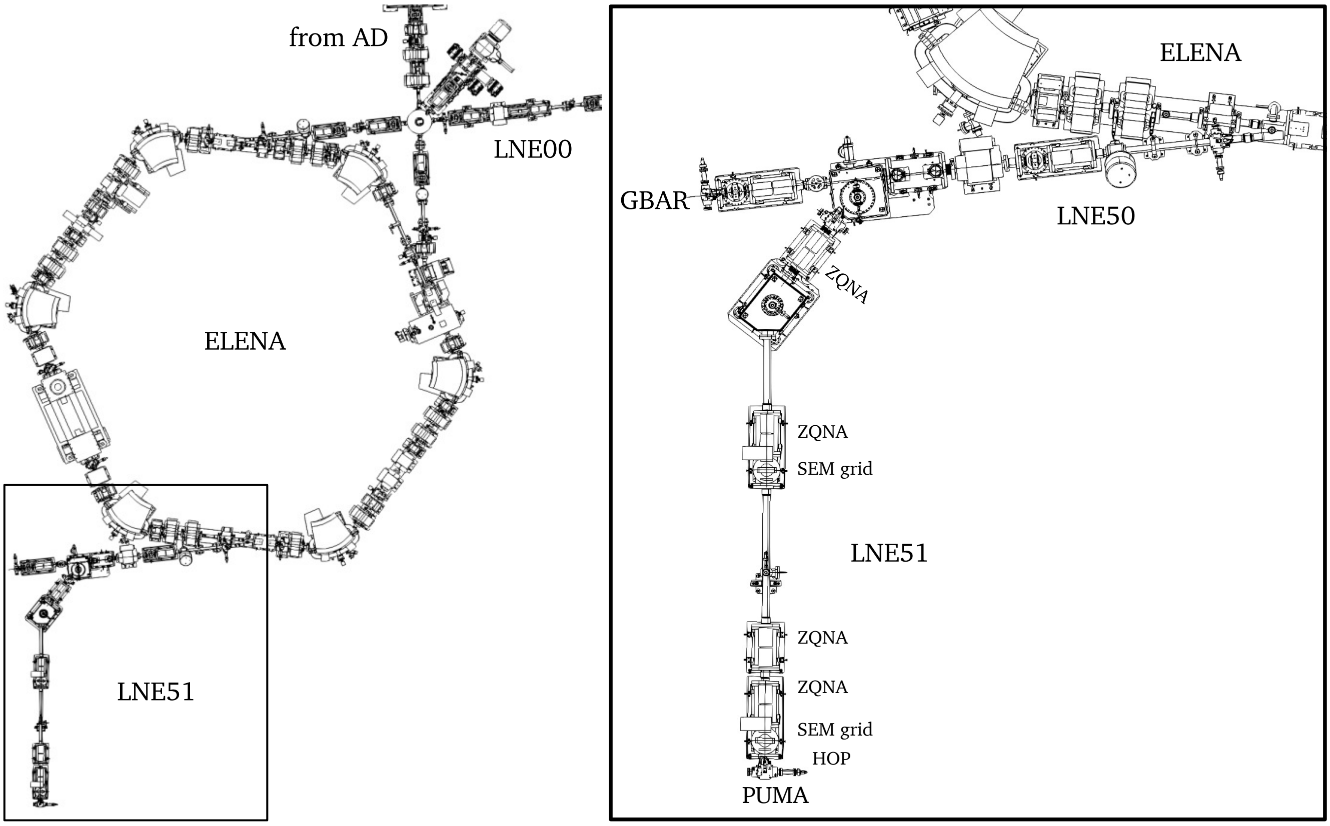

Figure 2.1.: Schematic top view of the ELENA ring with the transfer lines LNE00 (to ASACUSA, ALPHA, AEGIS, GBAR, BASE and BASE-STEP) and LNE51 to PUMA. The right panel shows the LNE51 line in more detail. Antiprotons are ejected from the ELENA ring into LNE50, from which LNE51 branches off. The handover point (HOP) is where the beamline changes responsibility from CERN to PUMA. Figure adapted from [119] under CC BY 4.0.

The space available in the PUMA experimental area is roughly 15 m by 5 m. The physical handover point is 3.5 m from the wall in beam direction. The PUMA frame is 5.5 m long and the space between the frame and the back wall should be at least 1.2 m as a walkway (see Fig. 2.2).

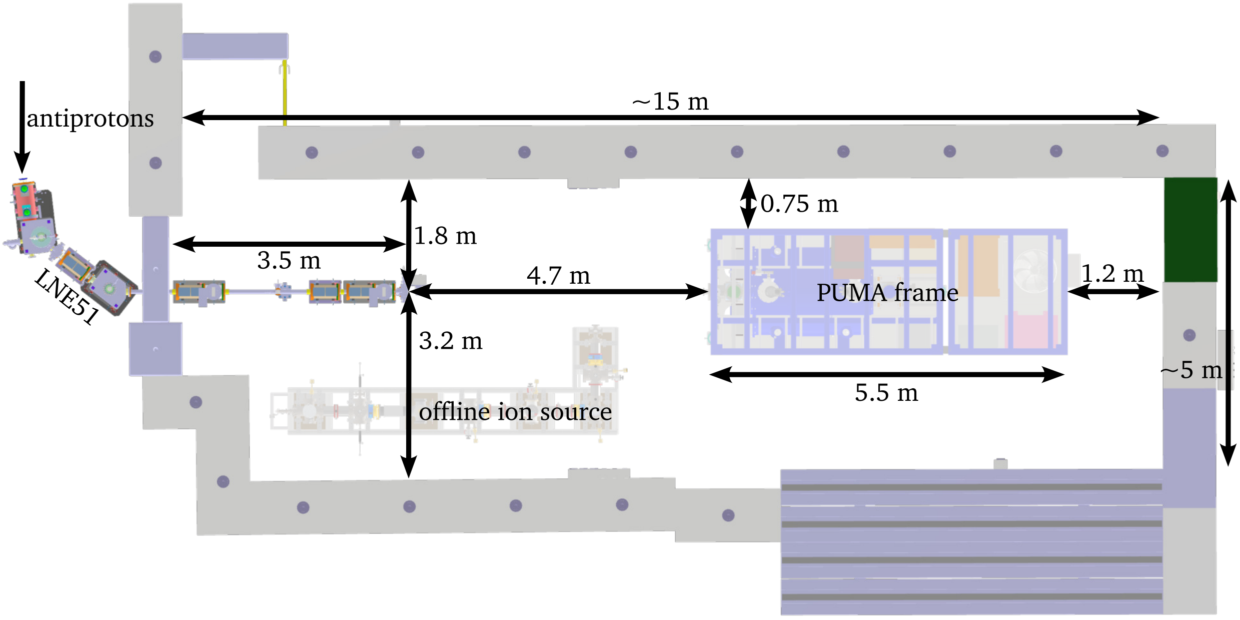

Figure 2.2.: Footprint of the PUMA experimental area. The space available for the antiproton beamline is limited by the offline ion source and the PUMA frame.

This leaves 4.7 m for the antiproton beam line, that must include the following parts

- the pulsed drift tube for deceleration, including a safety cage for high-voltage parts,
- a quadrupole bender for injections of ions from the offline ion source,
- a secondary emission monitor (SEM grid) for position sensitive particle detection in front of the trap,
- einzel lenses to steer and focus the beam,
- a connector to remove and attach the PUMA frame to the beamline,
- a differential pumping section to reduce the pressure to 10^{-11} mbar in front of the PUMA frame,
- gate valves to isolate different sections,
- bellows to allow for alignment of the ion optical elements,

and in addition, not taking up space in the direction of the beam,

- vacuum gauges,
- valves for the initial pump down and venting, and
- vacuum pumps

When choosing the size of the beam pipe, several factors have to be considered. The inner diameter should be as small as possible, as this reduces the area that outgasses as well as the conductance of the pipe, contributing to a lower pressure. Furthermore, it determines the cost, especially of the gate vales used to separate the sections. On the other hand, the beam pipe must be wide enough to be able to accommodate the slowed-down beam. Decelerating the beam from 100 keV to 4 keV leads to an increase of the divergence angle by a factor of 5 (see Eq. 2.1), which roughly translates to an increase in beam diameter from 4 mm to 20 mm. To have a sufficient safety margin, a pipe of at least CF DN63 with an inner tube diameter of roughly 63 mm has to be used.

The PUMA antiproton beam line consist of 4 sections (see Fig. 2.3): section 1 with the pulsed drift tube for the deceleration of the antiprotons, section 2 with the quadrupole bender for the injection of ions from the offline ion source, the connector section to couple the PUMA frame to the beam line and a pumping section to reach the necessary pressure in front of the PUMA trap assembly.

A detailed description of all parts can be found in Appendix A.

Section 1 contains the pulsed drift tube assembly, which consists of a high-voltage einzel lens (HV EL), the pulsed drift tube (PDT), and a low voltage (5 kV) einzel lens (LV EL). Its design is detailed in Section 2.5.

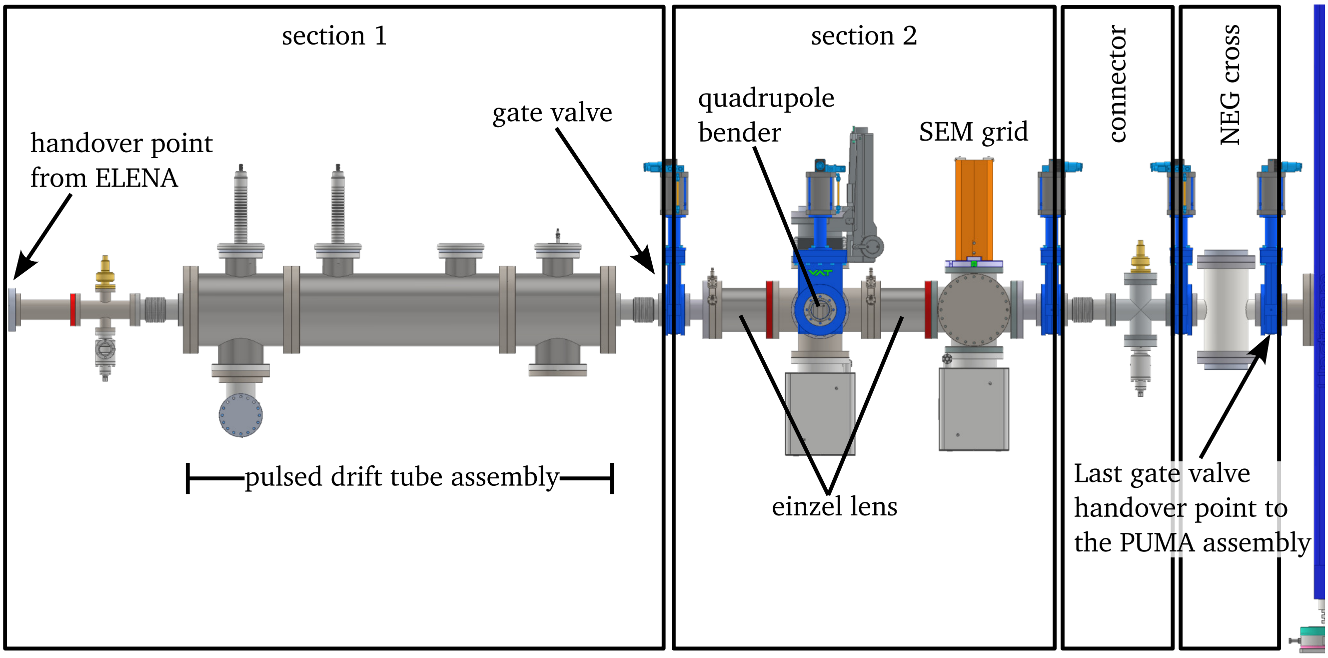

Figure 2.3.: The four sections of the PUMA antiproton beamline, separated by gate valves. The antiprotons enter on the left from LNE51. The last gate valve defines the handover point to the PUMA trap assembly. The parts a detailed in Appendix A.

2.2. Junction for Injecting Ions from the Offline Ion Source

Section 2 centers around the junction for injecting ions from the offline ion source. For this, a quadrupole bender adapted from a design from the university of Greifswald is used. It is mounted on a linear feedthrough, so it can be moved out of the beamline when no ions are injected. It is also possible to shoot antiprotons through the quadrupole bender. The bender consists of four electrodes, each a quarter segment of a cylinder oriented with the curvature towards the middle (see Fig 2.4). When applying opposite voltages to neighboring electrodes, the path of ions can be bent by 90°. The voltage needed for this is in the order of 10% of the ions' energy, *i.e.*, a few 100 volts for 4 keV ions. In front of the quadrupole electrodes are einzel lenses to focus the beam in and out of the bender. The aperture of the einzel lens is 18 mm wide which, according to simulations [86] allow for 100% transmission of antiprotons even when the bender is in the beamline. For the choice of materials, see Section 2.4 Vacuum Considerations.

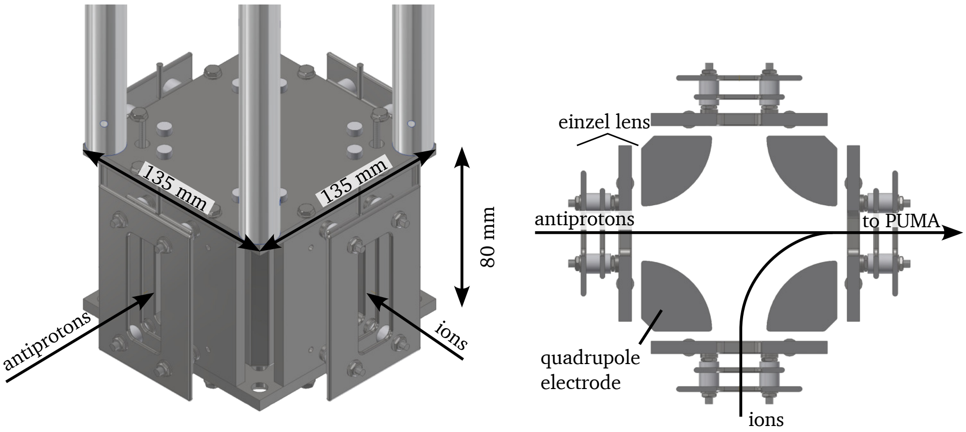

Figure 2.4.: The quadrupole bender for the injection of ions into the beamline. Left: a 3D view with the bars attaching the bender to the flange at the top. Right: a top-down cut view of the bender, the antiprotons traverse it straight and the ions can be directed into the beamline.

Up- and downstream of the quadrupole bender is one einzel lens, respectively. The einzel lenses have one four-fold segmented electrode, that would normally be grounded (see Fig. 2.4). By applying a voltage of a few 10 volts, the beam can be steered in the x-y-direction. For the choice of materials, see Section 2.4.

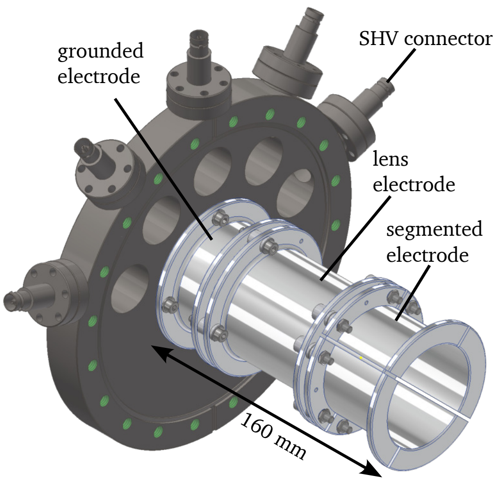

Figure 2.5.: The einzel lens assembly with one segmented electrode for beam steering in the x-y-direction.

Further downstream, a position sensitive detector is located. Originally, a SEM grid was foreseen, but because of delays in the delivery, a beam TV (BTV) was used instead. This has several drawbacks. A BTV uses a scintillating screen and a camera to determine the beam profile and position. The particles need sufficient energy to excite the scintillator, in our case phosphor. Because of the energy released in the annihilation, antiprotons are visible even at low energies, but H^- ions, used at ELENA as a proxy, are not. Also, the screen is not transparent for the beam and therefore has to be moved out of the beamline during operation of downstream elements.

2.3. Connector and NEG Cross

To move the PUMA transportable frame to ISOLDE for measurements of radioactive nuclei, it must be disconnected from the beamline at ELENA. To make this possible, a part of the beamline can be removed to make room for the maneuvering of the PUMA assembly (see Fig 2.6). The connector section consists of a bellow that is compressed to remove it and a valve for venting and pumping, as well as a pressure gauge.

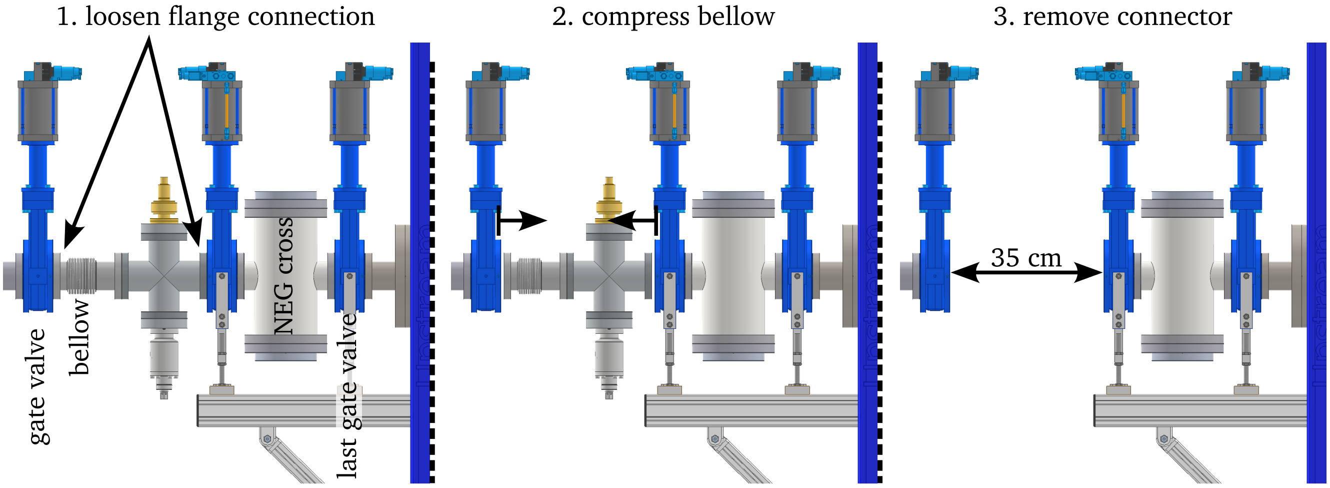

Figure 2.6.: The steps to disconnect the PUMA assembly from the beamline. First, the flange connections on the gate valves are undone (left panel). Then, the bellow is compressed to remove the connector (middle panel). Finally, with the connector removed, there is a space of 35 cm for craning operations (right panel). To connect to the beamline the steps are followed in reverse.

In front of the last gate valve, a pressure of 10^{-11} mbar is necessary. To achieve this, a cross purely for pumping is installed. Since the main component of residual gas in the trap is hydrogen, NEG cartridges (2 with $\sim$1000 l/s each) are used (see Sec. 2.4). The gate valve downstream of the pumping cross, referred to as the last gate valve, defines the end of the beamline and is the handover point to the PUMA trap assembly. To avoid exposing the NEG cartridges to air during moving, the NEG cross is part of the PUMA transportable frame.

2.4. Vacuum Considerations

The pressure p of a system is governed by the total outgassing and leak rate $\dot{Q}$ in mbar l/s and the pumping speed S in l/s

$$p = \frac{\dot{Q}}{S}. \tag{2.3}$$

To reach the required pressure of 10^{-11} mbar at the end of the beamline, the outgassing of all components must be minimized, and the pumping speed maximized. There are two main components contributing to the outgassing, atmospheric water vapor stuck to the surface of all components and hydrogen trapped in the bulk material. To accelerate the process of water molecules evaporating from the surface, the whole system is heated in a process called ‘baking’. The temperature and duration depend on the heat tolerance of the materials used, and can reach from 60°C for sensitive detectors to 450°C for stainless steel components. After a few days to a week, the outgassing of hydrogen from the bulk material becomes the dominant factor and the baking can be stopped. When the system is opened, water vapor from the atmosphere will stick to the surface again, and the baking procedure has to be repeated.

The removal of hydrogen from the bulk of the material scales with the temperature. Vacuum components are heated to temperatures of 1000°C under vacuum, this process is called 'vacuum firing' [128]. Other than with water vapor, this leads to a permanent reduction in the outgassing rate. Hydrogen outgassing is a problem in stainless steel especially, because the manufacturing process leads to hydrogen dissolving in the steel, that then later diffuses out and into the vacuum chamber.

The beamline is built from CF flange components made from stainless steel with copper gaskets. The low leak rates of less than $1 \cdot 10^{-11}$ mbar l/s, and ability to bake up to[*] 450°C allows operating at pressures below 10^{-11} mbar. To reduce the outgassing of hydrogen, all our CF flange components were vacuum fired by the manufacturer or at CERN before the assembly of the beamline.

The outgassing rate is also influenced by the choice of material. After baking, hydrogen is the dominant source of outgassing, and the only relevant gas in the cryogenic trap system of PUMA [86]. Therefore, we only focus on hydrogen outgassing rates. To reach ultra-high vacuum (UHV) no hydro-carbons must be used. For the insulation of in-vacuum cables, Kapton is used, and MACOR® ($1.1 \cdot 10^{-11}$ mbar l/s/cm^2 [129]) as an insulator for electrodes. Due to the low number of Kapton insulated cables (<20 m), their outgassing does not have an effect. Non-insulating parts are preferably made from aluminum ($\sim 1 \cdot 10^{-13}$ mbar l/s/cm^2) as opposed to stainless steel ($\sim 3 \cdot 10^{-12}$ mbar l/s/cm^2) [130], as the outgassing rates are lower. We use aluminum from the 6000 series (International Alloy Designation System) and steel WNr. 1.4429 (AISI 316LN).

For pumping, sputter ion pumps and non-evaporable getters are used. A requirement from the ELENA side is not to use a turbomolecular pump, as during a power cut, they would allow for the flow of molecules back through the pump, destroying the vacuum. Sputter ion pumps as well as non-evaporable getters are not connected to the atmosphere, but instead adsorb or absorb the gas molecules. Non-evaporable getters (NEG) are made from an alloy of Zr, V, Ti, Al and Fe, that can be used in a dedicated NEG cartridge or sputtered directly onto a surface like the wall of a vacuum chamber. Reactive[†] molecules like H_2O and N_2 are removed from the volume by chemical reaction with the getter material. Hydrogen is removed by a different mechanism. The molecule dissociates at the surface and the atoms quickly diffuse into the material. NEG is mostly used to pump hydrogen due to its high pumping speed and capacity. The capacity to pump reactive gases is much lower and hydrocarbons, mainly methane (CH_4), and noble gases cannot be pumped at all, due to their inertness. To complement the NEG, sputter ion pumps are used (see Tab. 2.1). A comparison between the Saes CapaciTorr Z1000 and the Agilent VacIon Plus 300 StarCell, both used in the antiproton beamline, can be found in Table 2.1. As an orientation, a turbo pump (Edwards nEXT730H) is also listed.

The inside walls of many vacuum chambers are also NEG coated at CERN, to turn them from a source of hydrogen into a sink. Some parts are not coated, those close to the SEM grid, because the outgassing of those would quickly saturate the NEG, leaving it useless. Using the aforementioned outgassing rates and pumping speeds as an input, a first estimate of the vacuum was done using two methods. First with an equivalent electrical network analysis (see Sec. 2.4.1), and subsequently with MOLFLOW+ (see Sec. 2.4.2).

---

[*] It is recommended to use silver plated copper gaskets when baking at high temperatures to reduce the risk of strong adhesion between the flange and gasket.

[†] meaning they chemically react with the getter material

Table 2.1.: A comparison between a NEG cartridge (Saes CapaciTorr Z1000), a sputter ion pump (Agilent VacIon Plus 300 StarCell) and a turbo pump (Edwards nEXT730H).

	Saes	Agilent	Edwards
	CapaciTorr Z1000	VacIon Plus 300 StarCell	nEXT730H
Type	NEG cartridge	ion pump	turbo pump
pumping speed nitrogen	360 l/s	240 l/s	730 l/s
pumping speed hydrogen	1250 l/s	360 l/s	750 l/s
pumping speed noble gases	0 l/s	48 l/s	750 l/s
pumping speed methane	0 l/s	215 l/s	-

2.4.1. Electrical Network Analysis (ENA)

To get an estimate of the achievable vacuum in the beamline and the corresponding outgassing rates and pumping speeds, the beamline was simulated in the Electrical Network Analysis (ENA) framework. Because the equations describing pressure in a vacuum system are analogous to those describing an electrical network (see Table 2.2) [131–133], one can use off-the-shelf analog electronic circuit simulators to calculate the equilibrium pressure in the system.

Table 2.2.: Quantities and equations describing a vacuum system and their electrical network counterpart.

Vacuum			Electrical Network	
gas flow	$\dot{Q} = C \cdot p$		Ohm's law	$I = G \cdot U$
pressure change	$\dot{Q} = V \cdot \frac{\mathrm{d}p}{\mathrm{d}t}$		voltage change	$I = C \cdot \frac{\mathrm{d}U}{\mathrm{d}t}$
$\dot{Q}$	gas flow	mbar l/s	I	current
C	conductance	l/s	$G = \frac{1}{R}$	conductance
p	pressure	mbar	U	voltage
V	volume	l	C	capacitance

With that, one can build an equivalent electrical network for a simplified vacuum system and calculate the pressure. The information needed are the total incoming gas flow $\dot{Q}_{\mathrm{in}}$, *i.e.*, outgassing and leaks, the pumping speed S_0 and the conductance C of all parts. The conductance C of a long round pipe with diameter d and length l can be analytically calculated

$$C = \sqrt{\frac{k_{\mathrm{B}}T}{2\pi m_0}} \cdot \frac{\pi d^3}{3l}. \tag{2.4}$$

Here, T is the temperature of the gas, m_0 the mass of the gas molecule and k_{B} is the Boltzmann constant. Figure 2.7 shows a simple vacuum system and its equivalent electrical network.

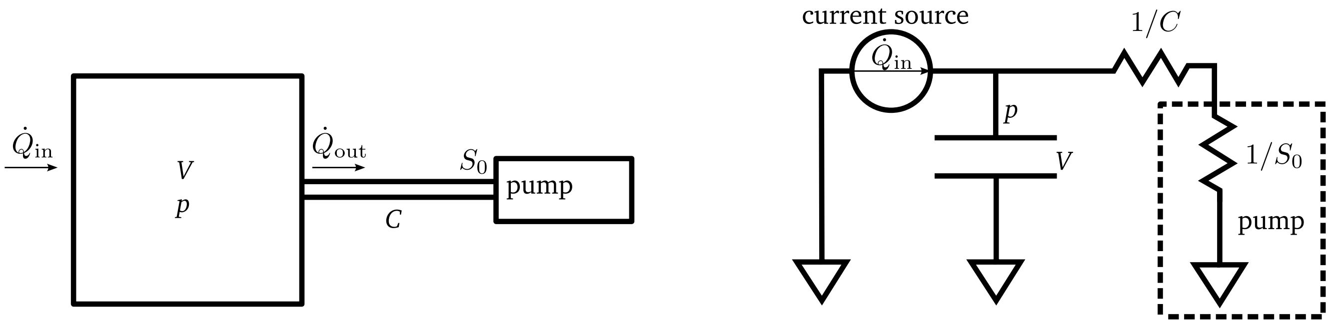

Figure 2.7.: A simple vacuum system and its equivalent electrical network. Vacuum pumps are modeled as resistance $R = 1/S_0$, where S_0 is the pumping speed.

This ansatz was used to model the entire PUMA antiproton beamline in *LTSpice*, an electronic circuit simulator [134], to determine the necessary pumping speed and maximum acceptable outgassing rate. For all parts, the conductance, volume, outgassing rate and pumping speed were determined. The outgassing rate was calculated with the surface area and the assumption of baked stainless steel with an outgassing rate of $5 \cdot 10^{-12}\,\mathrm{mbar\,l/s/cm^2}$, and for surfaces coated in NEG, a pumping speed of $0.044\,\mathrm{l/s/cm^2}$ was used. Vacuum gauges were implemented with an outgassing rate of $1 \cdot 10^{-9}\,\mathrm{mbar\,l/s}$ [135], gate valves and beam instrumentation with $1 \cdot 10^{-8}\,\mathrm{mbar\,l/s}$, and the pulsed drift tube with $1 \cdot 10^{-7}\,\mathrm{mbar\,l/s}$. Only hydrogen was considered. A part of the beamline as modeled in LTSpice XVII can be seen in Fig. 2.8. Pipes are modeled as a capacitance (volume) with resistances corresponding to the conductance of a pipe with half the original length on either side.

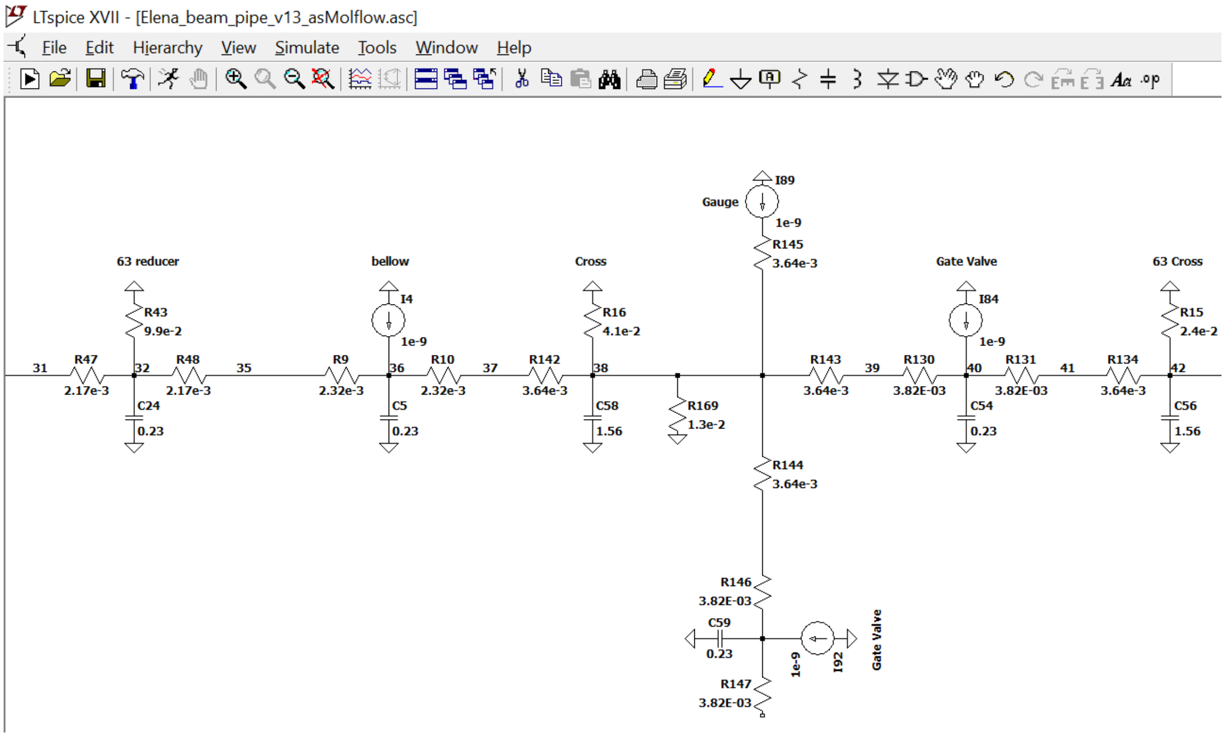

Figure 2.8.: Screenshot of LTSpice XVII, the analog electronic circuit simulator used to calculate the pressure with a part of the beamline implemented.

The electrical network analysis indicates that to reach a vacuum better than 10^{-10} mbar at the end of the beamline, most attention must be paid to the outgassing of the gate valve closest to the PUMA Penning trap. The effect of reducing the outgassing of the gate valves from 10^{-8} mbar to 10^{-9} mbar can be seen in Fig. 2.9. Also, two different input pressures at the handover point from LNE51 were considered. A change in pressure at the HOP has a negligible effect on the pressure at the end of the beamline, whereas, the closer to the last gate valve, the higher the effect of outgassing. Reducing the outgassing rate of the gate valves reduced the pressure from $6 \cdot 10^{-11}$ mbar to below $1 \cdot 10^{-11}$ mbar. The absolute values of this calculation are only indicative of the order of magnitude that can be reached, and demonstrate the effect of the outgassing. It shows, that effort should be put into the end of the beamline and in reducing the outgassing of the gate valves. Therefore, no beam instrumentation should be put into the last sections and it must be baked, to reach an outgassing rate of better than $1 \cdot 10^{-9}$ mbar l/s.

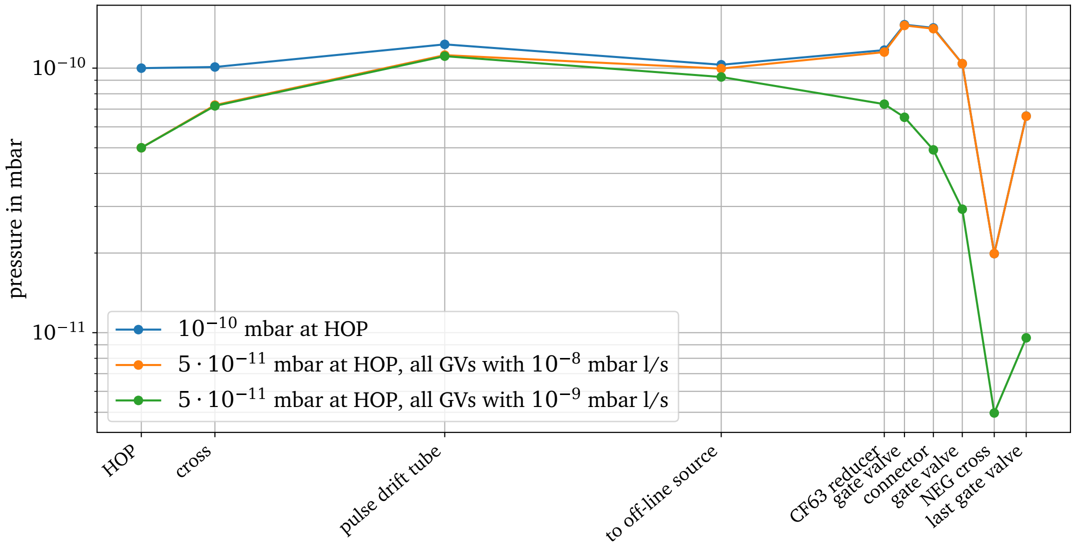

Figure 2.9.: Effect of outgassing reduction of the gate valves and pressure at the handover point (HOP). The pressure at the HOP has almost no effect on the pressure at the end of the beamline, as opposed to the outgassing of the gate valves at the end of the beamline.

2.4.2. MOLFLOW+ Simulations

MOLFLOW+ and ENA Comparison

To get a more detailed picture of the pressure along the beamline, it was simulated with a Monte-Carlo Simulator package developed at CERN, called MOLFLOW+ [136]. In the molecular flow regime, collisions between particles can be neglected, which allows simulating the trajectory of particles independently. The advantage over the electrical network analysis is, that the geometry can be modeled in more detail, since the conductance is not approximated by that of a tube. Also, distributed pumping and outgassing can be modeled more easily. A downside is that it can take several hours to reach sufficient statistics to calculate a pressure. The software works in the following way. The surfaces enclosing the volume are placed in one of three categories: absorbing, desorbing, or deflecting particles. Pumps and NEG coatings are modeled as absorbing surfaces, outgassing as desorbing surfaces and the rest reflect particles according to Knudsen's cosine law [137]. An example of how the beamline is modeled in MOLFLOW+ is shown in Fig. 2.10 with the corresponding CAD model.

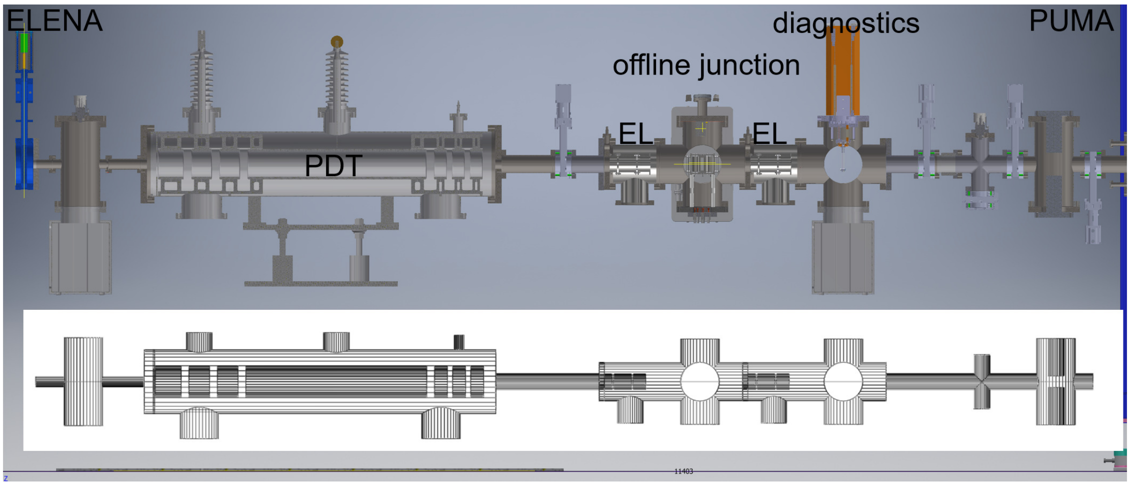

Figure 2.10.: The antiproton beamline with the corresponding MOLFLOW+ representation below.

A comparison between the ENA and the MOLFLOW+ simulation can be seen in Fig. 2.11. The input pressure for both simulations is the same at $2.1 \cdot 10^{-10}$ mbar. The ENA overestimates the local effect of the pumping, because it is not distributed over a surface, but instead concentrated in one point.

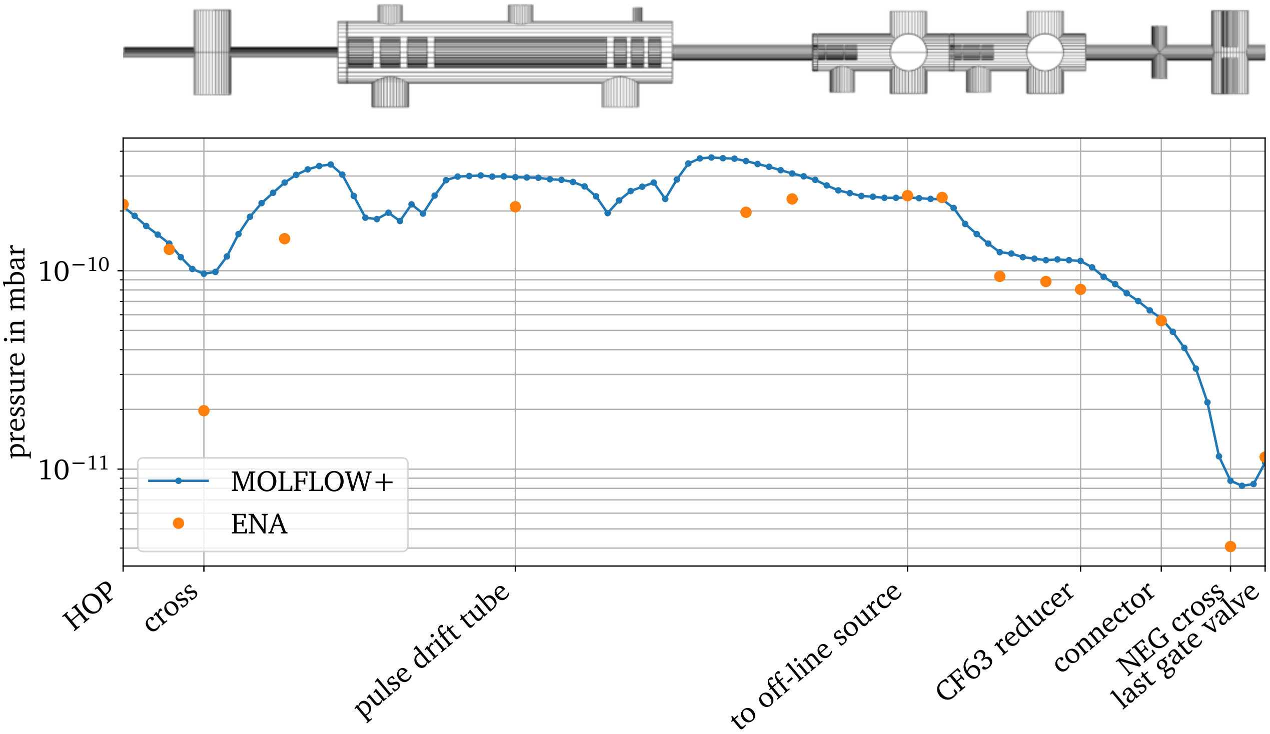

Figure 2.11.: A comparison between the MOLFLOW+ simulation and the ENA. The pressures at the last gate valve are $1.08 \cdot 10^{-11}$ mbar from MOLFLOW+ and $1.15 \cdot 10^{-11}$ mbar from the ENA. The ENA appears to overestimate the effect of the pumping, as it is not a realistically distributed on the surface.

Also, the MOLFLOW+ simulation more realistically predicts a rise in pressure inside the drift tube and electrodes, as they obstruct the pumping in the middle of the beamline, but contribute to the outgassing. Overall, in both simulations, the same trend can be observed, especially the steep drop in pressure at the end of the beamline, and the increase at the last gate valve. Both methods predict a pressure of around 10^{-11} mbar at the last gate valve, confirming the ENA estimate.

Beaming

An effect, that cannot be investigated with ENA, but with MOLFLOW+ is the so-called 'beaming'. Particles traversing an aperture from one large (compared to the aperture) volume to another have an angular distribution that follows a Lambertian radiator. Here, the probability for any angle is proportional to the cosine of that angle. In the case of tubes with non-zero length, the probability gets skewed towards more forward angles, similar to the effect of a collimator. At the end of the beamline, the angular distribution is therefore not a cosine, but more forward focused (see Fig. 2.12).

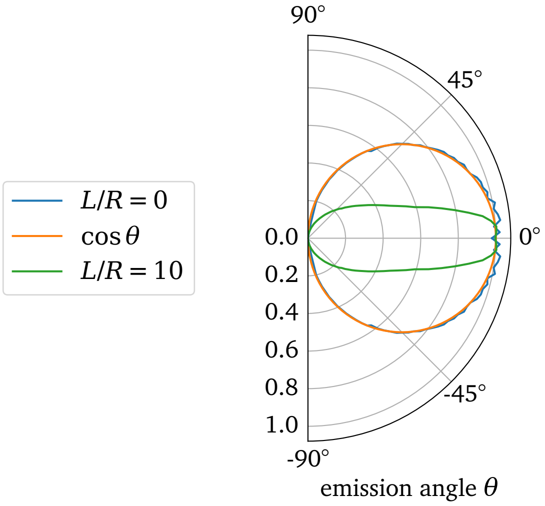

Figure 2.12.: The effect of beaming. In blue, the distribution of emission angles behind an aperture simulated with MOLFLOW+ is shown. It follows a cosine distribution (Lambertian radiator), shown in orange. Behind a pipe with length-to-radius ratio of $L/R = 10$, the distribution is more forward directed (green).

The pressure inside the PUMA cryostat was simulated with COMSOL by A. Schmidt [86], as it allows for a surface-coverage dependent pressure calculation and a time-dependent surface coverage, crucial for the long term behavior of the pressure. A drawback of the COMSOL software is, that it assumes a reservoir with a given pressure at the input, leading to a cosine distribution for the particle direction at the entrance. This leads to an underestimation of the particle density inside the trap, compared to a simulation of the complete beamline, see Fig. 2.13. Setting the input at the cryostat entrance to a cosine distribution resembles the COMSOL results more closely. Both simulations were done assuming 10^{-11} mbar at the last gate valve. The simulation underlines the effect of beaming and the necessity for an aperture blocking device in front of the trap, implemented as a rotating cylinder shutter in the PUMA setup [86]. The angular distribution at the entrance of the cyostat is shown in Fig. 2.14 in blue, as well as a cosine distribution in orange.

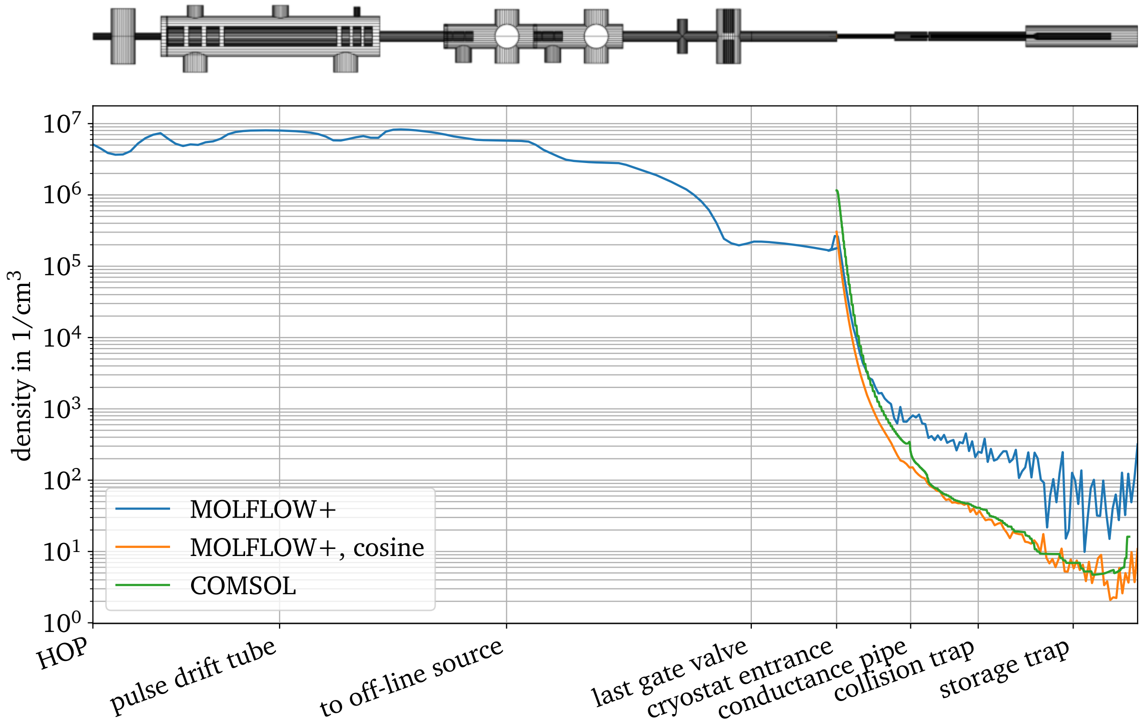

Figure 2.13.: A MOLFLOW+ simulation of the whole beamline with the PUMA Penning trap attached. As a comparison, a COMSOL simulation of the density in the trap is shown in green [86]. The COMSOL simulation underestimates the density inside the trap, because it does not take into account the beaming caused by the beamline upstream. In orange, the density inside the trap calculated with MOLFLOW+ under the assumption of a cosine distribution at the cryostat entrance reproduces the densities found in COMSOL.

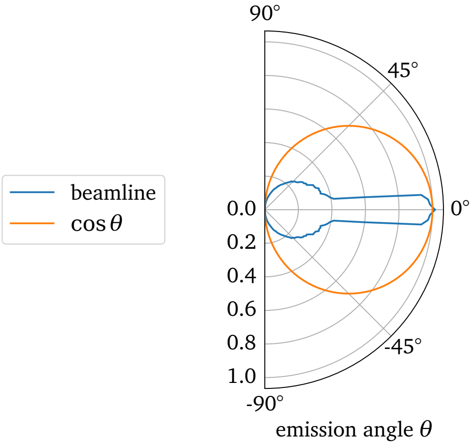

Figure 2.14.: The effect of beaming at the cryostat entrance. The angular distribution simulated in MOLFLOW+ in blue and a cosine distribution in orange as a comparison. The simulated distribution has a much larger forward component compared to the cosine.

If the results of these simulations are to be trusted, the hydrogen density in the collision trap is ~ 10 times higher than previously estimated. This leads to a 10-fold increase in background signal due to the increased annihilation rate of antiprotons with hydrogen. To reduce the background, one can think of a scenario where stable or long-lived ions are loaded into the trap and before mixing with antiprotons the shutter is used to close the trap. For the investigation of short-lived isotopes at ISOLDE, a careful study of the PUMA beamline at ISOLDE is necessary to determine the beaming effect. A possibility to counter it is the introduction of an angle of a few degrees in the beamline in combination with an electrostatic kicker to deflect the ions into the trap but suppress the beaming.

Parameter Study

To figure out which change on the beamline has the greatest effect on the vacuum at the last gate valve, the pressure was simulated with MOLFLOW+ for different parameter sets. The parameters varied were the number of ion pumps N_{pumps}, and the outgassing of the offline ion source beamline ($\dot{Q}_{\text{IB}}$), gate valves ($\dot{Q}_{\text{GV}}$), and pulsed drift tube ($\dot{Q}_{\text{PDT}}$). The considered parameters are listed in Tab. 2.3, and the pressure is also shown in Fig. 2.15. Globally, the parameter sets with $\dot{Q}_{\text{IB}} < 10^{-6}$ mbar l/s give a lower pressure. Within the two categories of $\dot{Q}_{\text{IB}}$, $\dot{Q}_{\text{GV}}$ separates the sub-regimes. Therefore, $\dot{Q}_{\text{IB}} < 10^{-7}$ mbar l/s, and $\dot{Q}_{\text{GV}} < 10^{-9}$ mbar l/s are targeted to achieve a vacuum of a few 10^{-11} mbar. With a 20 cm long CF63 pipe connecting the ion beamline and the antiproton beamline, a flow of 10^{-7} mbar l/s corresponds to a pressure of $7 \cdot 10^{-10}$ mbar at the end of the ion beamline.

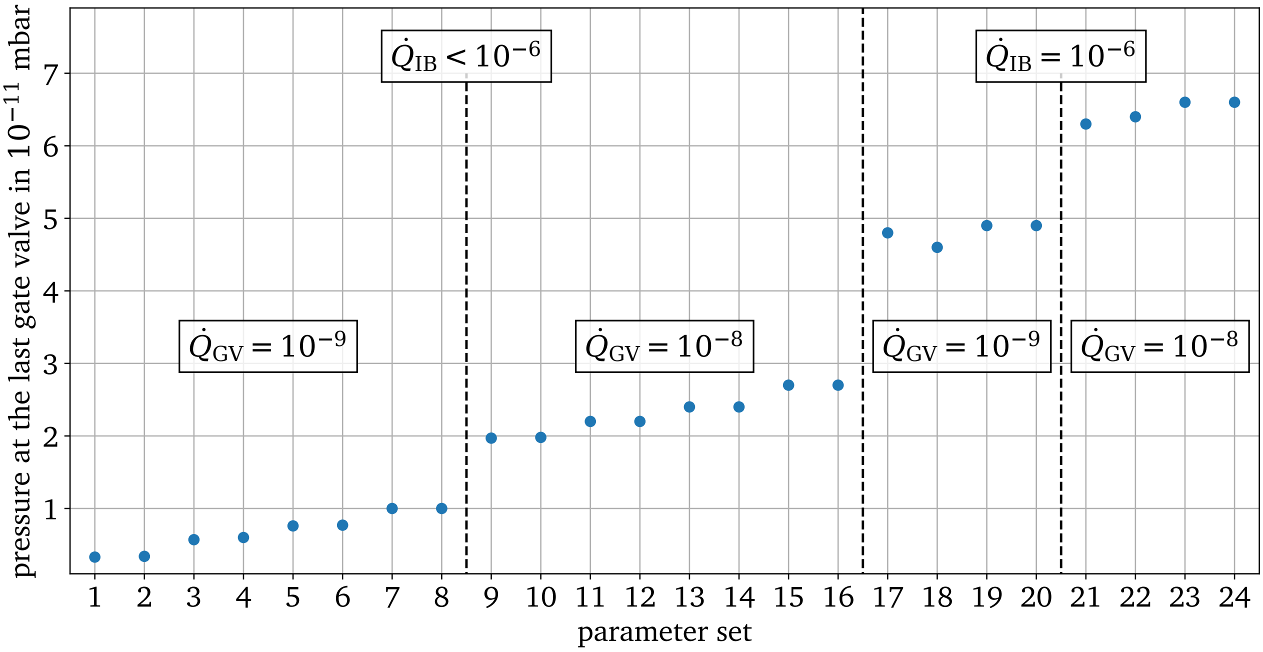

Figure 2.15.: The pressure for different parameter sets (see Tab. 2.3). The flows $\dot{Q}_i$ are given in mbar l/s. Pressures below $1 \cdot 10^{-11}$ mbar are achieved with $\dot{Q}_{\text{IB}} < 10^{-7}$ mbar l/s and $\dot{Q}_{\text{GV}} = 10^{-9}$ mbar l/s.

Table 2.3.: The parameter sets shown in Fig. 2.15. All flows $\dot{Q}_i$ are given in mbar l/s and p in 10^{-11} mbar.

set	$\dot{Q}_{\text{IB}}$	N_{pumps}	$\dot{Q}_{\text{GV}}$	$\dot{Q}_{\text{PDT}}$	p
1	0	5	10^{-9}	10^{-8}	0.33
2	0	3	10^{-9}	10^{-8}	0.34
3	0	5	10^{-9}	10^{-7}	0.57
4	0	3	10^{-9}	10^{-7}	0.6
5	10^{-7}	5	10^{-9}	10^{-8}	0.76
6	10^{-7}	3	10^{-9}	10^{-8}	0.77
7	10^{-7}	5	10^{-9}	10^{-7}	1
8	10^{-7}	3	10^{-9}	10^{-7}	1
9	0	5	10^{-8}	10^{-8}	1.97
10	0	3	10^{-8}	10^{-8}	1.98
11	0	5	10^{-8}	10^{-7}	2.2
12	0	3	10^{-8}	10^{-7}	2.2
13	10^{-7}	5	10^{-8}	10^{-8}	2.4
14	10^{-7}	3	10^{-8}	10^{-8}	2.4
15	10^{-7}	5	10^{-8}	10^{-7}	2.7
16	10^{-7}	3	10^{-8}	10^{-7}	2.7
17	10^{-6}	5	10^{-9}	10^{-8}	4.8
18	10^{-6}	3	10^{-9}	10^{-8}	4.6
19	10^{-6}	5	10^{-9}	10^{-7}	4.9
20	10^{-6}	3	10^{-9}	10^{-7}	4.9
21	10^{-6}	5	10^{-8}	10^{-8}	6.3
22	10^{-6}	3	10^{-8}	10^{-8}	6.4
23	10^{-6}	5	10^{-8}	10^{-7}	6.6
24	10^{-6}	3	10^{-8}	10^{-7}	6.6

To understand to which of the parameters the pressure is most sensitive, the pressure increase stemming from one parameter changing was calculated. The increase in pressure for a change in one of the parameters is given by

$$\Delta p_1 = p_1(a, b, c, d_1) - p_1(a, b, c, d_2). \tag{2.5}$$

For example the change in pressure originating from an increase in gate valve outgassing $\dot{Q}_{\text{GV}}$ from 10^{-9} mbar l/s to 10^{-8} mbar l/s, with $\dot{Q}_{\text{IB}} = 10^{-7}$ mbar l/s, $N_{\text{pumps}} = 3$ and $\dot{Q}_{\text{PDT}} = 10^{-8}$ mbar l/s is given by

$$\Delta p_1 = \text{parameter set 14} - \text{parameter set 6} = 1.63\,\text{mbar}. \tag{2.6}$$

The pressure increase Δp_1 for all combinations of parameter sets where one parameter is changed is shown in Fig. 2.16.

Remarkably, the pressure increase caused by the change of one parameter is independent of the other parameters. This behavior can be explained by modeling the pressure at the last gate valve with a very simplified equivalent circuit (see Fig. 2.17). At the last gate valve the pressure p_1 is influenced by the outgassing $\dot{Q}_0$, the pumping speed S and the pressure p_0 upstream of a pipe with conductance C. $\dot{Q}_0$ corresponds to $\dot{Q}_{\text{GV}}$, and N_{pumps}, $\dot{Q}_{\text{IB}}$, and $\dot{Q}_{\text{PDT}}$ only contribute to p_0.

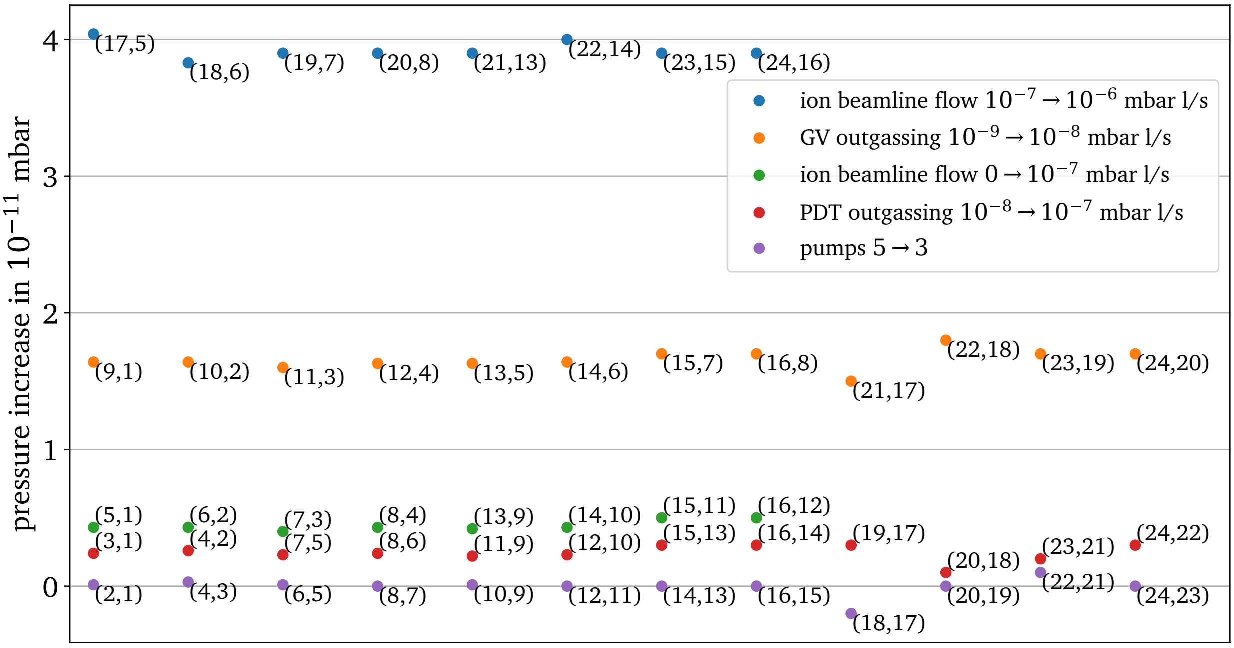

Figure 2.16.: The increase in pressure at the last gate valve for different combinations of outgassing and pumping, varying one parameter each time. The pressure increase is calculated as $\Delta p_1 = p_1(a,b,c,d_1) - p_1(a,b,c,d_2) =$ parameter set $i -$ parameter set j with (i,j) indicated at each point. The sets i and j have all parameters in common except the one indicated by the color.

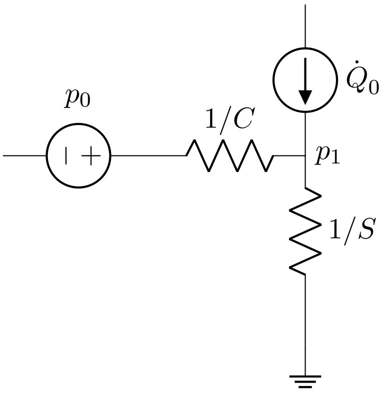

Figure 2.17.: A simplified electrical network model at the last gate valve, including only a conductance C, with a pressure p_0 upstream, outgassing of $\dot{Q}_0$ and pumping S. With this, the pressure at the last gate valve p_1 can be calculated.

The pressure p_1 at the last gate valve can be calculated analytically

$$p_1 = \frac{Cp_0}{C+S} + \frac{\dot{Q}_0}{C+S}. \tag{2.7}$$

As we are interested in the pressure change with respect to the pressure upstream $p_0(N_{\text{pumps}}, \dot{Q}_{\text{IB}}, \dot{Q}_{\text{PDT}})$

and the outgassing $\dot{Q}_0 = \dot{Q}_{\mathrm{GV}}$, we look at the partial derivatives

$$\frac{\partial p_1}{\partial p_0} = \frac{C}{C+S}, \tag{2.8}$$

$$\frac{\partial p_1}{\partial \dot{Q}_0} = \frac{1}{C+S}. \tag{2.9}$$

Because the derivatives only depend on the conductance C and pumping speed S, the change in the upstream parameters will always lead to a constant change in pressure, independent of the absolute pressure. As can be seen in Fig. 2.16, the pressure increases are constant for the variation of a single parameter. This means, that the gain in pressure for one parameter is independent of the other, which makes optimizing the system much easier. Broadly speaking, twice as much effort can be spent on reducing the flow from the ion beamline from 10^{-6} mbar l/s to 10^{-7} mbar l/s than on reducing the outgassing of the gate valves from 10^{-8} mbar l/s to 10^{-9} mbar l/s. Additional ion pumps would only have a minor impact.

In addition to the parameter study, the influence of different pump types at the pulsed drift tube was investigated. Two ion pumps were compared with two NEG cartridges and with one ion-NEG-combination pump (see Fig. 2.18). The pumps were placed underneath the pulsed drift tube assembly and in the case of the ion-NEG-combination pump under the high-voltage einzel lens. Considering only hydrogen, the pressure is directly proportional to the hydrogen pumping speed. Consequently, it reaches its peak with ion pumps and is at its lowest with ion-NEG-combination pumps. Bundling the pumping speed within a single pump does not impact the downstream pressure. The decision was taken to use one D2000-10, because of the availability and lower price. The lower pumping speed of hydrocarbons should not be a problem, as no such materials are used for the pulsed drift tube.

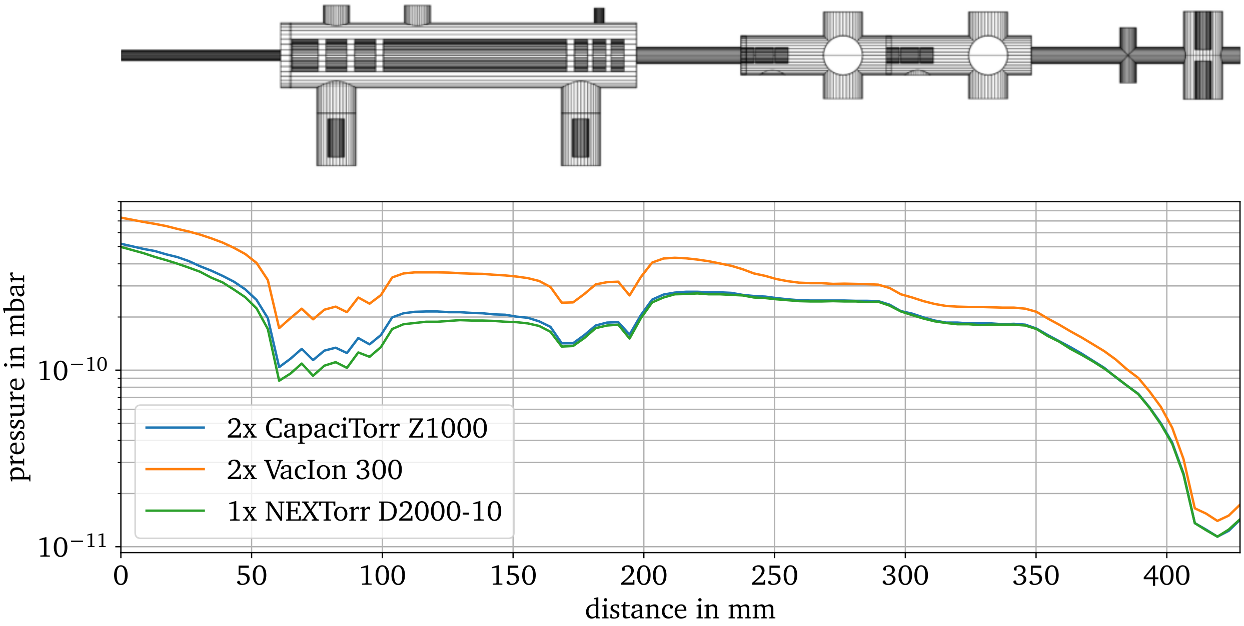

Figure 2.18.: Comparison between ion-, NEG-, and ion-NEG-combination pumps at the pulsed drift tube. As only hydrogen is considered, the pressure scales with the hydrogen pumping speed. Therefore, it is highest for the ion pumps, and lowest for the ion-NEG-combination pump. Concentrating the pumping speed in one pump does not have an effect on the pressure downstream.

2.4.3. Vacuum Measurements

The vacuum of section 1 and 2 was measured to confirm the success of the NEG coating and benchmark the simulations. Section 1 was tested in place in the PUMA experimental area. With the NEG coating activated and the pulsed drift tube not in operation, a pressure of $\sim 2 \cdot 10^{-11}$ mbar was reached. Section 2 was tested in the CERN vacuum lab. Without the SEM grid installed, a pressure of $\sim 5 \cdot 10^{-11}$ mbar was reached. The pressure was measured with Pfeiffer IKR 070 gauges calibrated for N_2. Judging from these measurements, a vacuum of $\sim 1 \cdot 10^{-11}$ mbar at the last gate valve is possible. The final confirmation will come, once the PUMA trap setup is installed, since the NEG cross, essential to achieve this pressure at the last gate valve, is mechanically mounted to the transportable frame.

2.5. Pulsed Drift Tube

Figure 2.19 shows the working principle of a pulsed drift tube (PDT). The bunch is decelerated by the field gradient entering the drift tube. While in the field-free region of the drift tube, the potential is lowered. When exiting the drift tube, there is no gradient between the drift tube an the next (grounded) electrode, and the bunch is not accelerated on exit.

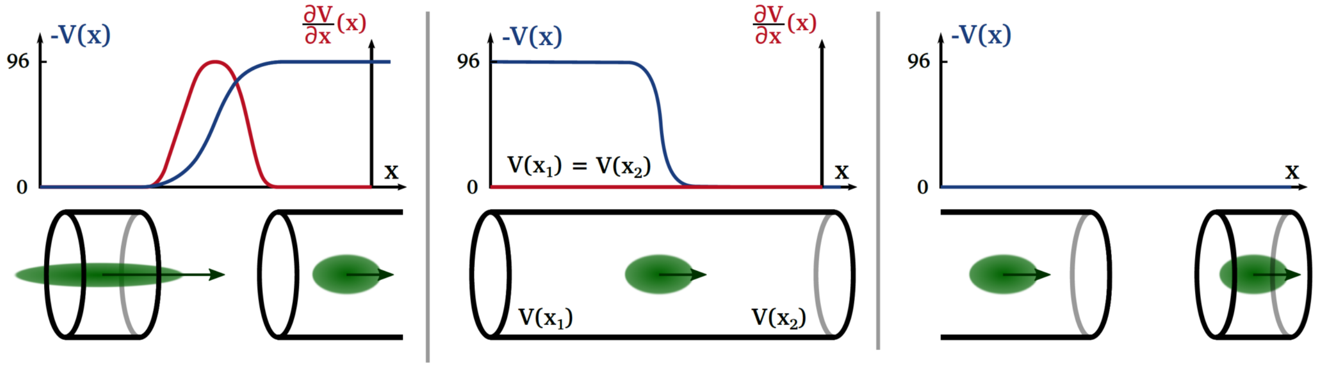

Figure 2.19.: Working principle of a pulsed drift tube. The bunch is decelerated by the field gradient in front of the drift tube. While in the field-free region of the drift tube the potential is lowered. When exiting the drift tube, there is no gradient between the drift tube and the next (grounded) electrode, and the bunch is not accelerated on exit. Figure from [86] under CC BY 4.0.

The pulsed drift tube used for the PUMA experiment, is based on the design proposed by GBAR [113]. It consists of the drift tube, a high-voltage (maximum -90 kV) einzel lens in front, and a low-voltage (maximum ±5 kV) einzel lens behind (see Fig. 2.20). The einzel lenses are needed to focus the beam into and out of the drift tube. Because the drift tube itself acts like lens, the high-voltage einzel lens is needed, so that together they act like a telescope. The drift tube has to accommodate a radial expansion of the beam. The inner diameter was thus chosen to be 100 mm with an outer diameter of 120 mm. An antiproton bunch from ELENA has a length of $t_{\text{bunchlength}} = 75\,\text{ns}$ (1σ) [109]. Decelerated to $E_{\text{kin}} = 4\,\text{keV}$, this corresponds to a length of 263 mm.

$$E_{\text{kin}} = \frac{1}{2}mv^2 = 4\,\text{keV} \tag{2.10}$$

$$s = vt = \sqrt{\frac{2E_{\text{kin}}}{\text{m}_{\bar{\text{p}}}}} \cdot t_{\text{bunchlength}} \approx 263\,\text{mm}^{\dagger} \tag{2.11}$$

The PUMA pulsed drift tube is 700 mm long. This ensures, that the bunch is in the field free region of the drift tube when the potential is changed. For the choice of material see Sec. 2.4.

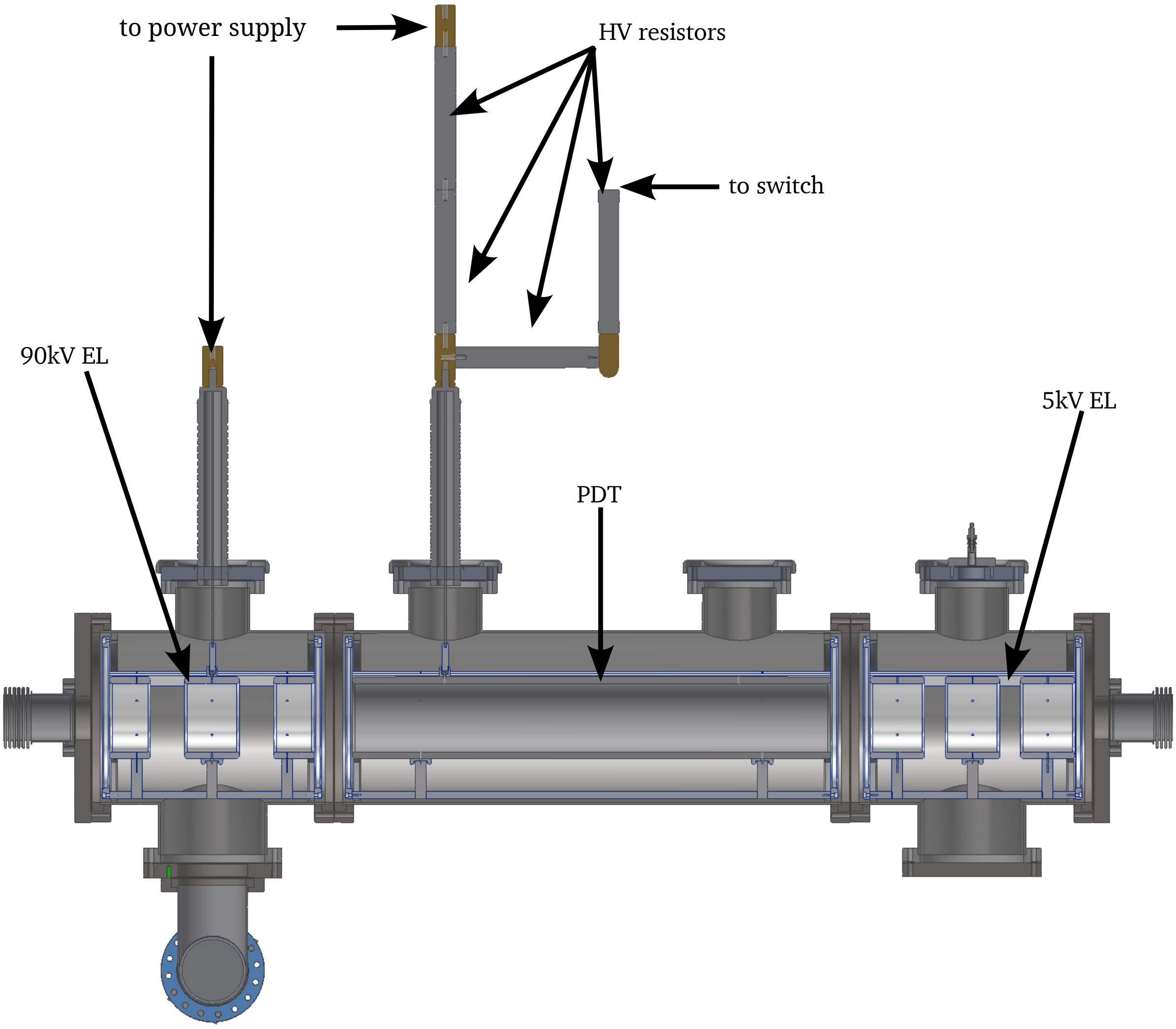

Figure 2.20.: Half section cut view of the pulsed drift tube assembly. The pulsed drift tube assembly consists of the drift tube and a high-voltage (-90 kV) einzel lens in front and a low-voltage (±5 kV) einzel lens behind.

The walls of the vacuum chambers are coated with a non-evaporable getter (NEG) to pump the section. The coating of the inside surfaces of the chambers was done at CERN. The installation of the pulsed drift

---

[†] I use $\text{m}_\text{p} = \text{m}_{\bar{\text{p}}}$, for further details see BASE and colleagues [138].

tube inside the chamber must be done with great care to avoid damaging the coating. It is first mounted onto its support structure before being lowered vertically into the vacuum chamber and secured with screws (see Fig. 2.21). To facilitate individual access to the high- and low-voltage einzel lens as well as the drift tube, the vacuum chamber is divided into three parts.

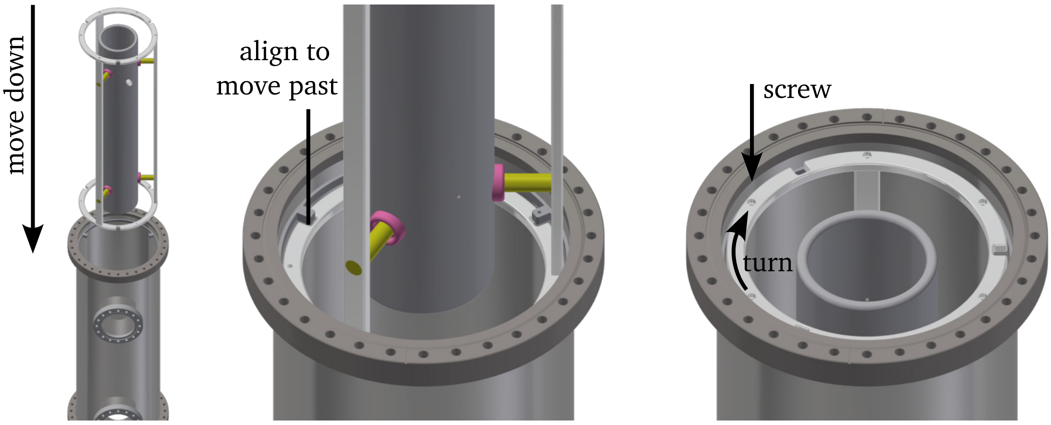

Figure 2.21.: Mounting procedure of the drift tube and einzel lenses in the vacuum chambers. This way, the NEG coating on the chamber walls is not damaged.

2.5.1. High-voltage Considerations

To decelerate the antiprotons from 100 keV to 4 keV a potential of -96 kV is needed on the drift tube. Consequently, high voltage must be taken into account. On all components, sharp edges have been avoided, and the electrodes have been polished to an average surface finish of $R_\mathrm{a} = 0.05\,\mu\mathrm{m}$, which helps to prevent discharges [139]. The assembled high-voltage einzel lens is shown in Fig. 2.22.

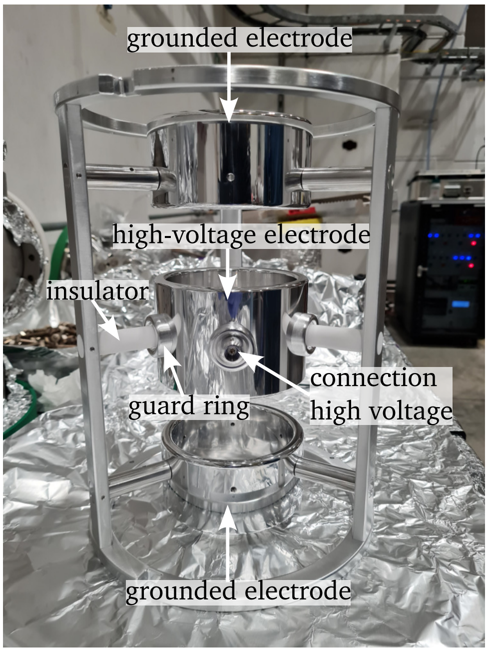

Figure 2.22.: Assembled high-voltage einzel lens. The electrodes have been polished to an average surface finish of $R_\mathrm{a} = 0.05\,\mu\mathrm{m}$.

At the intersections of vacuum, conductor and insulator, the electric field is strongly enhanced due to gaps arising from imperfections on the corners of the material (see Fig. 2.23). Special attention has been paid to these so-called triple junctions to prevent possible discharges [140]. They are shielded by rings that surround the triple junction and thereby lower the electric field (see Fig. 2.23).

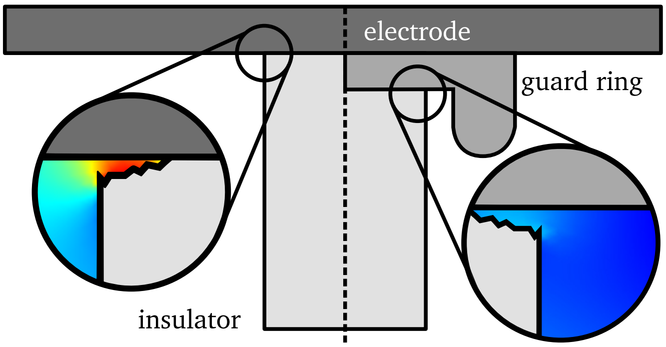

Figure 2.23.: The field strength at an unshielded triple junction (left) and one shielded with a guard ring (right) is illustrated here. Blue indicates lower and red higher electric field strengths. Figure adapted from [119] under CC BY 4.0.

Electronics

To not reaccelerate the antiprotons as they exit the pulsed drift tube, it must be discharged from -96 kV to 0 V before the first antiprotons exit the field-free region. The time to discharge the drift tube is given by the time between the last antiprotons entering and the first ones exiting. With the velocity v (see Eq. 2.11) and the length l of the drift tube and the bunch, the time to discharge is in the order of 500 ns for antiprotons with a kinetic energy of 4 keV.

$$t_{\text{last enter}} - t_{\text{first exit}} = \frac{l_{\text{PDT}} - l_{\text{bunch}}}{v} \approx 500\,\text{ns}. \tag{2.12}$$

Equipment, such as cables and resistors, that can withstand high voltages and high peak currents, as well as a high-voltage switch with a short transient ($\sim 10\,\text{ns}$), are needed. The pulsed drift tube is connected to a high-voltage power supply (Spellman SL130PN60, maximum current of 450 μA) via a $1\,\text{M}\Omega$ resistor (see Fig. 2.24). The high-voltage einzel lens is connected to a Spellman SL100PN10, with a maximum current of 100 μA.

In order not to exceed the voltage rating of the resistors, two Metallux HVR 969 resistors are used, connected via polished brass cylinders with rounded edges. The resistor value of $1\,\text{M}\Omega$ is chosen as a compromise between the need for a high resistance to decouple the power supply from the pulsed drift tube while switching, and the need for a low resistance to minimize the effects of current fluctuations on the voltage applied to the pulsed drift tube. For the discharge of the tube's capacitance, a fast high-voltage switch (Behlke HTS 1501-20-LC2, $I_{\text{pmax}} = 200\,\text{A}$, $R_{\text{stat}} = 28\,$, $t_{\text{r}} = 1\ldots 20\,\text{ns}$) connects the pulsed drift tube to ground. To make sure that the switch is not damaged, the pulsed drift tube is connected to the switch via a two $250\,\Omega$ Metallux HVR 969 resistors in series, limiting the current. Because the switch is a single pole single throw (SPST) switch, to discharge the drift tube, after switching the power supply output is connected to ground. The high-voltage leads are connected with HN-70 connectors from R.E. Beverly III & Associates. As high-voltage feedthrough, a HV125R-CE-CU39 from VACOM is used, rated for up to 125 kV. The cables are suspended from the ceiling to avoid triple junctions at the exposed high-voltage connectors.

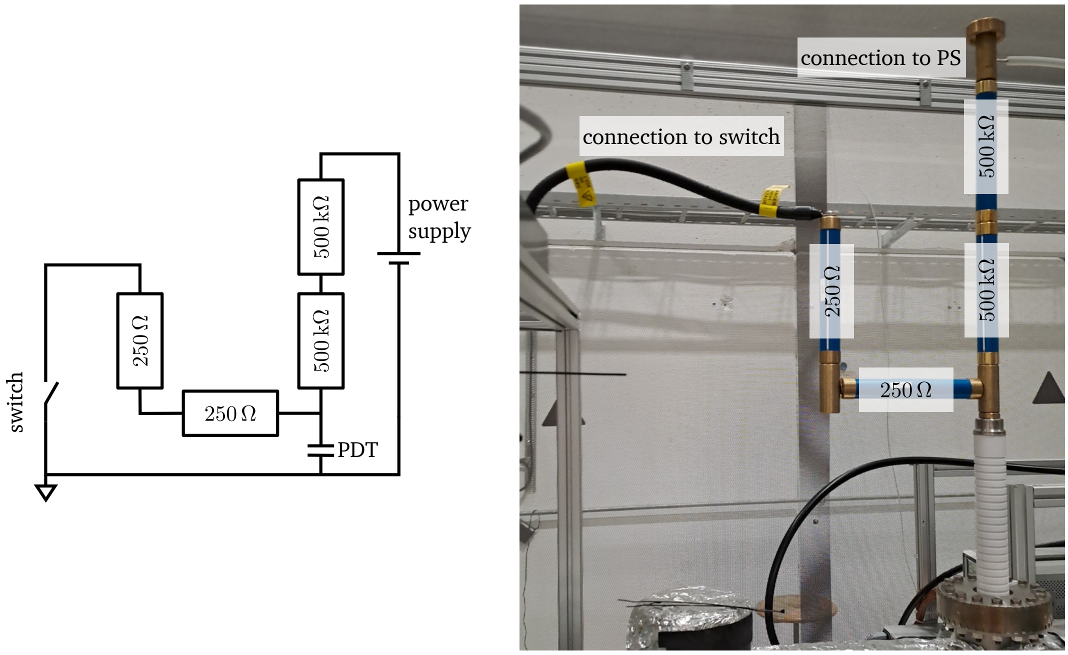

Figure 2.24.: Left: Circuit diagram for the PDT electrical installation. Because the switch is a single pole single throw (SPST) switch, to discharge, the power supply is also connected to ground. Right: Picture of the implementation of the high-voltage circuit.

The cable's grounded mesh is removed on the load side, and special care is taken to cover the pointy ends of the grounded mesh with copper tape (see Fig. 2.25).

Figure 2.25.: The grounded mesh is removed on the load side, and special care is taken to cover the pointy ends of the grounded mesh with conductive (copper) tape.

Using a 1/1000 voltage divider (LeCroy PPE6kV) connected to a Tektronix MDO3104 oscilloscope, the switching time from -5 kV to ground was measured. As can be seen in Fig. 2.26, there is a ~250 ns delay between the trigger signal from the waveform generator (blue) and the voltage on the pulsed drift tube (orange) which has to be taken into account when triggering the switch. Independent of the voltage applied to the switch, the transient time τ to V_0/e is ~80 ns. This is consistent with the time constant estimated by a simple RC-circuit and within the specifications of the switch:

$$\tau = RC = 500\Omega \cdot 170\text{pF} = 85\,\text{ns}, \tag{2.13}$$

where the capacitance of the pulsed drift tube was measured.

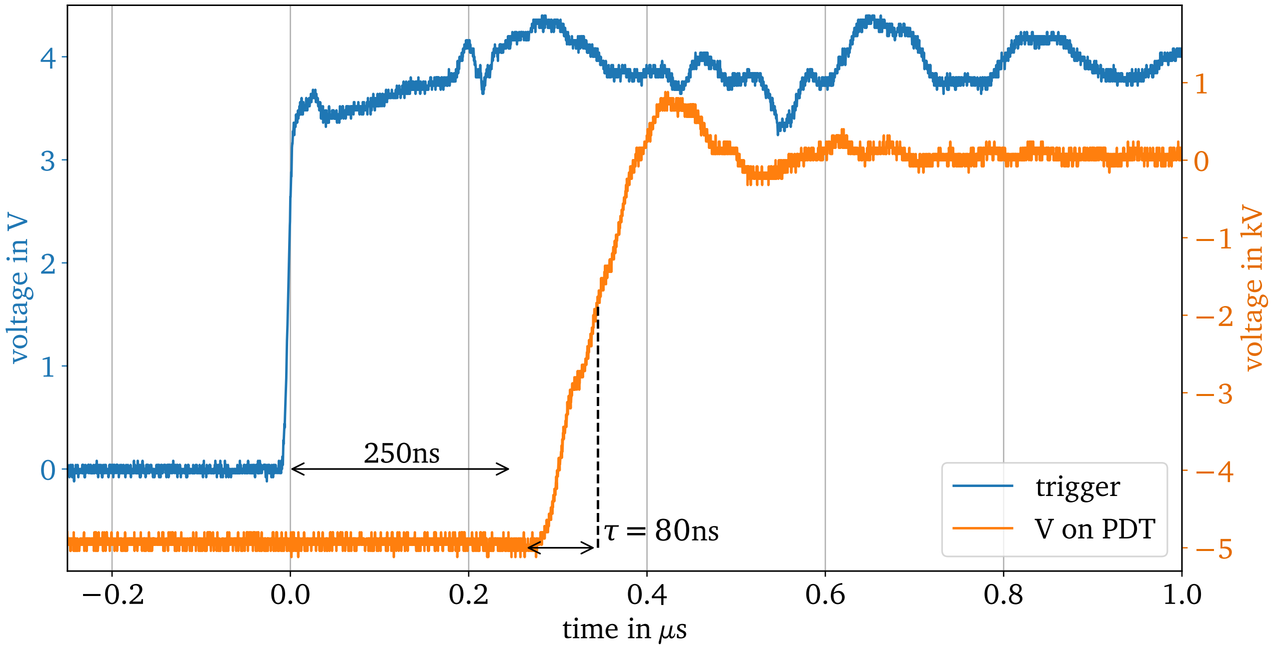

Figure 2.26.: Switching time while switching from 5kV to ground, measured with a 1/1000 voltage divider. The trigger signal is shown in blue and the voltage on the pulsed drift tube in orange. Figure adapted from [119] under CC BY 4.0.

Safety Cage

The high-voltage system has unshielded high-voltage connections up to 100 kV exposed to air during operation. Therefore, the safety of the users has to be ensured by a safety cage according to the ingress protection code level IP3X. Following the European norm EN 50191, the dimensions of the safety cage are defined so that any high-voltage point in air is at a distance of more than 74 cm from the cage. This corresponds to a maximum voltage of 130 kV, the maximum voltage of the drift tube high-voltage power supply (see Fig. 2.27).

The high-voltage system is interlocked via a switch (Telemecanique XCSDMC7902 coded magnetic switch) at the sliding door of the cage to interlock the power supplies in the event of unexpected access while the equipment is powered. The safety cage is further secured with a trapped key system from Allen Bradley (Rockwell) to prevent unauthorized access. The door must first be locked to use the key to connect the high-voltage power supplies to the power grid (mains). To simplify maintenance work, panels can be removed from all sides of the cage. The cage is built from aluminum profiles and panels of perforated steel sheets.

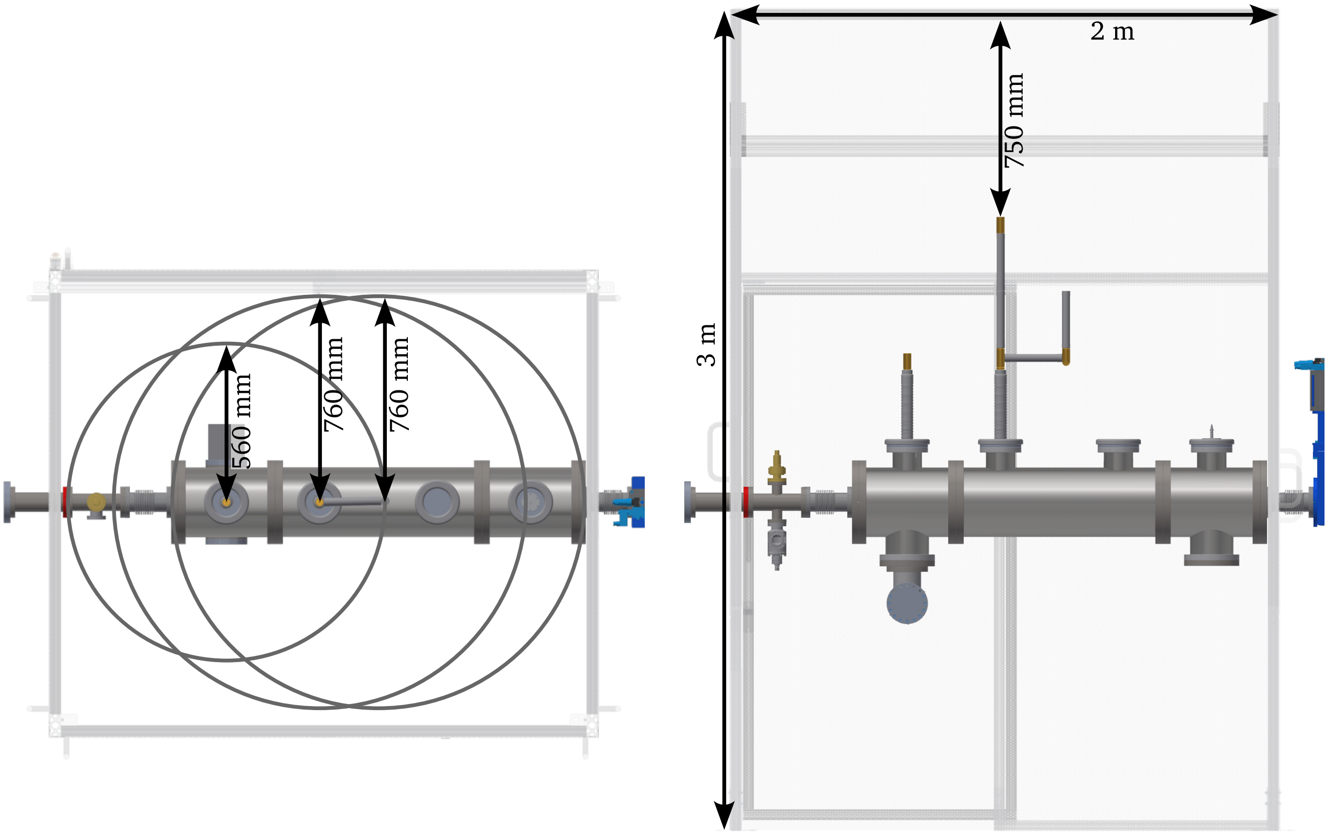

Figure 2.27.: Left: A top-down view of the safety cage. The distances correspond to the minimum distances for 130 kV (PDT) and 100 kV (HV EL) respectively according to EN 50191. Right: A side view of the safety cage. The distance to the ceiling is not critical for user safety, and therefore not dictated by EN 50191.

2.5.2. High-voltage Conditioning

When high voltage is applied, surface contamination and imperfections can cause discharges that degrade the vacuum and material. Instead of leading to discharges, they can also result in a leakage current that drains the set potential. To counter this, conditioning the high-voltage parts is essential before operating the pulsed drift tube. It was done by a step-wise increase of the voltage, while keeping the leakage current below the limit of the power supply and the vacuum better than $5 \cdot 10^{-8}$ mbar most of the time, as not to trigger the gate valve interlock ($5 \cdot 10^{-7}$ mbar).

The pulsed drift tube and high-voltage einzel lens were conditioned over several weeks. The voltage was increased step by step and left in static operation until the sudden spikes in current, associated with field emission from imperfections on the electrode, subsided. This took between 12 and 72 hours per voltage step.

As an illustration of the current, voltage and pressure behavior, part of the conditioning of the new high-voltage einzel lens is shown (see Fig. 2.28). First, when increasing the voltage, there is a spike in current (up to the current limit) to charge the capacitance of the electrode. As the current is needed to charge the drift tube, these current spikes are not associated with pressure increases. When increasing the voltage, there is the possibility of a spark originating from a surface contamination or imperfection. These events are characterized by a spike in current, a drop in voltage and, if the spark happens inside the vacuum, a spike in pressure. In this example, the first spark happens when going over -80 kV. Here, many sparks follow and after they subside the voltage is increased further to repeat the procedure.

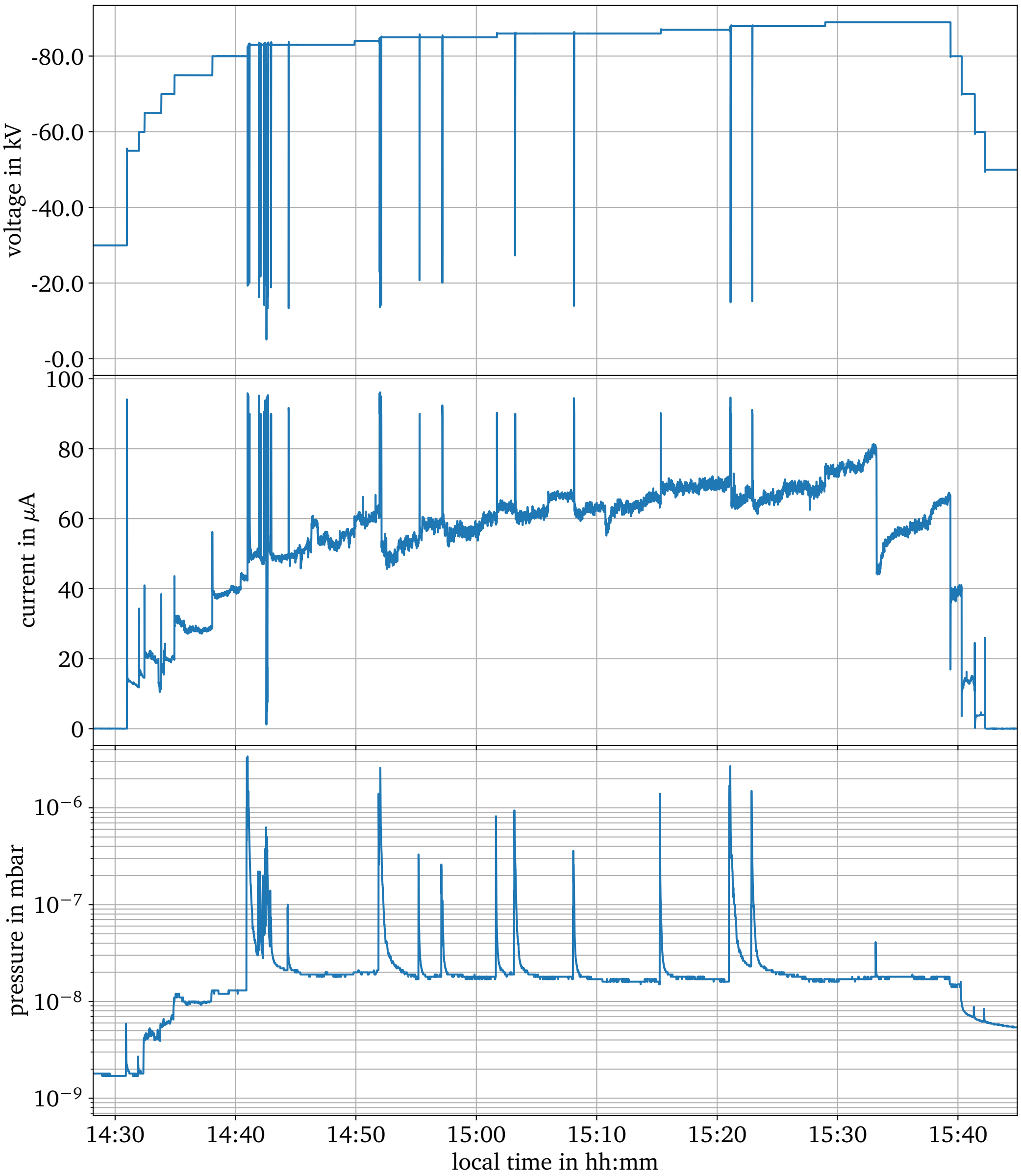

Figure 2.28.: From top to bottom: the voltage, current and pressure during a part of the high-voltage einzel lens conditioning. When increasing the voltage, there is a spike in current (up to the current limit) to charge the capacitance of the electrode. In the pressure these spikes are not associated with any spikes. When going over -80 kV, the first spark happens, corresponding to a drop in voltage, a spike in current and pressure (if it is inside the vacuum). Many sparks follow and after they subside the voltage is increased further.

For voltages above -92 kV, the pulsed drift tube showed a different behavior, recorded in Fig. 2.29. When increasing the voltage for the first time, it only rises slowly, the current is at the limit, and the pressure high. The voltage drops many times, interpreted as discharges. Once the set voltage is reached, the current drops to the expected value. Setting the voltage down and back up again, this phenomenon does not happen again.

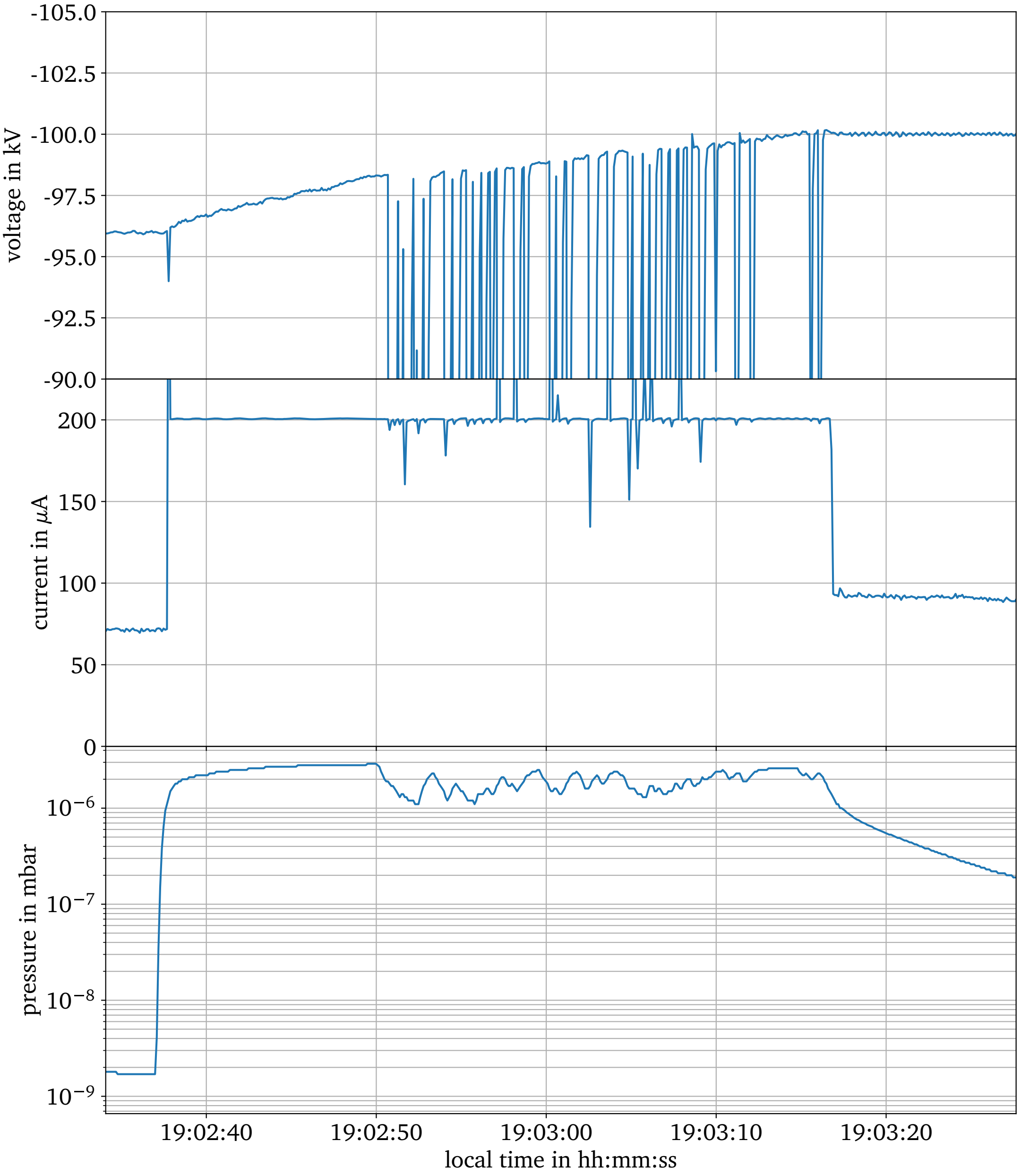

Figure 2.29.: Voltage, current and pressure when increasing the voltage from -96 kV to -100 keV for the first time. When increasing the voltage, it only rises slowly, the current is at the limit, and the pressure high. The voltage drops many times, interpreted as discharges. Once the set voltage is reached, the current drops to the expected value. Setting the voltage down and back up again, this phenomenon does not repeat.

Besides the spikes in current, there is a constant leakage current from high voltage parts to ground. To determine whether the current is flowing inside or outside the vacuum, Fig. 2.30 shows the pressure-current correlation for the drift tube (top) and the high-voltage einzel lens(bottom). The assumption is, that a flow of current from the electrodes to ground will cause the pressure to rise by impact ionization. From these it follows, that the leakage current originates inside the vacuum in the case of the einzel lens and in case of the drift tube it originates outside.

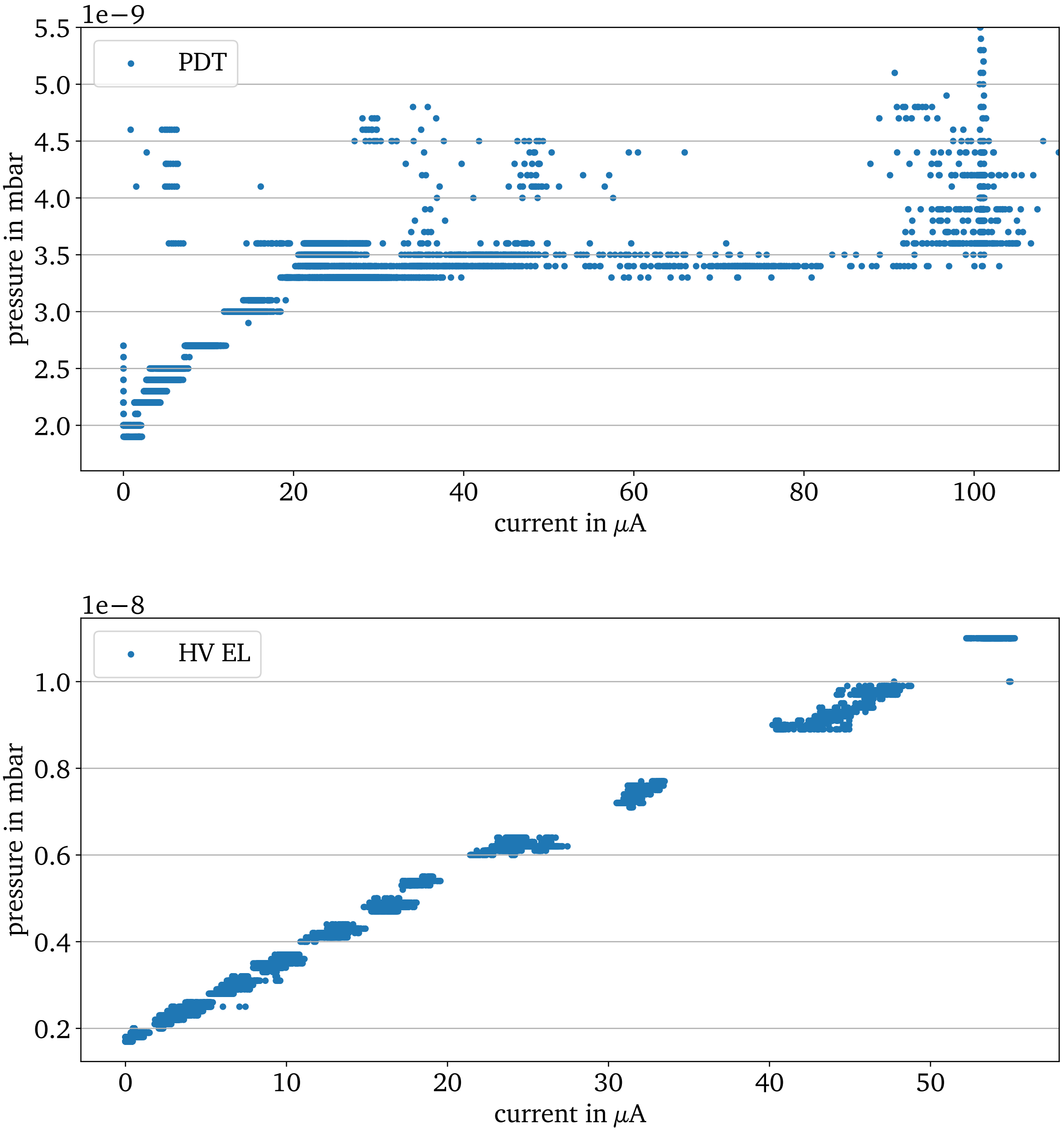

Figure 2.30.: Pressure-current correlation of the drift tube (top) and the high-voltage einzel lens (bottom). The source of leakage current is inside the vacuum chamber in the case of the HV EL and outside in the case of the drift tube.

The efforts to reduce the leakage current originating outside the vacuum can be summarized by three methods: increasing the distance between exposed high-voltage parts and ground, increasing the curvature of pieces in high electric fields, and polishing them. In particular, the leakage current at -96 kV could be lowered from 100 µA to 50 µA by polishing and increasing the corner radius of the connector between the two resistors connecting to the switch from 3 mm to 15 mm. The connector was produced twice, once from aluminum and once from brass. The choice of material makes no difference to the leakage current. Additionally, the current could be further decreased to 11 µA by increasing the ceiling height of the safety cage by 50 cm to 75 cm (see Fig. 2.31). Another measure was to cover the screws of the vacuum flanges with an aluminum cover.

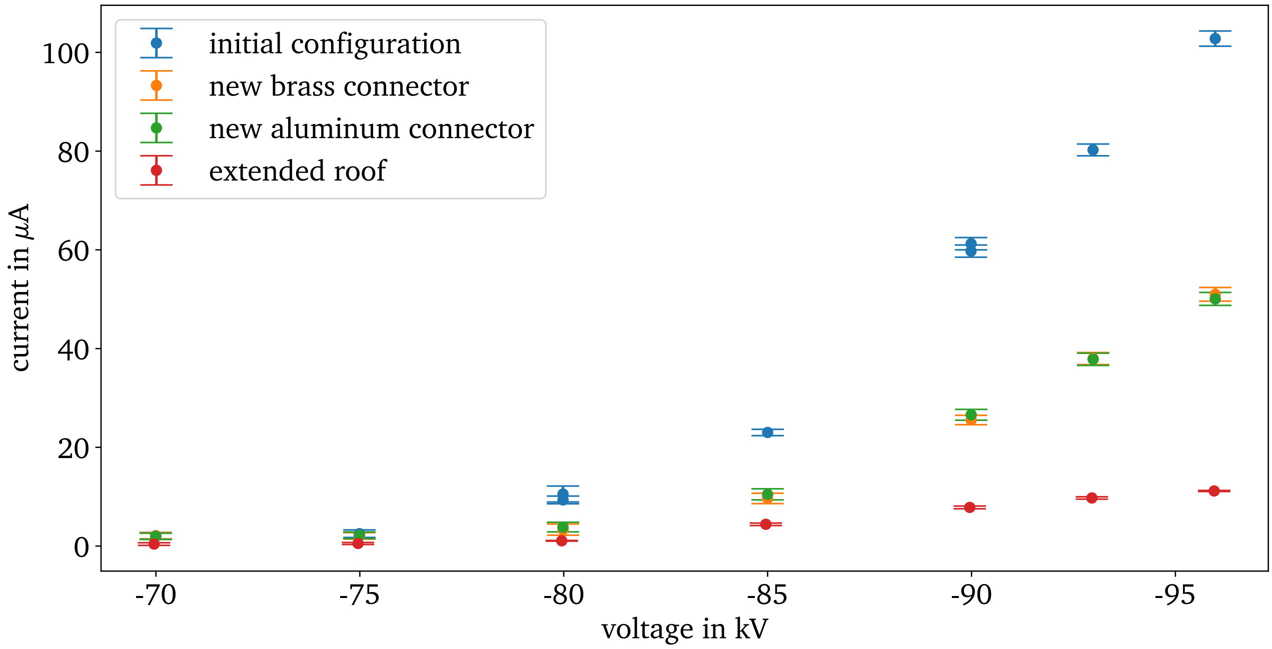

Figure 2.31.: Reduction of leakage current by increasing the corner radius of the connector between the two resistors connecting to the switch from 3 mm to 15 mm and additionally increasing the ceiling height of the safety cage by 50 cm to 75 cm. The choice of material does not influence the leakage current.

For the high-voltage einzel lens, it was decided that it had to be replaced with a new one with increased distance between the high-voltage and the grounded electrodes and polished to a higher degree. Unfortunately, even with the new HV EL, the leakage current could not be reduced in the same way as for the drift tube. The desired value of -89 kV was reached, with a current of around 80 µA. Even though the current of the HV EL degrades the vacuum do a higher extent than the PDT, with the ramping scheme implemented where the voltage is increased only shortly before the antiprotons arrive (see Sec. 2.5.3), the HV EL can be used.

2.5.3. Vacuum During Operation

During operation of the pulsed drift tube, the remaining leakage current inside the vacuum degrades the pressure. To mitigate this, as done by the GBAR collaboration, the voltage is kept at 0 V for most of the AD cycle and is increased to -96 kV only 9.5 s before a bunch of antiprotons arrives.

The ramping of the high voltage is triggered by the signal corresponding to the injection of the bunch from the AD into ELENA (*AEX.PUMA-INJ*). It gives a 9.5-second notice. This triggers a ramp of the high-voltage power supply. The steps are -70 kV, -80 kV, -90 kV, -93 kV and -96 kV for the drift tube and scaled to its voltage for the high-voltage einzel lens. The time between steps is 1.5 s and after 5 s on V_{set}, the voltage is put to 0 again. Ramping up the voltage only shortly, compared to a repetition time of 120 s for ELENA, before the bunch arrives reduces the impact on the pressure. The current is also zero for most of the time and therefore prevents material degradation. When -96 kV are applied to the drift tube, the pressure reaches a value of $\sim 8 \cdot 10^{-10}$ mbar and increases to $\sim 2 \cdot 10^{-9}$ mbar when switching (see Fig. 2.32).

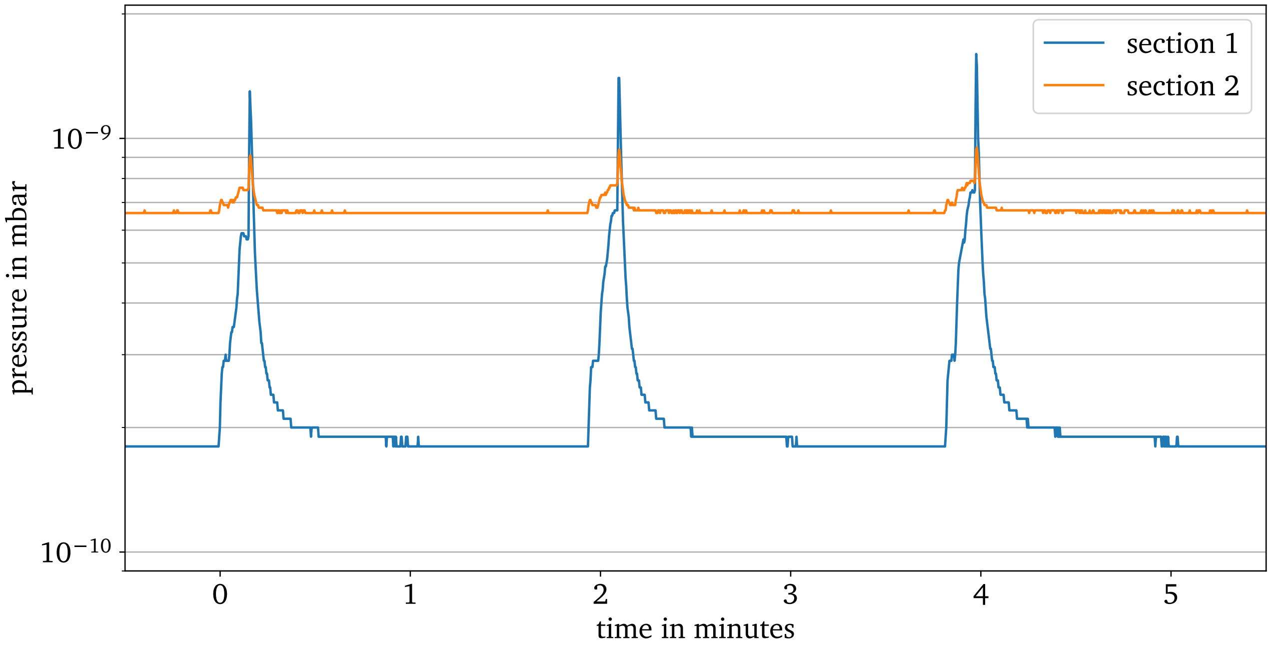

Figure 2.32.: The pressure in section 1 and 2 (see Fig. 2.3) during three AD cycles. The voltage on the HV EL is zero. The vacuum gauge for section 1 is situated 260 mm upstream of the pulsed drift tube and the section 2 gauge is at the position of the quadrupole bender. Figure adapted from [119] under CC BY 4.0.

Because the high-voltage einzel lens has a higher leakage current than the drift tube, the vacuum is worse when using it (see Fig. 2.33). The pressure downstream in section 2 is less affected by the increase. Since the pressure is still well below the interlock threshold to close the gate valve at the handover point to LNE51 ($p_{\text{th}} = 5 \cdot 10^{-7}$ mbar), the beamline could be commissioned with beam.

How exactly the ramping and switching of the HV EL and PDT affect the pressure at the last gate valve remains to be seen, especially because these test were done without the NEG coating activated, to conserve it for use with the trap attached. Still, because the source of the outgassing, the drift tube and einzel lens are far from the PUMA Penning trap, the expected effect is small. This is supported by the simulation of the effect of an increase in pressure at the handover point (see Fig. 2.9) and the muted response in section 2 (see Fig. 2.33). With the NEG coating activated, the surge is expected to be smaller and the increase downstream more muted, making a pressure of $\sim 1 \cdot 10^{-11}$ mbar possible.

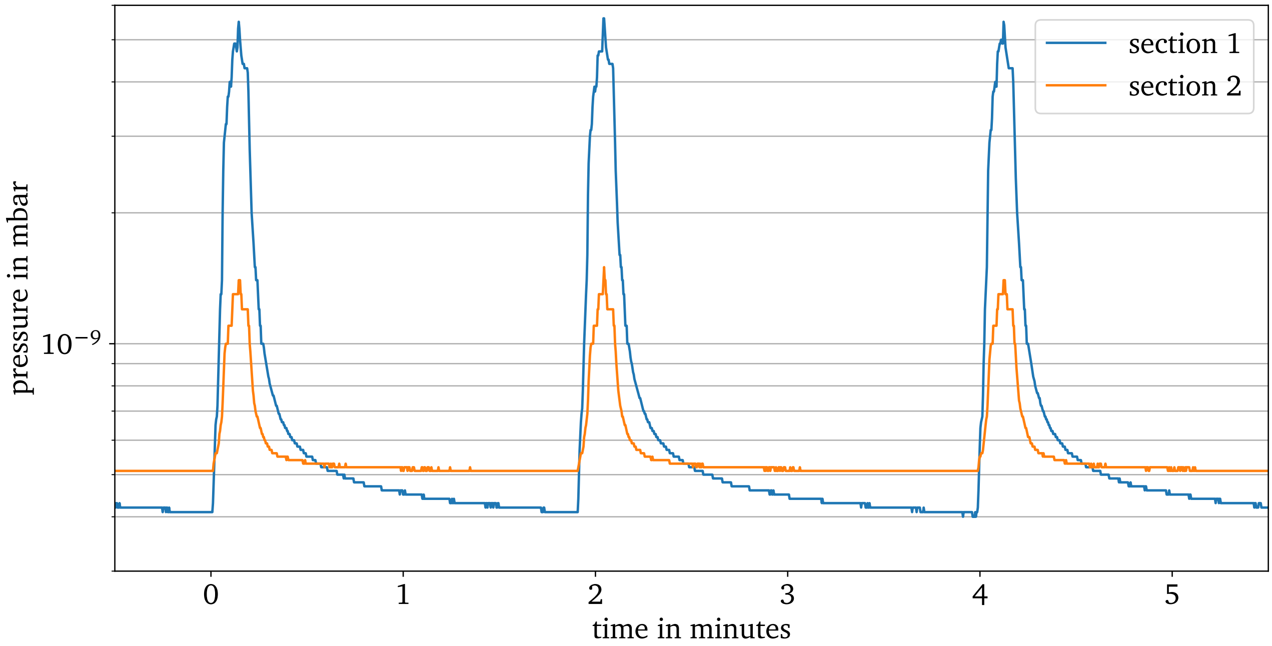

Figure 2.33.: The pressure in section 1 and 2 during three AD cycles. The voltage of both the HV EL and PDT is increased 10 s before the antiproton bunch arrives, leading to the increase in pressure.

2.6. Measurement of Beam Properties

2.6.1. Detection System

For the characterization of the system, a vacuum chamber with several detectors was installed at the end of the beamline (see left panel of Fig. 2.34). To visualize the beam spot, a microchannel plate (MCP) by Hamamatsu with a phosphor screen that has a diameter of 40 mm was used (see right panel of Fig. 2.34).

An MCP consists of one or more plates with microchannels that have a diameter of $d \sim 10\,\mu\text{m}$. The channels are tilted at an angle of 5° to 15° to the axis perpendicular to the plate surface (see Fig. 2.35). This angle is called the bias angle. In each channel, the incoming charge hits the wall and releases secondary electrons, which are accelerated, also hit the channel wall and are multiplied. This results in an amplification, or gain, of up to $3 \cdot 10^4$. The gain can be adjusted by changing the voltage applied between the MCP surfaces and can be increased by stacking two or more MCPs. Here, the MCPs are arranged so that the channels form a ”V” (or chevron). A two-plate MCP array has a gain of up to 10^7. The multiplied charges can be converted to light with a phosphor screen and then imaged with a CCD camera.

The open area ratio (OAR) of an MCP gives the fraction of channel opening area to the total area. It is typically 60%, meaning a fraction of 40% of the incoming particles misses the channels and does not contribute to the signal.

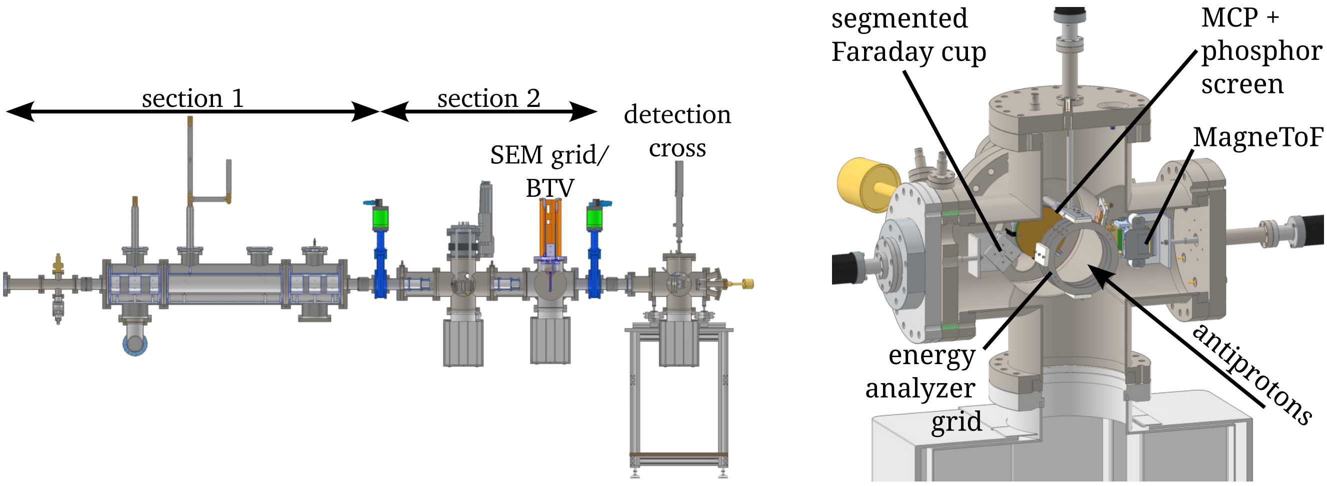

Figure 2.34.: Left: The antiproton beamline as commissioned with the detection cross. Right: The detection cross used for commissioning of the antiproton beamline. The MCP with phosphor screen can be used for a position sensitive measurement. The MagneTOF® allows for a time-of-flight measurement and the energy analyzer grids can be used to determine the energy. The segmented Faraday cup was not used in the commissioning.

The MCP used in the detector cross has a channel diameter of 6 μm and a bias angle of 12°. A monochrome camera (CS505MU - Kiralux 5 Megapixel Monochrome CMOS Camera) and a zoom lens (MVL7000) supplied by Thorlabs were used to image the phosphor screen. At the emission wavelength of phosphor P47 (400 nm), the quantum efficiency of the camera is $\sim 60\%$. In combination with the camera and lens, the smallest resolvable feature is 40 μm. The camera was mounted on a tripod in front of a viewing port, which allowed the beam shape to be captured.

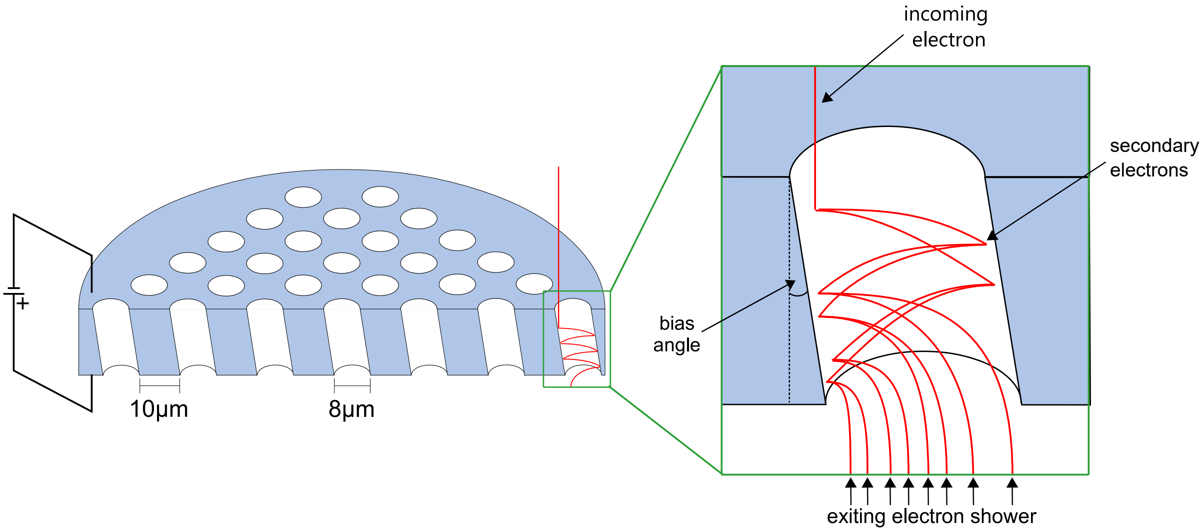

Figure 2.35.: Schematic view of a microchannel plate. An incoming electron (vertical red line) creates a cascade of secondary electrons (curved red lines). The angle at which the channels are tilted is called the bias angle. Figure adapted from [141] under CC 0 1.0.

A MagneTOF® detector by ETP ion detect® (<1.5 ns multiple ion pulse width) was used for two purposes: first, to determine the time of flight (ToF) of the antiprotons, and second, in combination with an "energy grid", to determine the kinetic energy distribution of the decelerated antiprotons. In a MagneTOF® detector, ions are accelerated towards an impact plate and the secondary electrons are guided to the dynodes with a magnetic field, to be multiplied (see Fig. 2.36).

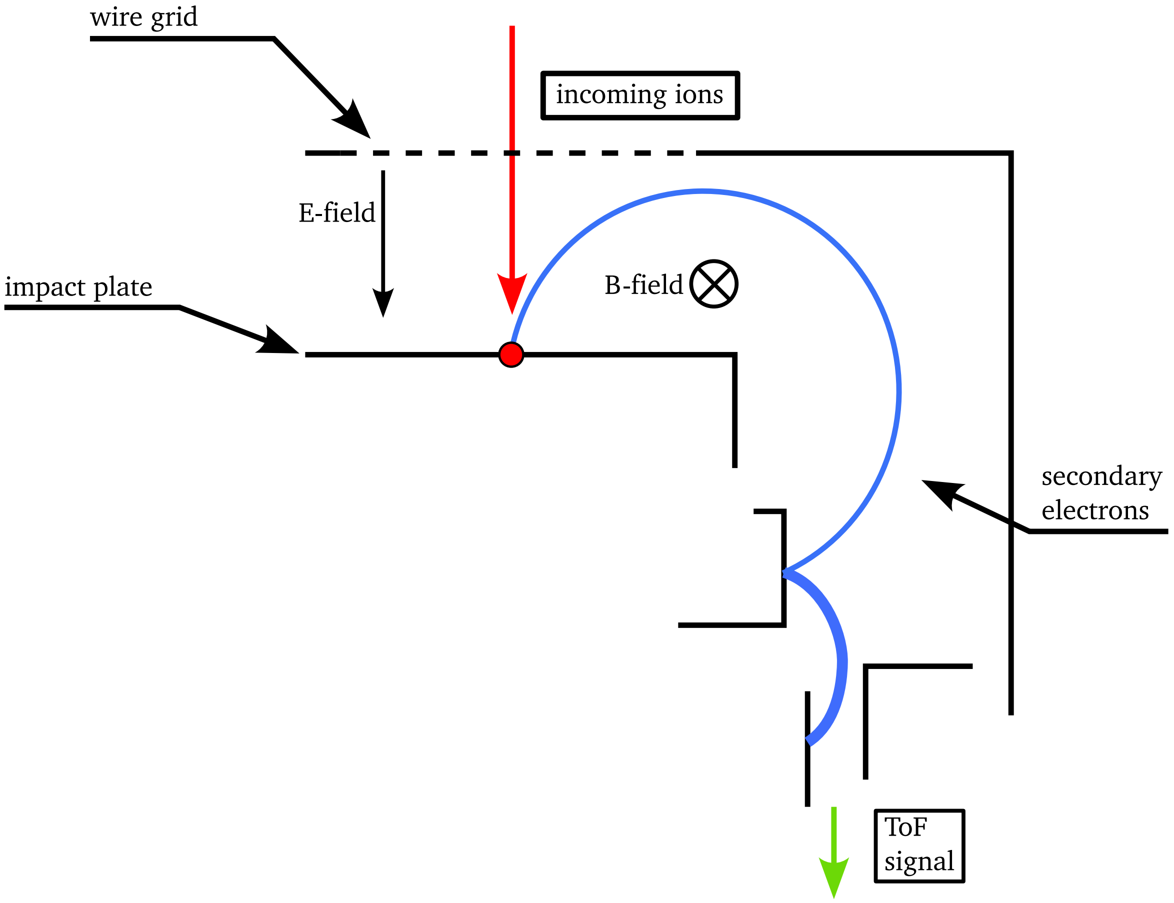

Figure 2.36.: Schematic view of a MagneTOF® detector. An incoming ion (vertical red line) creates secondary electrons (curved blue lines) on the impact plate. The magnetic field leads to isochronous transport of the electrons to the multiplier. Figure adapted from [142] under CC BY 4.0

The energy grid consists of a stack of three grids by ETP ion detect® with a diameter of 76.2 mm (see right panel of Fig. 2.34). The distance between the grids is 15 mm. The grid wires have a diameter of 0.018 mm, a center-to-center distance of 0.25 mm, and a transmission of 92% to 95%. The two outer grids were grounded, while a blocking voltage was applied to the middle one, with a ripple of less than 10 mV. The energy grids and the MagneTOF® detector can be moved out of the beam axis independently.

In addition to those detectors, the beam TV (BTV) further upstream in the beamline (see left panel of Fig. 2.34) was used for particle detection and intensity determination. The BTV uses a scintillating screen and a camera to determine the beam profile and position. The particles need enough energy to excite the scintillator, in our case phosphor. Because of the energy released in the annihilation, antiprotons are visible even at low energies, but H^- ions, used at ELENA as a proxy, are not. The BTV has a resolution of 0.0625 mm/pixel.

2.6.2. Pulsed Drift Tube Switching Delay

To successfully decelerate the antiprotons, the time at which the bunch is fully contained inside the pulsed drift tube (t_s) has to be determined. At t_s, the potential is changed. In practice, t_s is the length of time between an external trigger signal, heralding the arrival of antiprotons, and the time they are inside the drift tube. To determine the ideal value, t_s has to be scanned while observing the time of flight of the antiprotons. If t_s is too small, *i.e.*, the voltage is switched to early, the antiprotons see a grounded electrode and traverse the pulsed drift tube at full speed, arriving the earliest and with their initial energy. If t_s is too large, the antiprotons are decelerated while entering the pulsed drift tube and reaccelerated when leaving it, thus they arrive later than the ones never decelerated, but still with their initial energy. When switching at the correct time, the antiproton bunch is decelerated on entry but is not reaccelerated on exit. Thus, it arrives later than in the other cases, as they are slower, which can be seen in a simulation of the deceleration in the pulsed drift tube performed in SIMION® by A. Schmidt (see top panel of Fig. 2.37). Detailed information on the ion optics of the beamline can be found in Ref. [86].

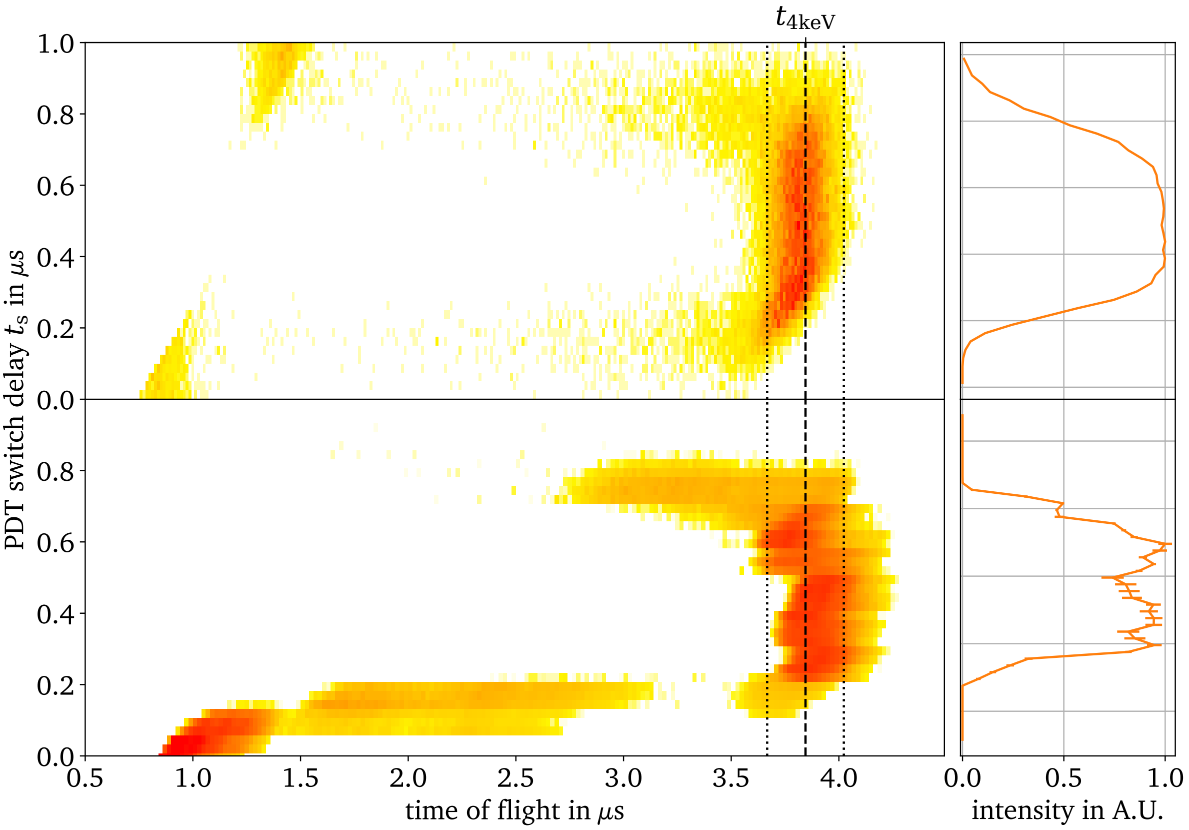

Figure 2.37.: Simulated (top) and measured (bottom) beam intensity when switching the pulsed drift tube from -96 kV to ground and varying the switch delay t_s. Yellow colors indicate lower and red higher intensity. In both cases, a successful deceleration to $4\,\mathrm{keV}$ corresponds to a time of flight $t_{4\mathrm{keV}}$ that is $2.9\,\mu\mathrm{s}$ longer than the undecelerated beam. On the right, the integrated intensity from $t_{4\mathrm{keV}} - 2\sigma$ to $t_{4\mathrm{keV}} + 2\sigma$ is shown, with $\sigma = 0.09\,\mu\mathrm{s}$, and t_s is chosen to maximize this intensity. The indicated uncertainty originates from the jitter of the arrival of antiprotons relative to the trigger, here $20\,\mathrm{ns}$. Figure adapted from [119] under CC BY 4.0.

The results from the measurement can be seen in the bottom panel of Fig. 2.37, they match the behavior expected from simulations. When t_s is too small, the antiprotons arrived early. When increasing t_s, the bunch diffuses, as it is partly in the fringe field of the electrode when the pulsed drift tube is switched. Afterward, in a window of about 300 ns, the antiprotons are uniformly decelerated. As t_s is further increased, the bunch diffuses again, because it is only partly inside the pulsed drift tube when switching.

The measurement shows a successful deceleration, and an estimation from the time of flight gives a deceleration to (4.0 ± 0.5) keV. A more precise measurement of the energy distribution was performed using the energy grids (see Sec. 2.6.4).

2.6.3. Transmission and Focusing

The intensity of the bunch after the pulsed drift tube (I), can be compared to the initial intensity of the bunch (I_0). The total transmission through the pulsed drift tube is thus defined by $T = I/I_0$. Upstream of the handover point, pick-ups in the ELENA transfer lines [143] determine the number of antiprotons in a bunch. Due to the small divergence of the beam at 100 keV, the transmission to the BTV is 100%. Besides showing the beam spot shape, the total intensity on the BTV is proportional to the number of incoming antiprotons, as can be seen in Fig. 2.38. The intensity on the BTV does not depend on the kinetic energy (at ~ 100 keV), as the energy released by the annihilation is much larger. This is evidenced by the fact that H^- ions at 100 keV do not produce a signal on the BTV.

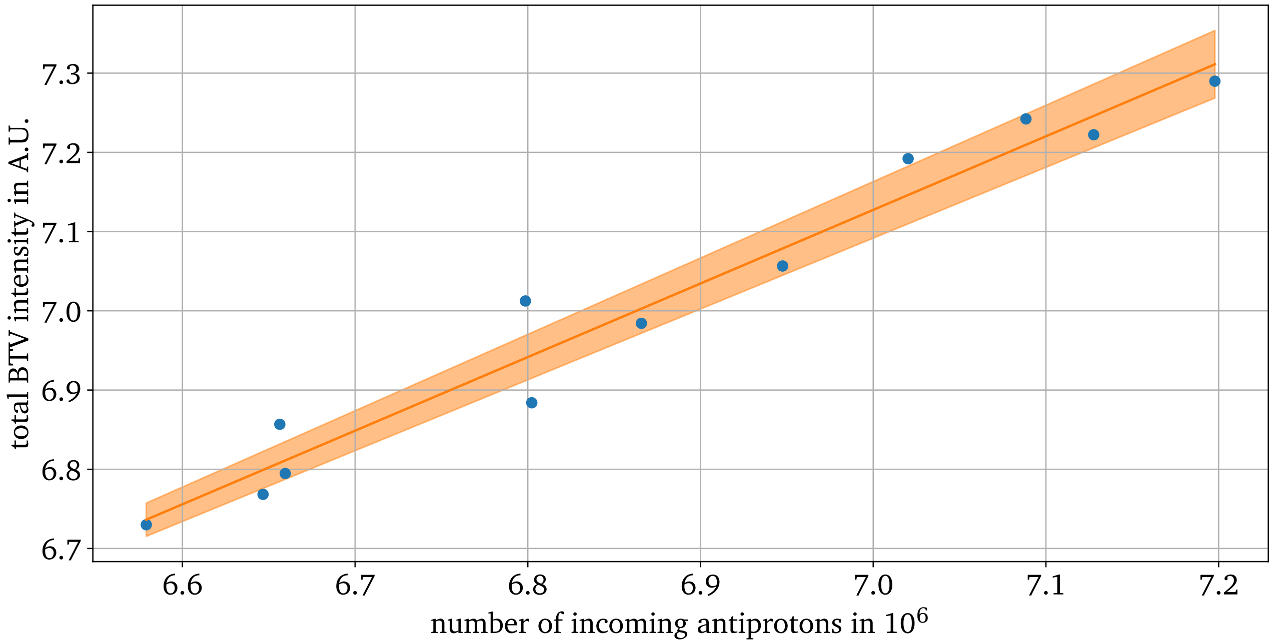

Figure 2.38.: The total intensity on the BTV is proportional to the number of antiprotons determined by the ELENA detectors. The transmission to the BTV is 100% at 100 keV. This allows to make a calibration to determine the transmission through the pulsed drift tube while decelerating.

Using the calibration in this plot, the intensity on the BTV $I_0(N_{\bar{\mathrm{p}},\mathrm{in}})$ expected for 100% transmission can be calculated. The intensity on the BTV I, along with the reconstructed intensity I_0 and the number of incoming antiprotons as determined by the pick-ups ($N_{\bar{\mathrm{p}},\mathrm{in}}$), is shown in Fig. 2.39. The transmission is then calculated using I_0.

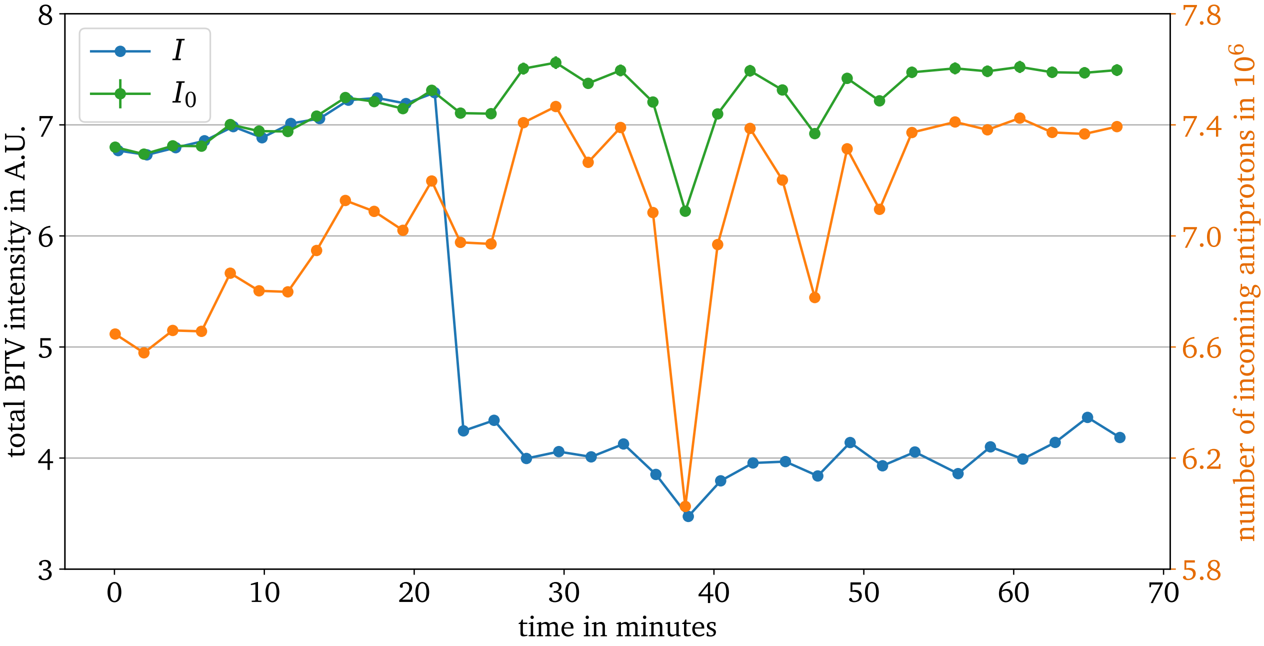

Figure 2.39.: The intensity on the BTV I (blue), along with the reconstructed intensity I_0 (green) and the number of incoming antiprotons as determined by the pick-ups $N_{\bar{\mathrm{p}},\mathrm{in}}$ (orange). The first 12 data points are used for the calibration ($E = 100\,\mathrm{keV}, T = 100\%$). The uncertainty stemming from the calibration is smaller than the markers.

During the experiment, the transmission of antiprotons decelerated to 4 keV reached $(55 \pm 3)\%$, while in simulations a transmission of 100% could be reached. The quoted uncertainty is purely statistical and the calibration uncertainty does not contribute significantly.

The voltage on the high-voltage einzel lens was limited to -85 kV, because the pulsed drift tube and the high-voltage einzel lens are misaligned. This is evidenced by the observation that increasing the voltage on the high-voltage einzel lens leads to a vertical shift of the beam. Were they perfectly aligned, the position of the beam spot on the BTV would stay the same. Shifts from voltages higher than -85 kV could not be compensated by the horizontal-vertical corrector units (ZQNA) upstream of the handover point (see Fig. 2.1). In simulations, this lower voltage leads to a drop in transmission from 100% to 95%. The effect of the high-voltage einzel lens was investigated with simulations and measurements, varying the applied voltage (see Fig. 2.40). In the simulation, the maximum transmission of 100% is reached at -89 kV. The measured transmission always falls a factor ~ 2 below the simulated one.

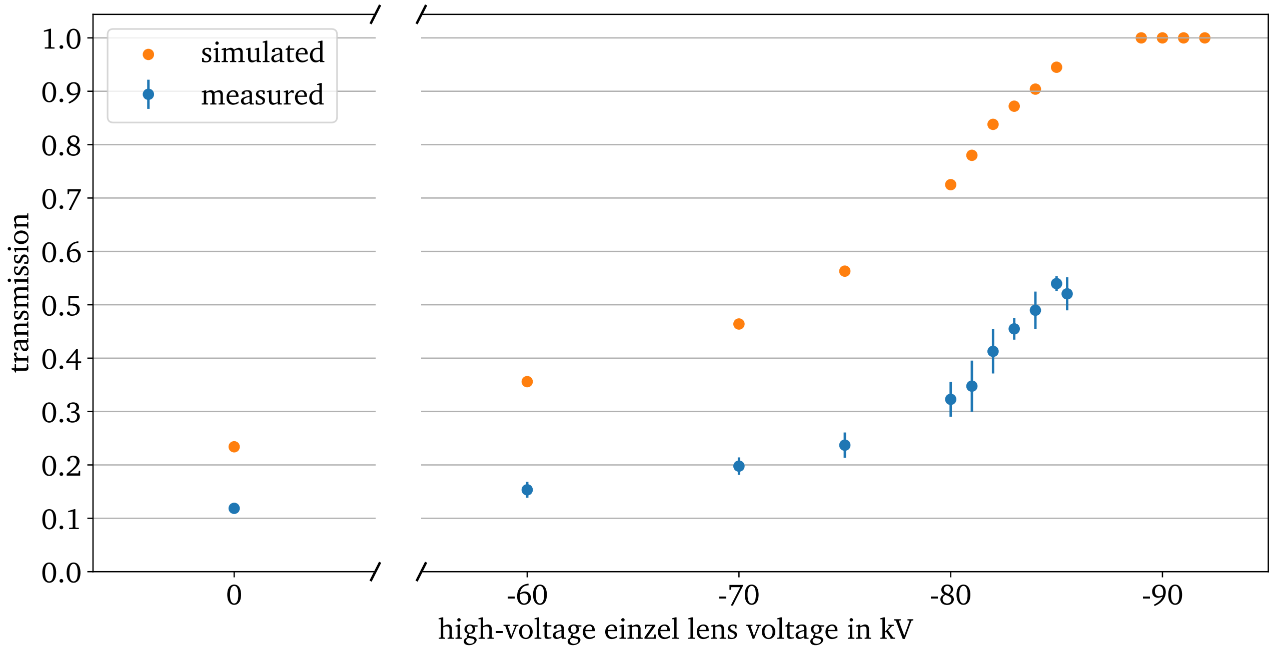

Figure 2.40.: The transmission of decelerated antiprotons to the BTV, depending on the high-voltage einzel lens voltage. The transmission rises to 100% at -89 kV in the simulation. The measured transmission also rises in the same manner but is always approximately half of the simulated transmission. Simulation data courtesy of A. Schmidt.

The origin of this loss is unknown. It might be from a misalignment of the ion optical elements, as the high-voltage einzel lens, drift tube and low-voltage einzel lens are not adjustable relative to each other, and also the two einzel lenses with steerers are fixed to each other and can only be aligned as a block. Furthermore, an optimization of the einzel lens voltages might bring improvement. In addition, the parameters assumed in the simulation for the incoming beam might also play a role.

Figure 2.41 shows the beam profile recorded by the BTV. The einzel lenses were used to focus the beam at the position of the BTV. Using a Gaussian fit, the following parameters can be obtained:

$$\begin{aligned}\sigma_{\text{horiz}} &= (3.0 \pm 0.1)\,\text{mm} \\ \sigma_{\text{vert}} &= (3.8 \pm 0.2)\,\text{mm}\end{aligned}$$

Overall, 64% of the antiprotons are within a circle of radius $r = 5.6\,\text{mm}$, the smallest aperture of the PUMA Penning trap. The focal point will have to be optimized at a later point for the injection into the PUMA trap.

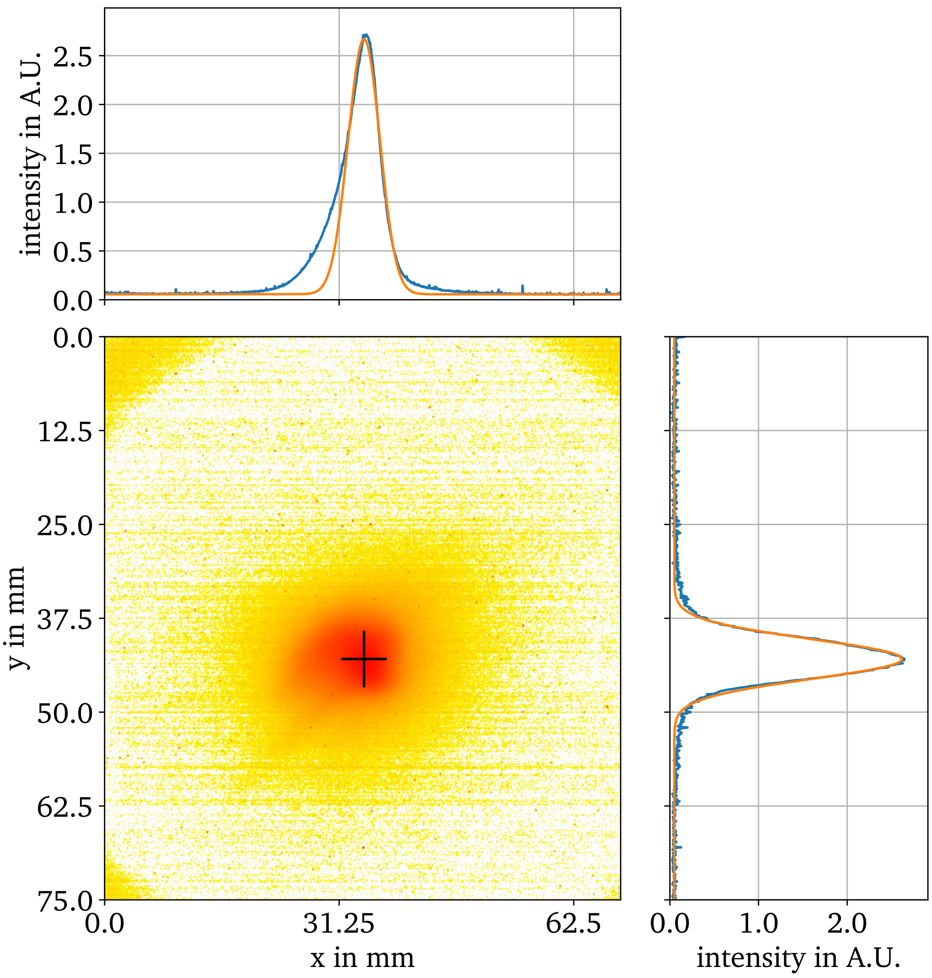

Figure 2.41.: Beam profile after optimizing the LV einzel lenses for deceleration to $4\,\mathrm{keV}$ and focus on the BTV. Fitting a Gaussian to the center peak yields $\sigma_{\mathrm{horiz}} = 3.0\,\mathrm{mm}$, $\sigma_{\mathrm{vert}} = 3.8\,\mathrm{mm}$. Yellow colors indicate lower and red higher intensity. The projected intensity is shown in blue and the Gaussian obtained from the fit in orange. Figure adapted from [119] under CC BY 4.0.

2.6.4. Energy Distribution

The standard deviation of the antiprotons' kinetic energy after deceleration to 4 keV at the position of the MagneTOF$^{®}$ detector was simulated to be 101 eV. The kinetic energy E of the antiprotons was determined by blocking the antiprotons with the energy grids, and measuring the transmission on the MagneTOF$^{®}$. The results can be seen in Fig. 2.42. In blue, the transmission onto the MagneTOF$^{®}$ is displayed in dependence of the kinetic energy of the antiprotons. Fitting the cumulative distribution function (CDF) of a normal distribution yields the mean energy $\mu = (3898 \pm 3)$ eV and energy spread $\sigma = (127 \pm 4)$ eV. The energy distribution calculated from the fit is shown in orange. This demonstrates the strength of the pulsed drift tube for the deceleration of antiprotons compared to foils, as the energy spread has only slightly increased compared to the initial distribution.

88% of decelerated antiprotons are within ± 200 eV of the central energy, which is the energy acceptance for successful trapping in the PUMA Penning trap, according to simulations.

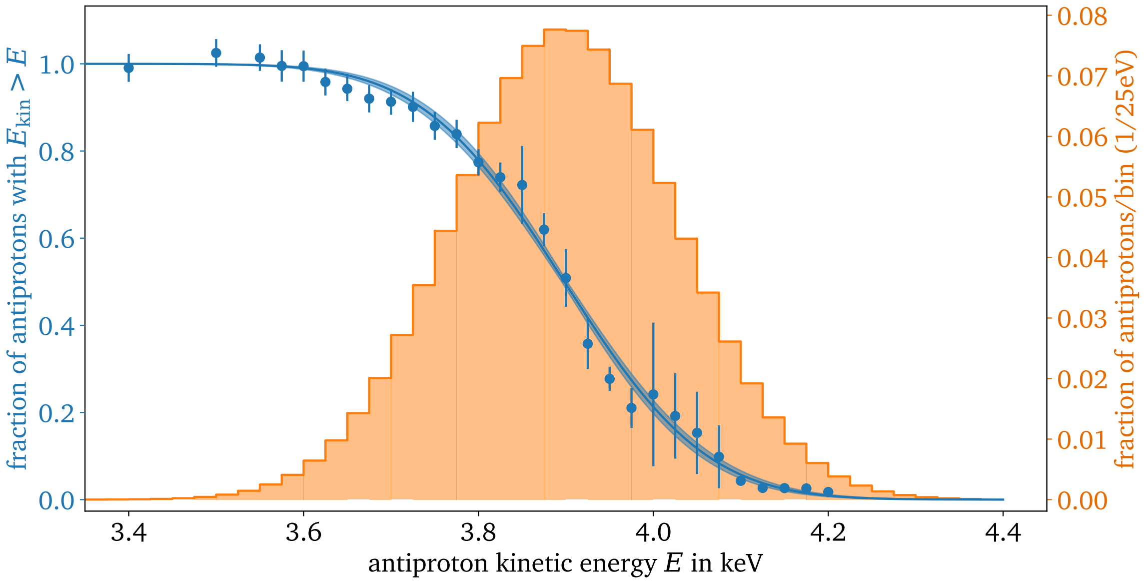

Figure 2.42.: The energy distribution of decelerated antiprotons. The data and fitted CDF of a normal distribution are shown in blue, and the probability density function corresponding to the fit in orange. The mean energy is $\mu = (3898 \pm 3)$ eV and the standard deviation $\sigma = (127 \pm 4)$ eV. 88% of decelerated antiprotons are within ± 200 eV of the mean energy, which is the estimated energy acceptance for trapping. Figure adapted from [119] under CC BY 4.0.

2.6.5. Bunch Length

The length of the antiproton bunch at 4 keV is relevant, because it determines the losses in the second stage of deceleration to a few 100 eV right in front of the trap. The simulation predicts an increase in length from 75 ns (1σ) to 89 ns (1σ) at the position of the MagneTOF®, with which 90% of the bunch can be trapped. A measurement of the bunch length of the decelerated antiprotons with the MagneTOF® yields a length (1σ) of (93 ± 3) ns, consistent with the simulation.

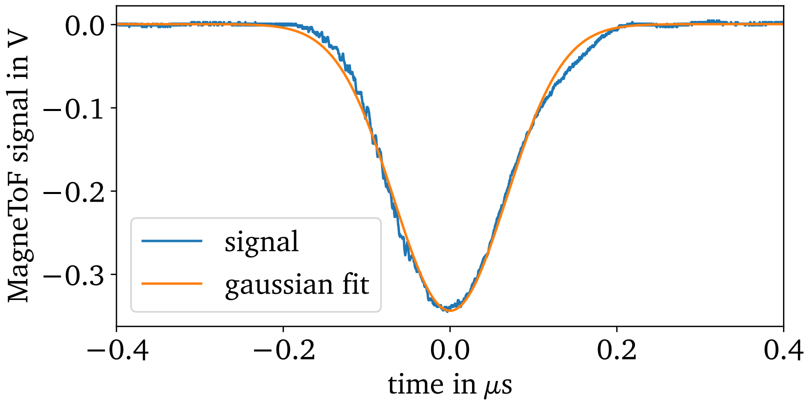

Figure 2.43.: The time-of-flight spectrum of one antiproton bunch after deceleration to 4 keV. The fit of a Gaussian to several bunches yields a length (1σ) of 93 ± 3 ns.

2.7. Summary

The PUMA antiproton beamline was designed, built and commissioned. The antiproton beamline is shown to be successful in decelerating antiprotons from 100 keV to (3898 ± 3) eV, the first step in trapping antiprotons for the PUMA experiment. With the implemented high-voltage ramping scheme (see Sec. 2.5.3), the pressure stays below $5 \cdot 10^{-10}$ mbar in section 1 for 75% of the cycle time, during operation of the pulsed drift tube. The commissioning was carried out without activating the NEG coating. It can be expected that the pressure will be even lower when the NEG coating of the beamline is activated for the use with the PUMA trap. According to vacuum simulations performed in MOLFLOW+, the achieved baseline pressure is sufficient to reach the required vacuum of $\sim 1 \cdot 10^{-11}$ mbar at the last gate valve to operate PUMA. The exact influence of the pressure spikes during the ramping and switching of high voltage on the pressure at the last gate valve, with the NEG coating activated and the NEG cross installed, remains to be investigated. A transmission of (55 ± 3)% for antiprotons decelerated to 4 keV was achieved. The beam can be focused to a spot with $\sigma_\text{horiz} = (3.0 \pm 0.1)$ mm and $\sigma_\text{vert} = (3.8 \pm 0.2)$ mm, demonstrating it can be focused into the PUMA Penning trap. The length of the 4 keV antiproton bunch, relevant for the second deceleration from 4 keV to 100 eV, is (93±3) ns. This matches the predicted bunch length from SIMION® simulations.

3. Cold Field Emission Electron Source

After the antiprotons are decelerated to 4 keV, they are injected into the PUMA Penning trap, where they are decelerated in another pulsed drift tube from 4 keV to a few 100 eV (the maximum electrostatic potential depth is 500 eV). This happens inside the magnetic field, to compensate the increase in divergence angle. As discussed in the previous chapter, deceleration with a pulsed drift tube conserves the width of the energy distribution which is around 100 eV at PUMA when operated at ELENA. The reduction of the mean and the variance of the kinetic energy are referred to as slowing and cooling in the context of this chapter. To achieve further reduction in the energy of captured antiprotons, several cooling techniques in Penning traps have been explored [144]. Among these, sympathetic electron cooling stands out as the fastest and most efficient method for slowing and cooling antiprotons across multiple orders of magnitude. Electron cooling is used in the Antiproton Decelerator and the ELENA ring. When storing a large number of antiprotons in a Penning trap their behavior can be described as a plasma. The maximum achievable density is given by the Brillouin limit [145]

$$n_\mathrm{B} = \frac{\epsilon_0 B^2}{2m} = 4.2 \cdot 10^{10}\,\mathrm{cm}^{-3} \text{ with } B = 4\,\mathrm{T}, m = m_{\bar{\mathrm{p}}} \tag{3.1}$$

for the PUMA Penning trap. Experimentally, only a few percent of this limit is reached routinely [146], translating to $n_{\bar{\mathrm{p}}} \sim 10^8\,\mathrm{cm}^{-3}$ for the PUMA Penning trap. Due to their charges, the antiprotons repel each other leading to an increasing size of the plasma. To compensate this, and allow long term storage, the plasma is usually compressed by applying a rotating electric field on a segmented electrode. This is called the *rotating wall technique* [147]. However, the compression leads to a heating of the plasma, that has to be countered by constant sympathetic cooling in PUMA. Inhomogeneities in the magnetic and electric field, as well as misalignment also lead to a heating of the plasma.

3.1. Cooling Antiprotons

3.1.1. Cyclotron Cooling

Charged particles emit electromagnetic radiation when accelerated and the particles in a Penning trap constantly experience acceleration due to the magnetic and electric fields. The combination of the two effects leads to a loss of energy in the form of cyclotron radiation for a particle of charge q and mass m in the magnetic field of the trap. The energy loss $\frac{\mathrm{d}E}{\mathrm{d}t}$ is given by the Larmor formula [148]

$$\frac{\mathrm{d}E}{\mathrm{d}t} = -\frac{q^2}{6\pi\epsilon_0 c^3} a^2, \tag{3.2}$$

where a is the acceleration. For a particle in harmonic motion, meaning the restoring force is oppositely proportional to the displacement, the mean rate of energy loss is given by

$$\left\langle \frac{\mathrm{d}E}{\mathrm{d}t} \right\rangle = -\gamma_r E, \tag{3.3}$$

which is solved by

$$E = E_0 \mathrm{e}^{-\gamma_r t}, \tag{3.4}$$

where the decay constant γ_r is given by

$$\gamma_r = \frac{q^2\omega^2}{6\pi\epsilon_0 mc^3} \tag{3.5}$$

if ω is the frequency of the harmonic motion.

For a cyclotron motion, γ_c is equal to $2\gamma_r$ [148, p. 198]. Substituting the cyclotron frequency $\omega = \omega_\mathrm{c} = qB/m$ one gets

$$\gamma_c = \frac{q^4B^2}{3\pi\epsilon_0 c^3 m^3}, \tag{3.6}$$

where B is the magnetic field. This gives a cooling constant $\tau_\mathrm{e} = \gamma_\mathrm{e}^{-1} = 0.2\,\mathrm{s}$ for electrons in a magnetic field of 4 T, the magnetic field in the PUMA trap. For antiprotons, the constant is approximately 8 billion times larger, because of the dependence of τ_r on m^3. Electrons cool down to the trap temperature of 4.2 K within a second. They will not cool below this temperature because the trap acts as an infinite reservoir of 4.2 K black body radiation. Therefore, thermal equilibrium is reached at 4.2 K.

3.1.2. Sympathetic Cooling

To cool the antiprotons, electrons can be used as a coolant. As electrons and antiprotons have the same charge they can be stored in the same potential well. The electrons and antiprotons exchange energy via Coulomb collisions and due to the unequal mass, kinetic energy is transferred to the electrons, thereby cooling the antiprotons. This is called *sympathetic electron cooling*. The equations governing the temperatures T of the electrons and antiprotons are given by [149]

$$\frac{\mathrm{d}T_\mathrm{e}}{\mathrm{d}t} = \frac{1}{\tau_{\bar{\mathrm{p}}}}\frac{N_{\bar{\mathrm{p}}}}{N_\mathrm{e}}(T_{\bar{\mathrm{p}}} - T_\mathrm{e}) - \frac{1}{\tau_\mathrm{e}}(T_\mathrm{e} - T_\mathrm{am}) \tag{3.7}$$

$$\frac{\mathrm{d}T_{\bar{\mathrm{p}}}}{\mathrm{d}t} = -\frac{1}{\tau_{\bar{\mathrm{p}}}}(T_{\bar{\mathrm{p}}} - T_\mathrm{e}) + \frac{\Delta T_\mathrm{heating}}{\Delta t} \tag{3.8}$$

where $N_{\bar{\mathrm{p}}}/N_\mathrm{e}$ is the ratio of the number of antiprotons to electrons, T_am is the ambient temperature of 4.2 K, $\Delta T_\mathrm{heating}$ is a constant external heating, for example caused by the rotating wall technique. τ are the cooling constants of electrons and antiprotons. $\tau_{\bar{\mathrm{p}}}$ is given by [150, 151]

$$\tau_{\bar{\mathrm{p}}} = \frac{3m_{\bar{\mathrm{p}}}m_\mathrm{e}c^3}{8\sqrt{2\pi}\,n_\mathrm{e}q^4\ln(\Lambda)} \cdot \left(\frac{\mathrm{k_B}T_\mathrm{e}}{m_\mathrm{e}c^2} + \frac{\mathrm{k_B}T_{\bar{\mathrm{p}}}}{m_{\bar{\mathrm{p}}}c^2}\right)^{3/2} \qquad \text{(cgs units)}. \tag{3.9}$$

Here q is equal to the elementary charge, and n_e is the electron number density. $\ln\Lambda$ is the so-called Coulomb logarithm and can be calculated as follows [144]

$$\ln(\Lambda) = \ln\left(\frac{4\cdot 10^3}{\sqrt{n_\mathrm{e}}}\sqrt{T_\mathrm{e}}\cdot\left(T_\mathrm{e} + \frac{T_{\bar{\mathrm{p}}}}{1836} + \frac{\sqrt{T_\mathrm{e}\cdot T_{\bar{\mathrm{p}}}}}{21}\right)\right) \tag{3.10}$$

with n_i in cm^{-3} and T_i in K. Figure 3.1 shows the evolution of the temperature for two different ratios $N_{\bar{\mathrm{p}}}/N_\mathrm{e}$. The temperature is obtained by the numerical solution of equations 3.7 and 3.8. The solid line represents $N_{\bar{\mathrm{p}}}/N_{\mathrm{e}} = 0.1$ and the dashed $N_{\bar{\mathrm{p}}}/N_{\mathrm{e}} = 1$. The electron density considered for both cases is $n_{\mathrm{e}} = 10^8\,\mathrm{cm}^{-3}$ and the initial temperatures are

$$T_{\mathrm{e},0} = 4.2\,\mathrm{K} \tag{3.11}$$

$$T_{\bar{\mathrm{p}},0} = 1160450\,\mathrm{K}\ (\mathrm{k_B} T_{\bar{\mathrm{p}},0} = 100\,\mathrm{eV}) \tag{3.12}$$

$$T_{\mathrm{am}} = 4.2\,\mathrm{K} \tag{3.13}$$

$$\frac{\Delta T_{\mathrm{heating}}}{\Delta t} = 46418\,\mathrm{Ks}^{-1}\ (4\,\mathrm{eVs}^{-1}). \tag{3.14}$$

The value for $\Delta T_{\mathrm{heating}}$ is taken from [147] for a strong rotating wall compression.

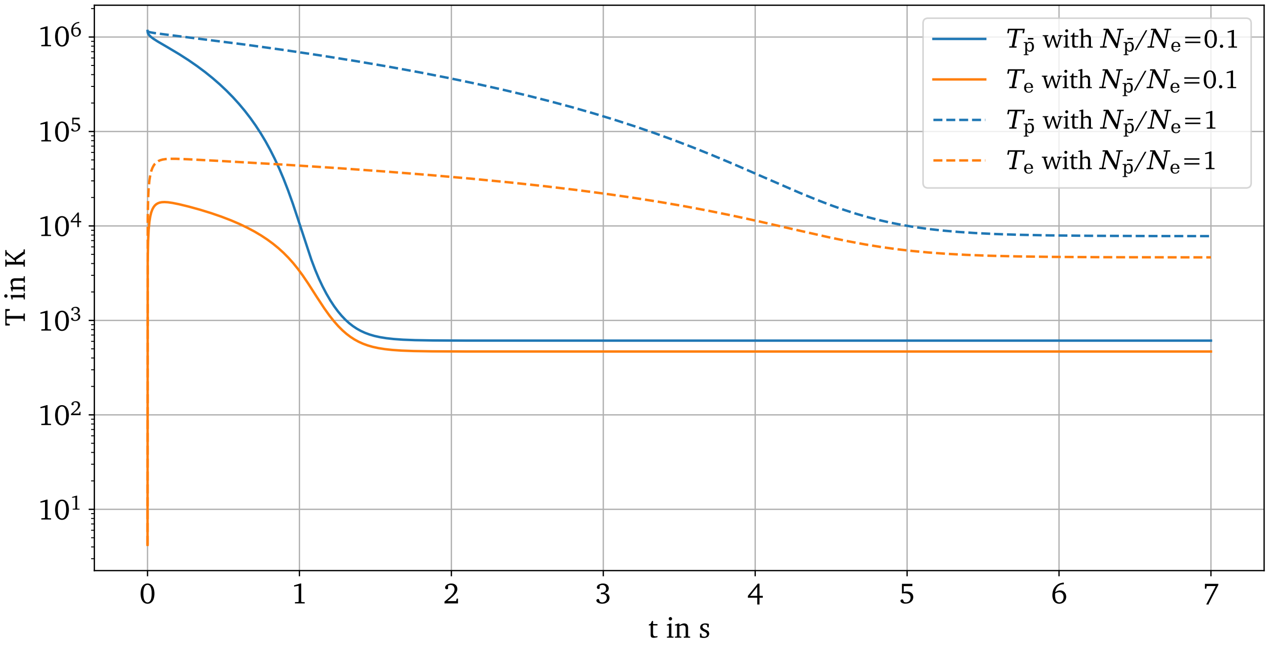

Figure 3.1.: The temperature of antiprotons and electrons with $N_{\bar{\mathrm{p}}}/N_{\mathrm{e}}$ equal to 0.1 (solid) and 1 (dashed) over time. The electron density is constant at $n_{\mathrm{e}} = 10^8\,\mathrm{cm}^{-3}$.

Neither the electron temperature nor the antiproton temperature go down to the ambient temperature. This is due to the constant heating term in Eq. 3.8, that was added to simulate the heating effect of the rotating wall. With fewer antiprotons, the ensemble can be cooled to lower temperatures if the electron density is kept constant. For this calculation full overlap of the electrons and antiprotons was assumed. The reported cooling times lie in the range of tens of seconds [152, 153].

Figure 3.2 shows the temperature evolution for two different electron densities. For a higher electron density, the antiprotons are cooled more quickly and to a lower temperature. Because the electron and the antiproton density are directly connected to the ratio of the number of electrons to antiprotons, at a fixed $N_{\bar{\mathrm{p}}}/N_{\mathrm{e}}$, a higher electron density also means a higher antiproton density. Comparing the electron equilibrium temperatures

$$T_{\mathrm{e,eq}} := \lim_{t\to\infty} T_{\mathrm{e}}(t) \tag{3.15}$$

for $n_{\mathrm{e}} = 10^8\,\mathrm{cm}^{-3}$ and $n_{\mathrm{e}} = 10^7\,\mathrm{cm}^{-3}$ shows, that the change in the electron equilibrium temperature $T_{\mathrm{e,eq}}$ is negligible (see Fig. 3.2), and that the cooling time increases by a factor of less than three.

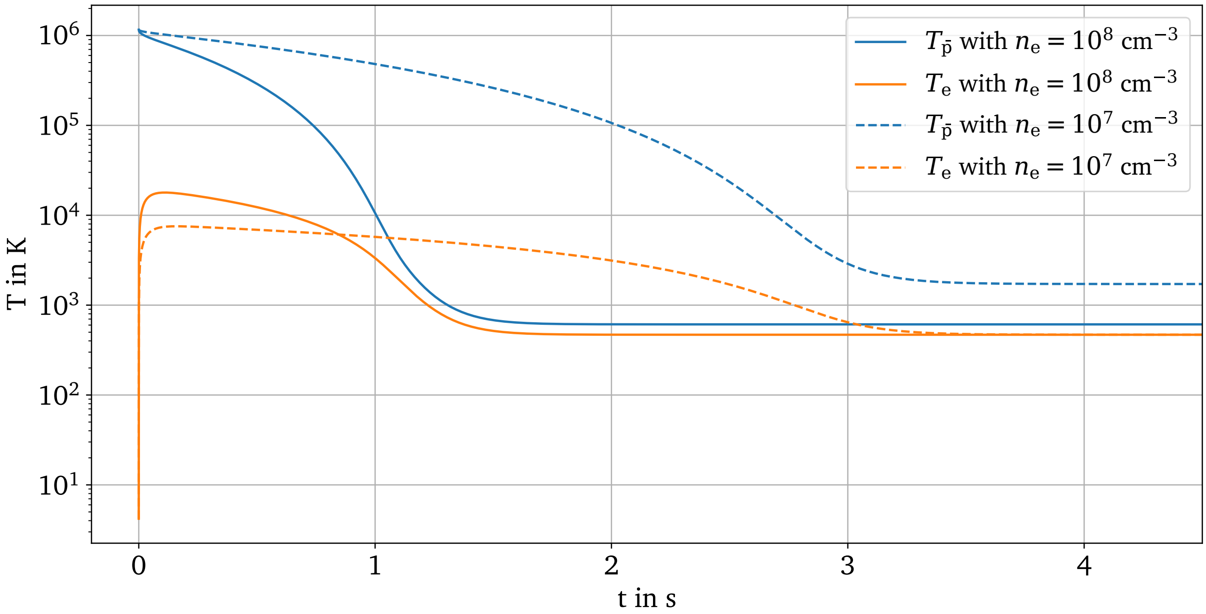

Figure 3.2.: The temperature of antiprotons and electrons over time with n_e equal to 10^8 (solid) and $10^7\,\mathrm{cm}^{-3}$ (dashed). The antiproton to electron ratio is constant at $N_{\bar{\mathrm{p}}}/N_\mathrm{e} = 0.1$.

In a scenario where bunches of antiprotons are stacked in the storage trap, Eq. 3.7 and 3.8 can be expanded to include already cooled and still hot antiprotons

$$\frac{\mathrm{d}T_\mathrm{e}}{\mathrm{d}t} = +\frac{1}{\tau_{\mathrm{cool}\,\bar{\mathrm{p}},\mathrm{e}}}\frac{N_{\mathrm{cool}\,\bar{\mathrm{p}}}}{N_\mathrm{e}}(T_{\mathrm{cool}\,\bar{\mathrm{p}}} - T_\mathrm{e}) + \frac{1}{\tau_{\mathrm{hot}\,\bar{\mathrm{p}},\mathrm{e}}}\frac{N_{\mathrm{hot}\,\bar{\mathrm{p}}}}{N_\mathrm{e}}(T_{\mathrm{hot}\,\bar{\mathrm{p}}} - T_\mathrm{e}) - \frac{1}{\tau_\mathrm{e}}(T_\mathrm{e} - T_\mathrm{am}) \tag{3.16}$$

$$\frac{\mathrm{d}T_{\mathrm{cool}\,\bar{\mathrm{p}}}}{\mathrm{d}t} = +\frac{1}{\tau_{\mathrm{hot}\,\bar{\mathrm{p}},\mathrm{cool}\,\bar{\mathrm{p}}}}\frac{N_{\mathrm{hot}\,\bar{\mathrm{p}}}}{N_{\mathrm{cool}\,\bar{\mathrm{p}}}}(T_{\mathrm{hot}\,\bar{\mathrm{p}}} - T_{\mathrm{cool}\,\bar{\mathrm{p}}}) - \frac{1}{\tau_{\mathrm{cool}\,\bar{\mathrm{p}},\mathrm{e}}}(T_{\mathrm{cool}\,\bar{\mathrm{p}}} - T_\mathrm{e}) + \frac{\Delta T_\mathrm{heating}}{\Delta t} \tag{3.17}$$

$$\frac{\mathrm{d}T_{\mathrm{hot}\,\bar{\mathrm{p}}}}{\mathrm{d}t} = -\frac{1}{\tau_{\mathrm{hot}\,\bar{\mathrm{p}},\mathrm{cool}\,\bar{\mathrm{p}}}}(T_{\mathrm{hot}\,\bar{\mathrm{p}}} - T_{\mathrm{cool}\,\bar{\mathrm{p}}}) - \frac{1}{\tau_{\mathrm{hot}\,\bar{\mathrm{p}},\mathrm{e}}}(T_{\mathrm{hot}\,\bar{\mathrm{p}}} - T_\mathrm{e}) + \frac{\Delta T_\mathrm{heating}}{\Delta t}. \tag{3.18}$$

The cooling constant $\tau_{\mathrm{hot}\,\bar{\mathrm{p}},\mathrm{cool}\,\bar{\mathrm{p}}}$ can be found with Eq. 3.9 by substituting $\bar{\mathrm{p}} \to \mathrm{hot}\,\bar{\mathrm{p}}$ and $\mathrm{e} \to \mathrm{cool}\,\bar{\mathrm{p}}$. Because the mass of the antiproton is much higher than the electron's, $\tau_{\mathrm{hot}\,\bar{\mathrm{p}},\mathrm{cool}\,\bar{\mathrm{p}}}$ is large and these terms can be ignored, only the electrons contribute to the cooling. As antiproton bunches only arrive every 120 s from ELENA, the trapped ones are already in equilibrium with the electrons when the new bunch arrives, *i.e.*, $\frac{\mathrm{d}T_{\mathrm{cool}\,\bar{\mathrm{p}}}}{\mathrm{d}t} = 0$. The temperature curve does not depend strongly on the initial electron temperature because τ_e is small. Therefore Eq. 3.16, 3.17 and 3.18 can be simplified to

$$\frac{\mathrm{d}T_\mathrm{e}}{\mathrm{d}t} = +\frac{N_{\mathrm{cool}\,\bar{\mathrm{p}}}}{N_\mathrm{e}}\frac{\Delta T_\mathrm{heating}}{\Delta t} + \frac{1}{\tau_{\mathrm{hot}\,\bar{\mathrm{p}},\mathrm{e}}}\frac{N_{\mathrm{hot}\,\bar{\mathrm{p}}}}{N_\mathrm{e}}(T_{\mathrm{hot}\,\bar{\mathrm{p}}} - T_\mathrm{e}) - \frac{1}{\tau_\mathrm{e}}(T_\mathrm{e} - T_\mathrm{am}) \tag{3.19}$$

$$\frac{\mathrm{d}T_{\mathrm{hot}\,\bar{\mathrm{p}}}}{\mathrm{d}t} = -\frac{1}{\tau_{\mathrm{hot}\,\bar{\mathrm{p}},\mathrm{e}}}(T_{\mathrm{hot}\,\bar{\mathrm{p}}} - T_\mathrm{e}) + \frac{\Delta T_\mathrm{heating}}{\Delta t}. \tag{3.20}$$

For $N_{\mathrm{cool}\,\bar{\mathrm{p}}}/N_\mathrm{e} = 0$ Eq. 3.19 equals Eq. 3.7. Stacking bunches of antiprotons $(N_{\mathrm{cool}\,\bar{\mathrm{p}}}/N_\mathrm{e} = 0.9, N_{\mathrm{hot}\,\bar{\mathrm{p}}}/N_\mathrm{e} = 0.1)$ instead of adding the same amount at once $(N_{\mathrm{cool}\,\bar{\mathrm{p}}}/N_\mathrm{e} = 0, N_{\mathrm{hot}\,\bar{\mathrm{p}}}/N_\mathrm{e} = 1)$ gives a cooling time that is roughly three times faster, assuming $n_\mathrm{e} = 10^8\,\mathrm{cm}^{-3}$ (see Fig. 3.3). The equilibrium temperature only depends on the ration of antiprotons to electrons $N_{\bar{\mathrm{p}}}/N_\mathrm{e}$ with $N_{\bar{\mathrm{p}}} = N_{\mathrm{cool}\,\bar{\mathrm{p}}} + N_{\mathrm{hot}\,\bar{\mathrm{p}}}$.

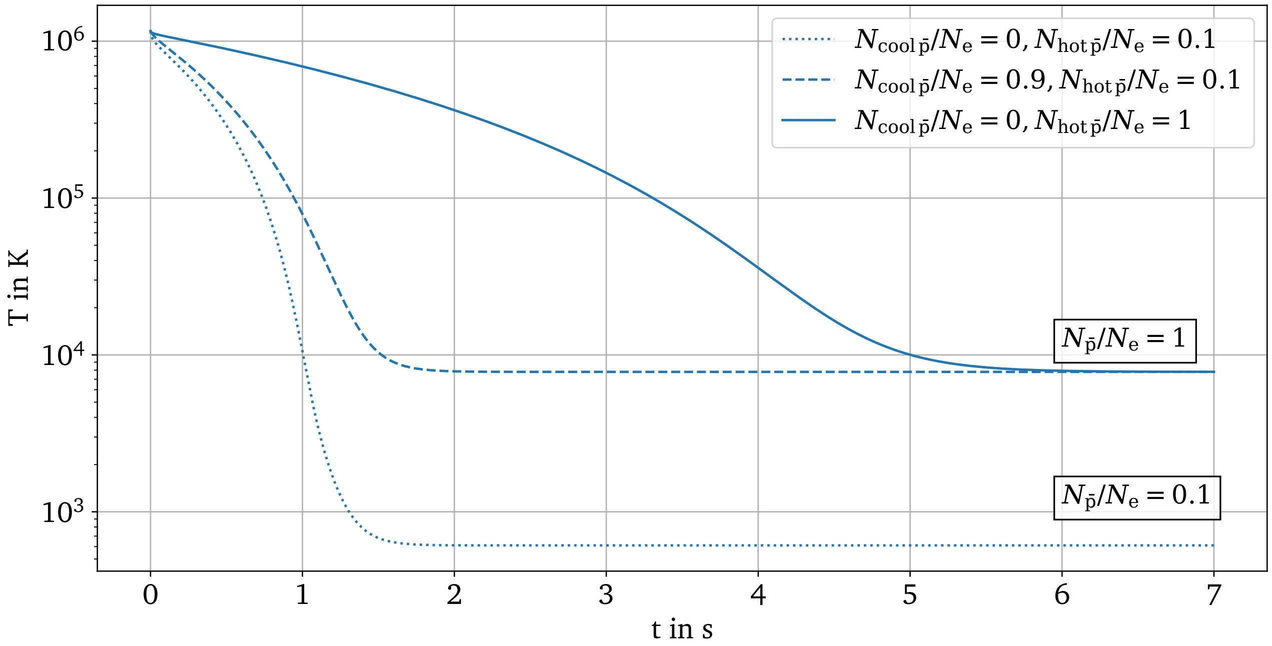

Figure 3.3.: Comparison between the temperature of a first bunch $(N_{\mathrm{cool}\,\bar{p}}/N_e = 0, N_{\mathrm{hot}\,\bar{p}}/N_e = 0.1)$, a later bunch $(N_{\mathrm{cool}\,\bar{p}}/N_e = 0.9, N_{\mathrm{hot}\,\bar{p}}/N_e = 0.1)$ and cooling the same number of antiprotons at once $(N_{\mathrm{cool}\,\bar{p}}/N_e = 0, N_{\mathrm{hot}\,\bar{p}}/N_e = 1)$. $N_{\bar{p}} = N_{\mathrm{cool}\,\bar{p}} + N_{\mathrm{hot}\,\bar{p}}$.

3.2. Field Emission

The mechanism chosen to produce the electrons is cold field emission (CFE). A design using this technique was first proposed by *Crewe et al.* in 1968 [154]. In contrast to many conventional electron sources that produce electrons via a hot filament, a field emission electron source does not introduce heat into the environment. This is important as the PUMA setup must be kept at 4 K for cryosorption to achieve the pressure for long-term antiproton storage.

The power that can be dissipated by a cold field emission process is small due to the low currents involved

$$P_{\mathrm{CFE}} = RI^2 = \rho \cdot l/A \cdot I^2 \approx 5 \cdot 10^{-12}\,\mathrm{W} \tag{3.21}$$

with the electrical resistivity of tungsten $\rho = 50\,\mathrm{n\Omega\,m}$, a current of $A = 1\,\mu\mathrm{A}$ and the thinnest part of the emitter approximated with $l = 1000\,\mathrm{nm}$ and $A = (100\,\mathrm{nm})^2$. Another common emitter, called Shottky type emitter, also uses field emission but enhances it by heating the emitter to a temperature of $T \approx 1500\,\mathrm{K}$. The power radiating from this emitter is much higher

$$P_{\mathrm{Shottky}} = \sigma T^4 A_{\mathrm{surface}} \approx 0.3\,\mathrm{W} \tag{3.22}$$

with the Stefan–Boltzmann constant σ and $A_{\mathrm{surface}} = (1\,\mathrm{mm})^2$. This motivates the need for a cold field emission source.

To extract electrons from the material in an electron source with a hot filament, the electrons are given energy greater than the work function ϕ via thermal energy. For field emission, a voltage is applied between the end of a metal wire and an extraction electrode, so that the potential outside the metal is lowered. This makes it possible for the electrons to tunnel out of the material (see Fig. 3.4).

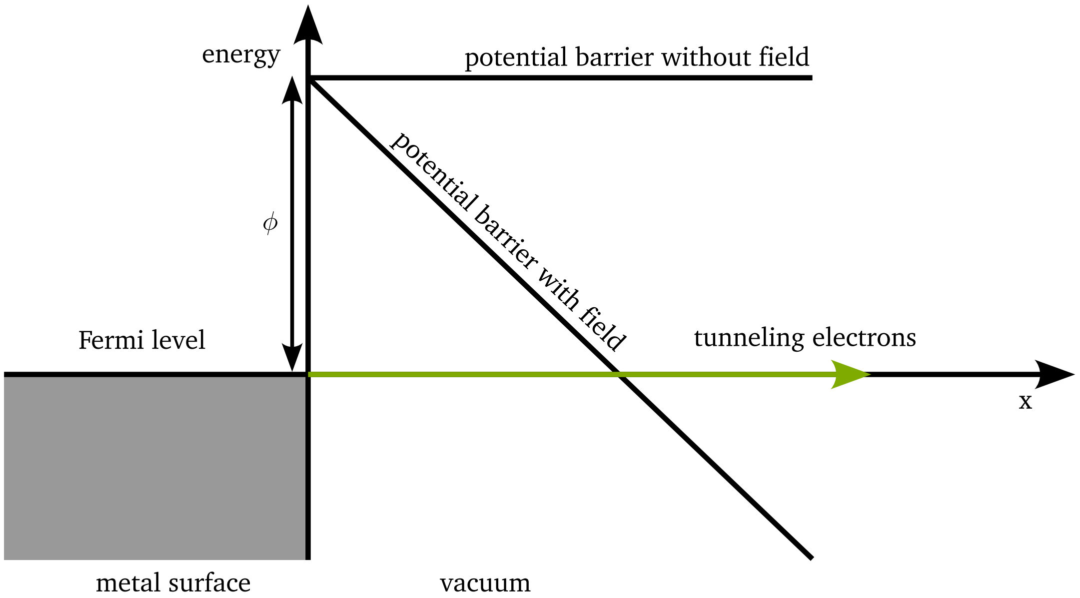

Figure 3.4.: Schematic depiction of the potential barrier on a metal surface with and without an external field. With an external field, the electrons are able to tunnel out of the metal.

The effective potential Φ_{eff} an electron has to overcome can, in a simple picture, be described as

$$\Phi_{\text{eff}} = \phi - E \cdot x, \tag{3.23}$$

where x is the distance from the surface and E the electric field strength. This means, with a higher electric field, the electrons can tunnel out more easily. If we describe the tip of the wire as a sphere of radius R on a infinitesimally thin wire, the electric field and the applied voltage U are related as follows

$$E = \frac{U}{x + R}, \tag{3.24}$$

at a distance x from the surface of the sphere. Combining equations 3.24 and 3.23, we get an effective potential that depends on the radius of the tip as

$$\Phi_{\text{eff}} = \phi - \frac{U}{x + R} \cdot x, \tag{3.25}$$

hence for a smaller R, Φ_{eff} drops more steeply and the electrons can tunnel out more easily for a given voltage applied. Therefore, a tip with smaller R yields a larger electron current. Such a wire is called a *field emission point*. The Fowler-Nordheim theory [155] describes the emission of electrons from a field emission point. It gives the relation between the electric field and the extracted current.

$$\begin{aligned} J &= a\phi^{-1}E^2 \exp\left(-b\phi^{3/2}/E\right) && \text{in A/nm}^2 \\ a &= 1.541434 \cdot 10^{-6} && \text{in A eV V}^{-2} \\ b &= 6.830890 && \text{in eV}^{-3/2}\text{ V nm}^{-1}. \end{aligned} \tag{3.26}$$

And because $I \propto J$ and $E \propto U$

$$I = AU^2 \exp\left(B/U\right), \tag{3.27}$$

with A and B determined by the exact shape of the tip and the electric field.

Because of the assumptions about the shape of the tip made by the Fowler-Nordheim theory, it is not possible to predict the current from an experimentally measured tip radius [156]. Empirically, it is found that a tip radius of below 200 nm is needed to make a tip fire with less than 5 kV applied [156]. The fabrication of field emission points is detailed in section 3.3.

3.3. Tungsten Wire Tip Production

3.3.1. Electrochemical Etching

Field emission points are made from tungsten because it has a high melting point and high durability. One established fabrication method is electrochemical etching. Here, the tungsten wire acts as an anode and is submerged in a basic solution. When a current is applied (see Fig. 3.5a), the following electrochemical reactions at the tungsten anode and the cathode take place [157]

$$\text{cathode} \quad 6H_2O + 6e^- \rightarrow 3H_2(g) + 6OH^- \tag{3.28}$$

$$\text{anode} \quad W(s) + 8OH^- \rightarrow WO_4^{2-} + 4H_2O + 6e^- \tag{3.29}$$

$$\text{net reaction} \quad W(s) + 2OH^- + 2H_2O \rightarrow WO_4^{2-} + 3H_2(g). \tag{3.30}$$

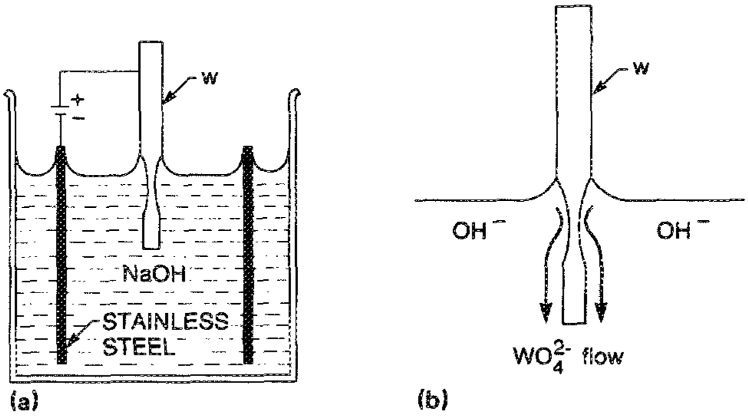

Figure 3.5.: Illustration of the "drop-off method". Due to capillary forces, a meniscus forms and the metal is etched more at the NaOH-air boundary. The downwards flowing WO_4^{2-} also protects the metal. Reprinted with permission from [157]. Copyright 1990, American Vacuum Society.

Because of the capillary forces, a meniscus is formed at the solution-air boundary. The etching process is slower at the top of the meniscus, because of a OH^--concentration gradient stemming from the diffusion of OH^- ions to the tip [158]. The WO_4^{2-} flows to the bottom of the tip and protects it from etching (see Fig. 3.5b). When the weight of the lower part cannot be supported anymore it drops off. The etching process at the lower part stops immediately as it is disconnected from the circuit. The method for the fabrication of field emission points presented in the next section (Sec. 3.3.2) utilizes this feature.

3.3.2. Fabrication of Field Emission Points

For the fabrication of field emission points, a modified version of the setup proposed by *Redshaw et al.* [156] (see Fig. 3.6) was used in the scope of my Master thesis [159]. In this setup, the tungsten wire is threaded through a hole in the copper cathode. Because of the capillary force, the NaOH solution forms a layer and the wire only etches at the part submerged in the solution. The lower part is disconnected from the circuit as soon as it drops, so the tip is not dulled by continued etching. Shaving foam is used to catch the tip. The copper cathode is 2 mm thick, with a 1.5 mm hole. A high purity tungsten rod (3N8 high purity tungsten wire from ESPI Metals) 0.25 mm thick was used as raw material. The rod is preferred over a wire from a spool, because the bent shape leads to irregular etching. The molarity of the NaOH solution was 1.5 mol/L, as in [156]. The etching current was set to 150 mA and maintained by the constant current mode on the power source.

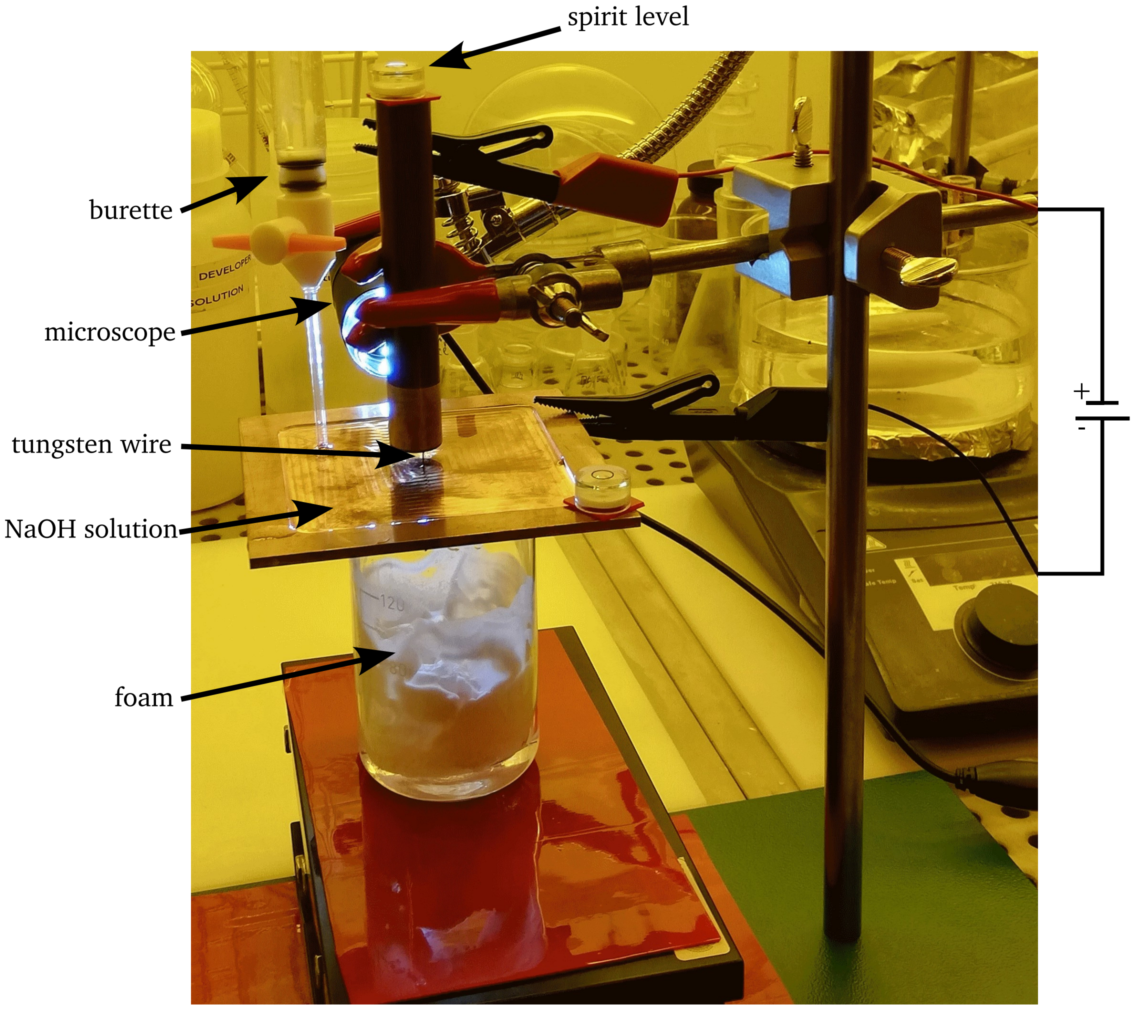

Figure 3.6.: Setup for the fabrication of field emission points adapted from [156].

It is important that the wire does not touch the copper plate, as this would short the circuit. After this, the NaOH solution is put on the cathode, replenished by more solution dropping from a burette. Enough NaOH must be supplied to maintain a constant current. Also, an insufficient supply causes hydrogen bubbles to form around the wire, disturbing the meniscus. A drop rate of 1 - 2 ml/min were the ideal balance between enough supply and minimal disturbance of the meniscus for this setup. The voltage needed to keep the current constant at 150 mA lies around 2 - 5 V, but rises more quickly toward the end of the etching. After 1.5 minutes, the tungsten is etched all the way through and the lower part drops. The tungsten rod is etched along the total thickness of the plate, plus the meniscus at the top and the meniscus at the bottom of the copper cathode (see Fig. 3.7). The etching is fastest at the lower meniscus, leading to the shape indicated in Fig. 3.7. 11 times out of 12 the tungsten dropped at the lower meniscus, only once at the upper one. This causes the nicely shaped part to be immediately disconnected from the etching current and preserves the sharpness of the tip. The tip is then rinsed with isopropanol, then acetone, then isopropanol again to remove the NaOH solution, shaving foam and other possible contaminants from the surface of the tungsten rod. Figure 3.8 shows a scanning electron microscope image of one field emission point at different magnifications. From the image, the tip radius can be estimated as $R \sim 130\,\mathrm{nm}$.

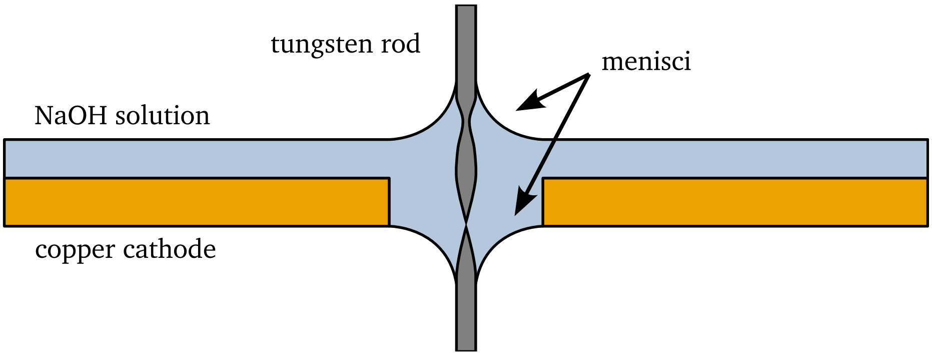

Figure 3.7.: A schematic cross section of the etching setup. Two menisci from at the tungsten rod and lead to an etching in two places.

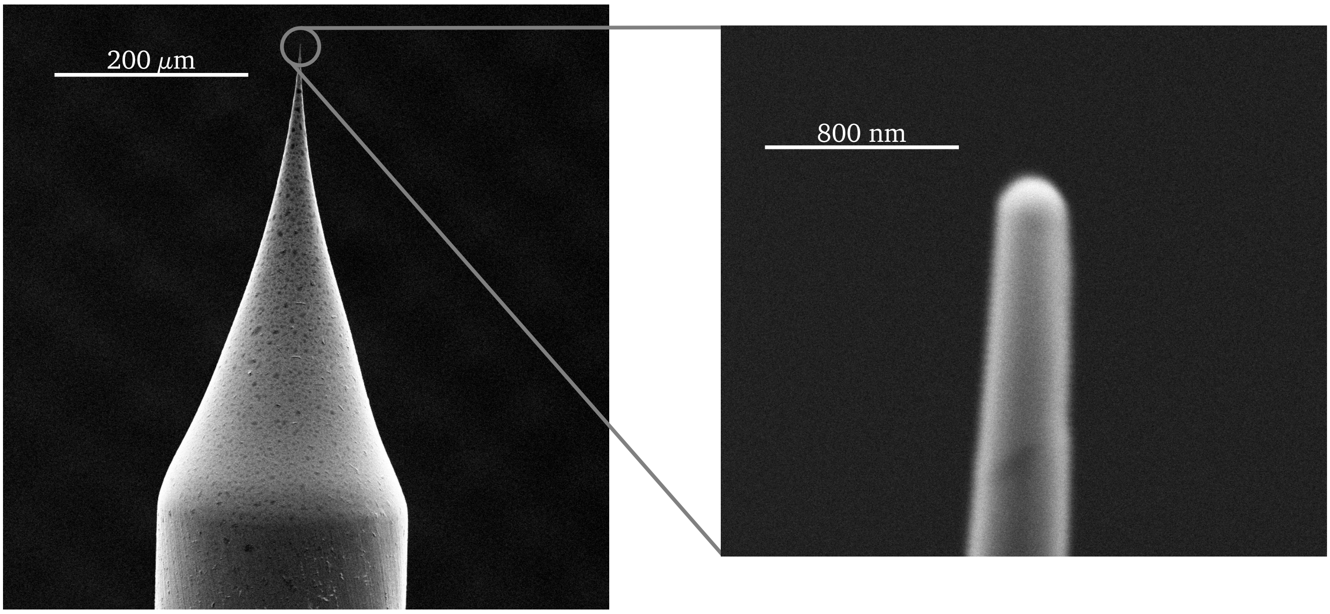

Figure 3.8.: Scanning electron microscope image of a field emission point at different magnifications. The radius at the tip is roughly 130 nm.

3.4. Electron Source Design

The electron source is composed of multiple anodes separated by insulators. A schematic drawing of the source is shown in the left panel of Fig. 3.9, and a picture of the assembled electron source in the right panel. The field emission point is mounted in such a way, that it is only a few 100 µm from the plane of the extraction electrode. To extract electrons from the field emission point, a high electric field is applied. This is achieved by setting the extractor to a potential of up to $+1$ kV. The casing is grounded so that after exiting the source, the electrons are at the same potential as the trap. To make it possible for the electrons to overcome the grounded aperture, the base is set to a small negative (~ -50 V) voltage. This voltage dictates the energy of the electrons after exiting the source. The compact design with an outer diameter of only 30 mm is necessary, because the electron source must fit into the PUMA cryostat at the downstream end of the Penning trap.

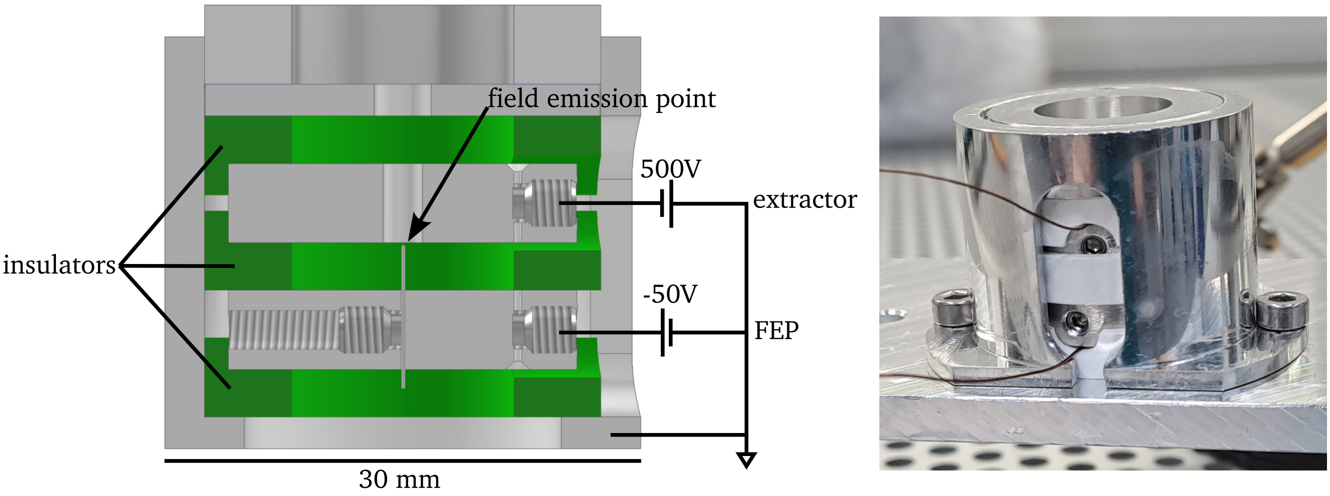

Figure 3.9.: Left: a schematic view of the electron source with the electrical layout. Right: the assembled electron source.

The electrons are emitted perpendicular to the surface (along the electric field lines), and therefore only a small fraction is emitted towards the opening of the electron source (see left panel of Fig. 3.10). The magnetic field used for the Penning trap helps in guiding the electrons through the exit aperture (see right panel of Fig. 3.10).

The simulated transmission with respect to the magnetic field is shown in Fig. 3.11. A magnetic field of $B = 0.34$ T is sufficient in this configuration to extract all electrons.

For redundancy, two electron sources are placed downstream of the PUMA storage trap. They are mounted 11 and 15 cm downstream and 11 mm off-center of the storage trap (see Fig. 3.12). The off-center injection of the electrons give them an initial cyclotron radius, easing plasma manipulation. Due to the increasing magnetic field strength towards the center of the trap (axially), the electrons are guided from 11 mm from the trap center (radially) to 6.6 mm.

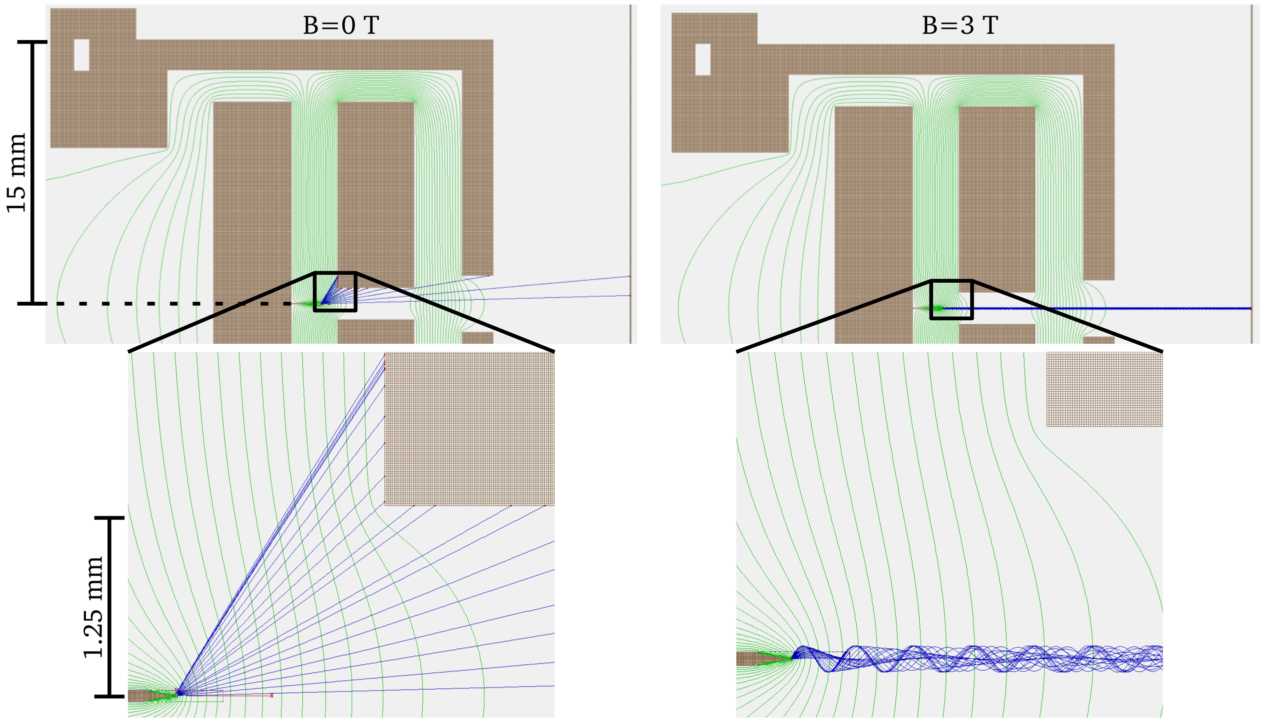

Figure 3.10.: A simulation of the current emitted from the electron source performed in SIMION®. Electrodes are shown in brown, equipotential lines in green and the electron trajectories in blue. Left: many electrons hit the extraction electrode instead of exiting though the aperture. Right: with a magnetic field parallel to the beam, the electrons exit the electron source.

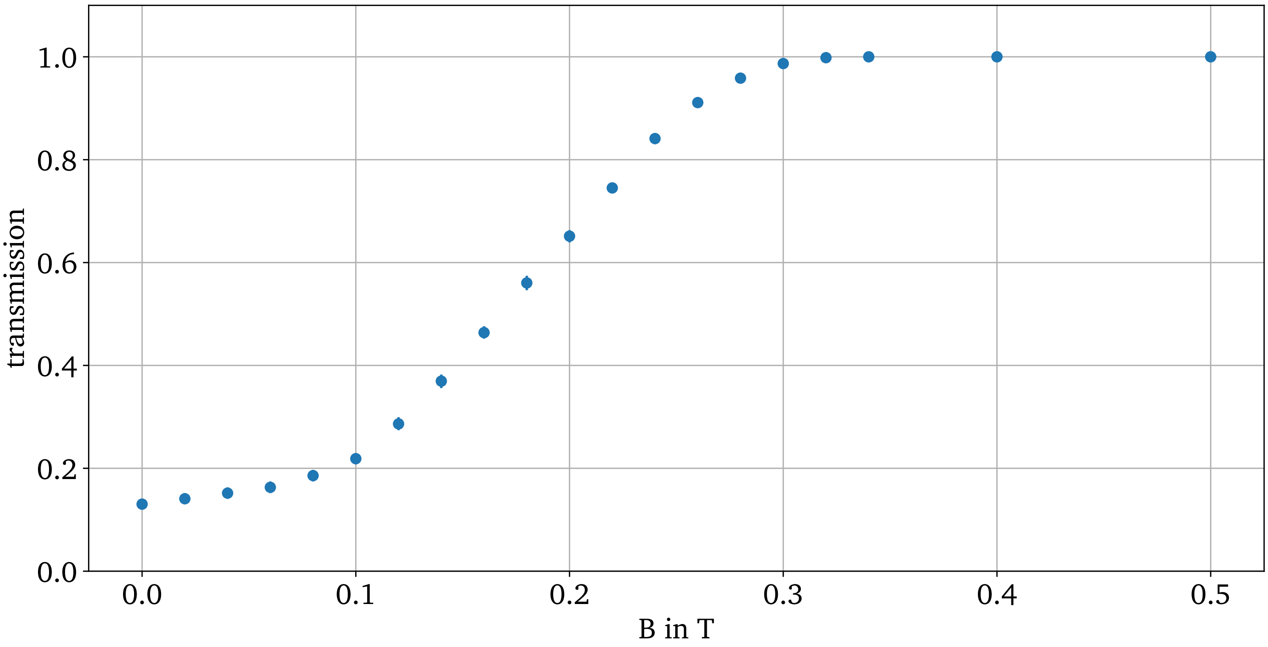

Figure 3.11.: The increase in transmission due to the focusing effect of the magnetic field simulated in SIMION®. Here, a magnetic field of $B = 0.34\,\mathrm{T}$ is sufficient to extract 100%.

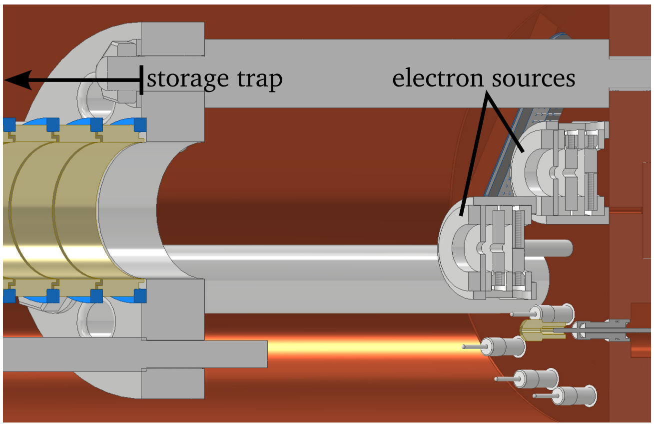

Figure 3.12.: The position of the two electron sources in the PUMA setup. They are placed 11 and 15 cm downstream and 11 mm off-center of the storage trap.

3.5. Testing the Electron Source

First, field emission points are tested in a simple setup (see Fig. 3.13). The field emission point is placed ~ 1 mm from a grounded plate, that is connected to an Ampere meter. The voltage on the field emission point is increased until a current can be measured. The initial voltage to induce field emission is upwards of 1000 V, but is reduced for “re-starting” the field emission point. Reducing the voltage required for a certain current, or equivalently, increasing the current produced by a certain voltage can be achieved by conditioning the field emission point. Drawing a current of 10^{-7} A to 10^{-6} A for about an hour can increase the produced current by a factor of 100.

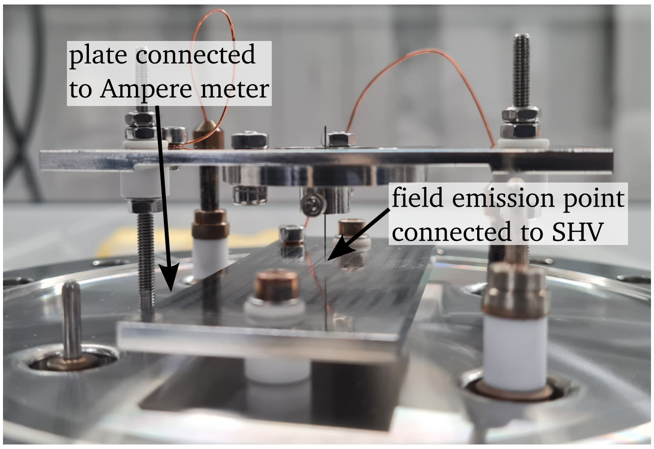

Figure 3.13.: Setup for the test of field emission points. The field emission point is connected to a power supply and the plate opposite to ground via an ammeter. The distance between them is about 1 mm.

A measurement of the produced current while varying the voltage shows the field emission nature, as it follows the Fowler-Nordheim equation (see Eq. 3.31). It is typically rearranged to the form of a linear equation, and the corresponding plot is called a Fowler-Nordheim plot (see left panel of Fig. 3.14). The same data is also shown in more familiar way in the right panel of Fig. 3.14, but the relation of the current I to the voltage U is not obvious.

$$I = AU^2 \exp\left(B/U\right) \tag{3.31}$$

$$\Leftrightarrow \frac{I}{AU^2} = \exp\left(B/U\right) \tag{3.32}$$

$$\Leftrightarrow \ln\left(A\frac{I}{U^2}\right) = B\frac{1}{U} \tag{3.33}$$

$$\Leftrightarrow \underbrace{\ln\left(\frac{I}{U^2}\right)}_{y} = \underbrace{B\frac{1}{U}}_{mx}\underbrace{-\ln\left(A\right)}_{+b} \tag{3.34}$$

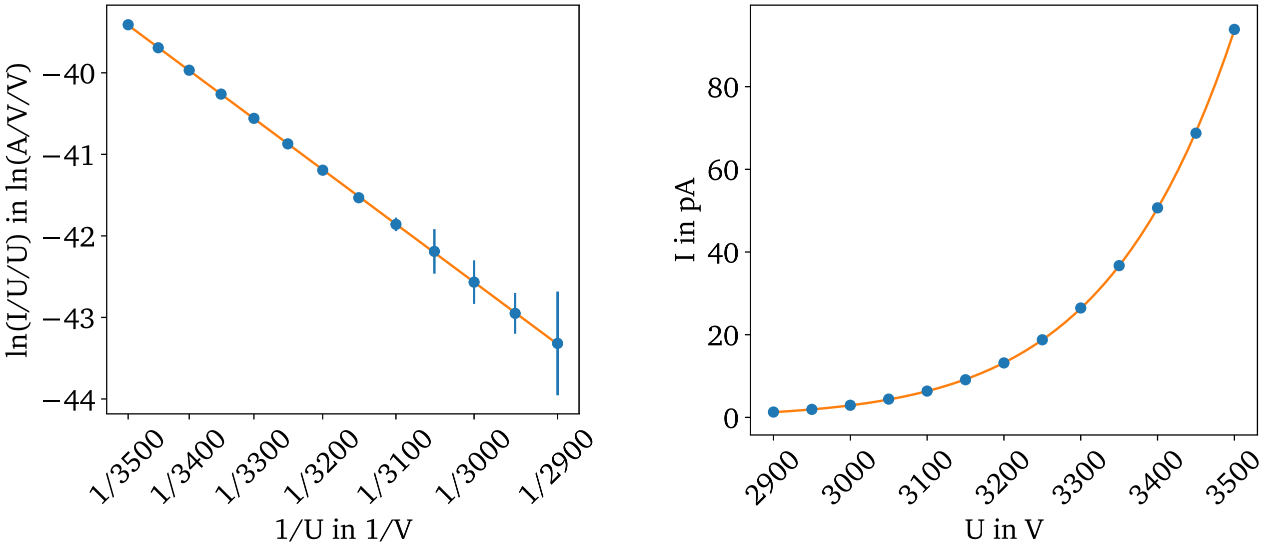

Figure 3.14.: Left: Fowler-Nordheim plot of one field emission point. The measurements follow the linear rearrangement of the Fowler-Nordheim equation (see Eq. 3.34). Right: A plot of the current produced by a field emission point over the voltage. This is the same data as in the left panel.

As an example, the current emitted over time by one field emission point is shown in Fig. 3.15. The stability of the emitted current was tested by setting the voltage to 450 V to produce a current of roughly $2.5 \cdot 10^{-10}$ A and monitored over 10 days. The behavior can be described by two phenomena, stable periods, that can last for several hours, and sudden jumps in current up to a factor of 10, that occur with no warning. This might be explained by the rearrangement of crystal planes in the tungsten field emission point, as different planes have different work functions [154, 160]. The normalized standard deviation σ_N

$$\sigma_\mathrm{N} = \frac{\sqrt{\mathrm{Var}(I)}}{\bar{I}} \tag{3.35}$$

is between 5% and 10% during the periods between the jumps.

The electron source was installed in the PUMA test trap setup in a test solenoid. The test trap is a Penning trap with the same dimensions as the PUMA storage trap, but at room temperature and in a 3 T magnetic field instead of 4 T. It consists of 22 electrodes with a diameter of 4 cm and a length of 2 cm. The electron source is placed 11 mm off-center, as in the PUMA cryostat, and 4 cm from the trap (see Fig. 3.16).

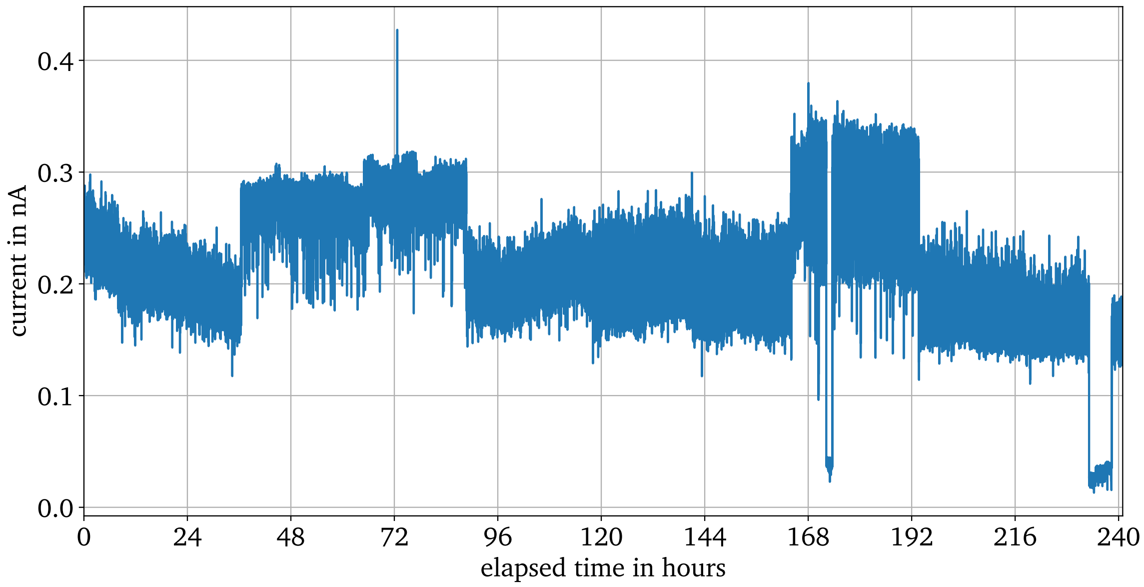

Figure 3.15.: The long term behavior of a field emission point over 10 days. The voltage was adjusted to produce roughly $2.5 \cdot 10^{-10}\,\mathrm{A}$. Periods of stable current emission are interrupted by sudden jumps in current that might originate from the rearrangement of crystal planes in the tungsten field emission point.

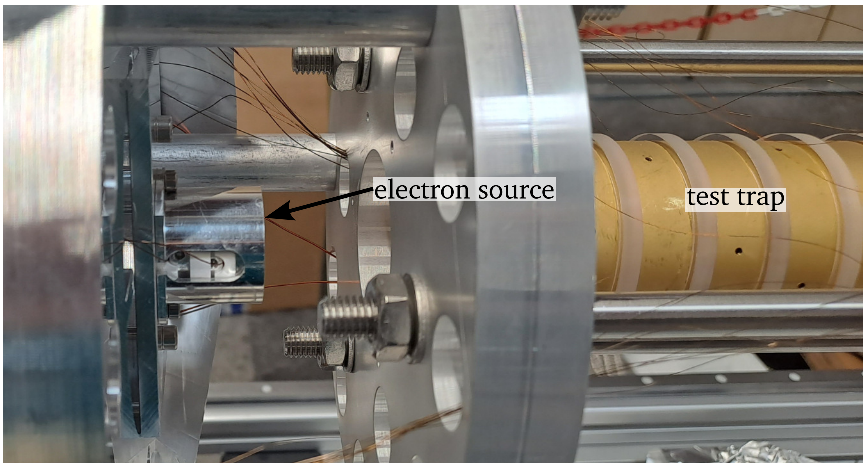

Figure 3.16.: The placement of the electron source upstream of the PUMA test trap. It is placed off-center to mimic the conditions in the PUMA cryostat.

A microchannel plate (MCP) with phosphor screen (compare Fig. 2.35) at the downstream end of the trap was used to measure the intensity of electrons traveling through the trap. As expected, without magnetic field there is barely any signal visible (compare Fig. 3.10). With increasing magnetic field (0.15 T) the intensity quickly rises and the beam spot migrates to its final position (see Fig. 3.17), matching the overall behavior expected from simulations (compare Fig. 3.11). The migration of the spot can be explained by a misalignment of the electron source-MCP axis with respect to the magnetic field. With perfect alignment, the spot would only focus and not move.

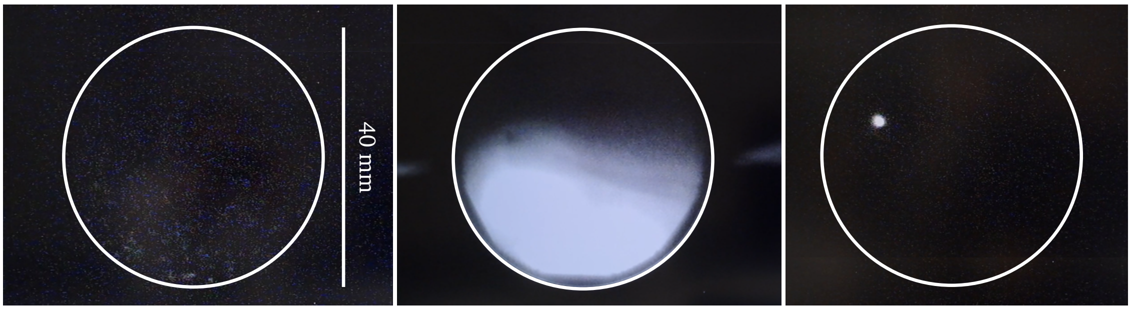

Figure 3.17.: Images of the MCP with no magnetic field (left), <0.15 T (middle) and >0.15 T (right). The increase in intensity is the effect of the magnetic field guiding the electrons along the field lines. The white circle indicates the extent of the 40 mm phosphor screen.

To confirm that the magnetic field guides all electrons out of the source, the transmission from the field emission point through the trap to the MCP was measured in a magnetic field of 0.2 T. The MCP was not used to amplify but only collect the current, connected to a picoammeter (Keithley Model 6485). The correlation between the current from the power supply (CAEN R1471ET) and the MCP is shown in Fig. 3.18. The Pearson correlation coefficient r_{xy} given by

$$r_{xy} = \frac{\sum_{i=1}^{n}(x_i - \bar{x})(y_i - \bar{y})}{\sqrt{\sum_{i=1}^{n}(x_i - \bar{x})^2}\sqrt{\sum_{i=1}^{n}(y_i - \bar{y})^2}} \tag{3.36}$$

measures linear correlation between two sets of data and is 1 for correlated data. For the data shown in Fig. 3.18 $r_{xy} = 0.999$, indicating a strongly correlated data set. Fitting a line reveals that $> 99\%$ of the current produced by the field emission point reaches the other side of the trap, confirming the simulation (see Fig. 3.10).

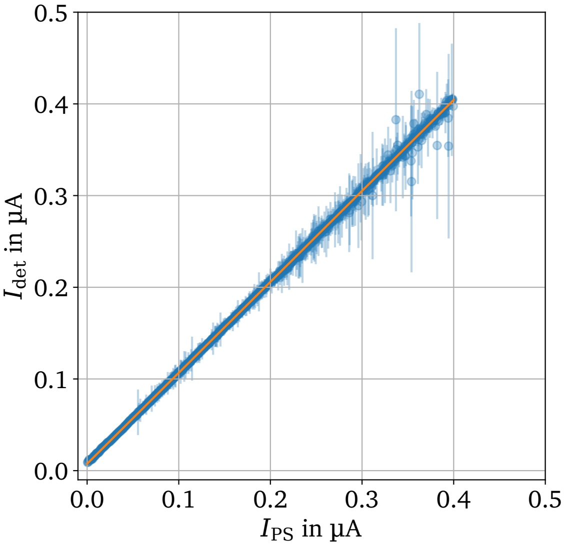

Figure 3.18.: Correlation between the current provided by the power supply and the current measured on the MCP on the other side of the trap. The data is shown in blue and a linear fit in orange. The currents strongly correlate and more than 99% reaches the detector.

When increasing the magnetic field further from $\sim 0.15\,\mathrm{T}$ to 3 T, the intensity decreases (see Fig. 3.19). A decrease is also described in Refs. [161] and [162]. The authors of [161] describe a decrease to $\sim 85\%$ when increasing the magnetic field to 1.4 T at room temperature. In [162], a decrease above a critical magnetic field is reported, dropping to $\sim 40\%$ at 1.2 T at liquid helium temperatures. Theoretical descriptions do not reproduce this decay, but predict a decrease like $1 - B^2$ for fields smaller than 5 T at zero temperature [163].

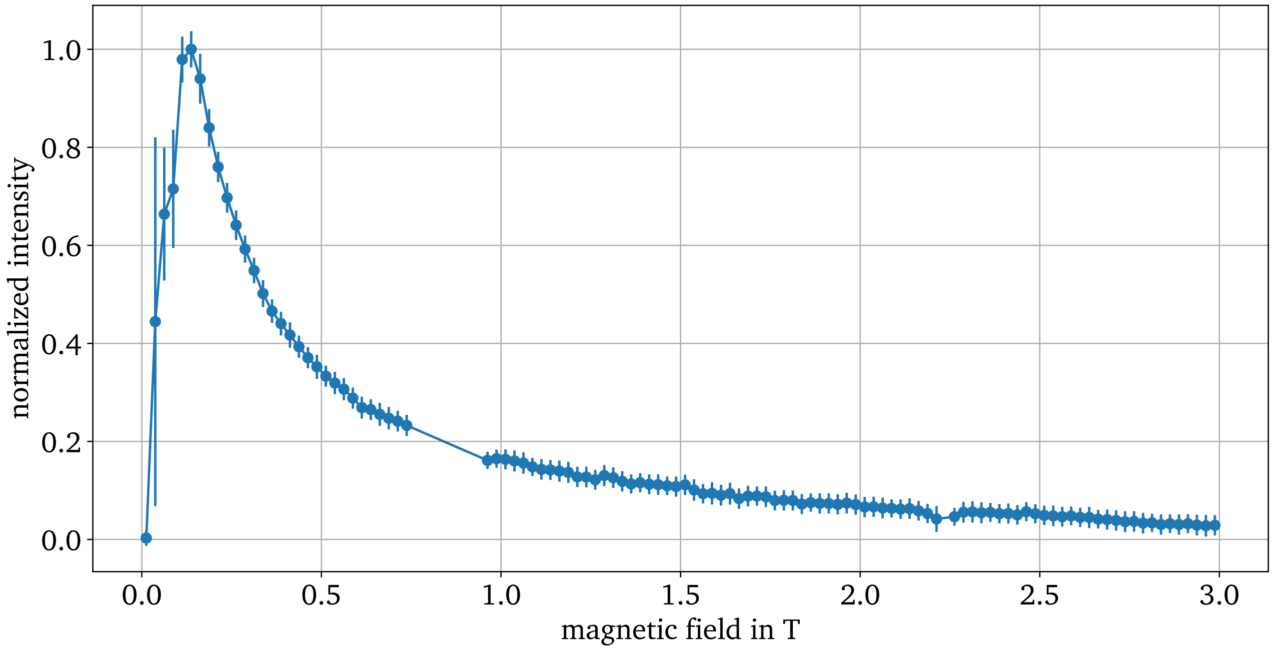

Figure 3.19.: The intensity measured with the MCP while varying the magnetic field between 0 and 3 T, normalized to the maximum. At magnetic fields $B > B(I_{\text{max}})$ all the current exits the electron source (see Fig. 3.18). The increase at low magnetic field can be explained by the focusing effect of the field (compare Fig. 3.10). A decreasing current with increasing magnetic field has also been reported in Refs. [161] and [162].

The current density under the influence of a magnetic field B parallel to the surface can be written as

$$|j_{\mathrm{B}}| = a\phi^{-1} \cdot E^2 \exp\left(-b\phi^{3/2}/\sqrt{E^2 - c^2B^2}\right) \tag{3.37}$$

according to Ref. [164], with a and b defined as is Eq. 3.26. The effect of a magnetic field perpendicular to the surface is zero [163, 165]. If we assume emission from a hemisphere with the magnetic field in the $\theta = 0$ direction, the component parallel to the surface, *i.e.*, perpendicular to the electric field is given by

$$|\vec{E} \times \vec{B}| = |\vec{E}||\vec{B}| \sin\theta. \tag{3.38}$$

Therefore, the total current I can be calculated by substituting $B \to \sin(\theta)B$ and integrating over θ

$$I = \int j_{\mathrm{B}} \mathrm{d}A \propto \int_0^{\frac{\pi}{2}} \exp\left(-b\phi^{3/2}/\sqrt{E^2 - c^2(\sin(\theta)B)^2}\right) \sin\theta \mathrm{d}\theta \tag{3.39}$$

Figure 3.20 shows the current density j_B and current I emitted from a hemispherical tungsten emitter ($\phi = 4.5\,\mathrm{eV}$) with $E = 550/128\,\mathrm{V/nm}$, using equations 3.38 and 3.39. The value for E was extracted from a Fowler-Nordheim plot using the electron source in the test setup. In this configuration the current is expected to drop to 80% at $B = 3\,\mathrm{T}$, but in our experimental setup the current drops to less than 10%. The decrease in current can be compensated by increasing the extractor voltage.

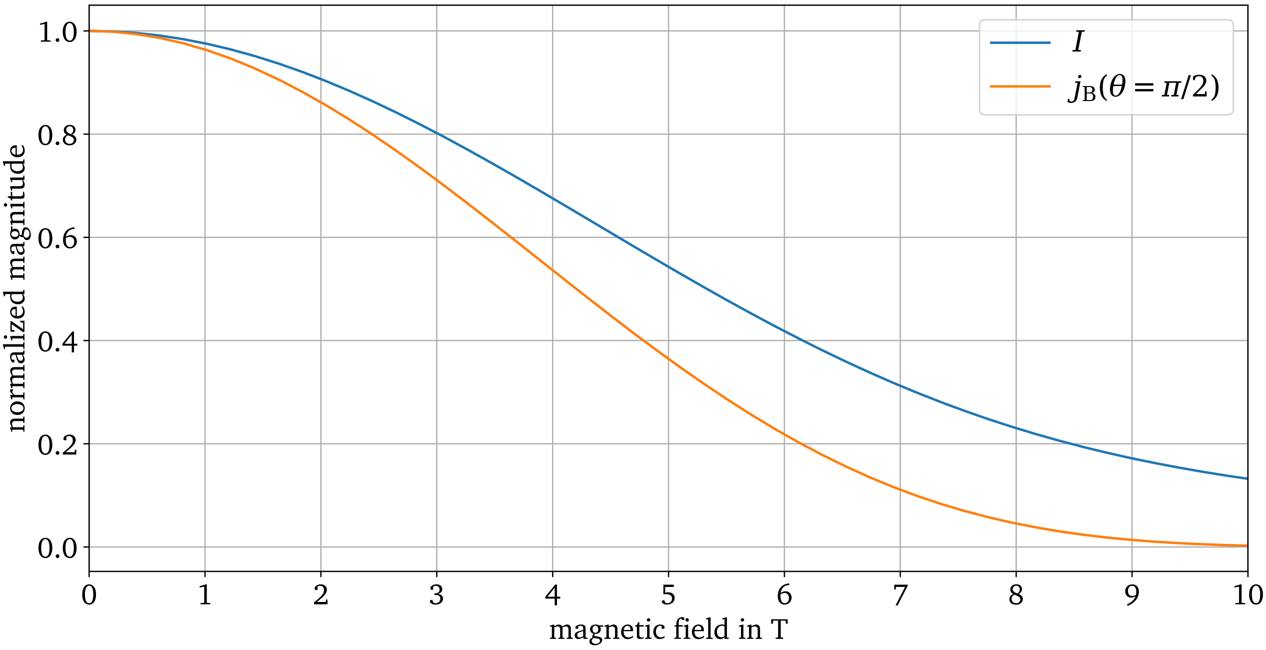

Figure 3.20.: The current density j_B and current I emitted from a hemispherical tungsten ($\phi = 4.5\,\mathrm{eV}$) emitter with $E(550\,\mathrm{V}) = 550/128\,\mathrm{V/nm}$. In this configuration, the current drops to 80% at $B = 3\,\mathrm{T}$.

The electron source was used to trap electrons in the PUMA test trap. Future characterizations of the electron source will include an investigation of the effect on the vacuum. Because the electrons are guided out of the source by the magnetic field and therefore do not collide with material on the way, it is expected that the influence on the vacuum is minimal.

3.6. Summary

A cold field emission electron source for the PUMA Penning trap was designed, built and commissioned in this work. The current-voltage relation of the manufactured field emission points follow the Fowler-Nordheim formula, confirming their field emission character. The electron source installed in the PUMA test trap produces a current of $\sim 10^{-7}\,\mathrm{A}$ with a potential difference of less than $1\,\mathrm{kV}$ between the field emission point and the extractor. A magnetic field is needed to guide the electrons out of the source, and a magnetic field of $0.2\,\mathrm{T}$ is already sufficient. A decrease in the extracted current with increasing magnetic field as reported in [161] and [162] was found, with no explanation yet. The decrease can be countered by increasing the extraction potential. The design of the electron source has been validated by the successful trapping of electrons in the PUMA test trap and two more electron sources have been built for the use in the PUMA Penning trap.

4. Conclusion

The PUMA experiment at CERN focuses on the study of the neutron-to-proton ratio in the density tail of stable and unstable nuclei using low-energy antiprotons. For this, up to 10^9 antiprotons will be stored in a transportable Penning trap. This work contributes to the high-efficiency accumulation of antiprotons for PUMA through the development of an antiproton deceleration beamline and a cold field emission electron source. Both are crucial for the manipulation of the antiproton kinetic energy to a level suitable for trapping.

In this work, the PUMA low energy antiproton beamline has been designed, built and commissioned. It serves four purposes. First, to decelerate antiprotons from 100 keV to 4 keV with high efficiency and energy-distribution-width preservation using a pulsed drift tube. Second, to allow the injection of ions from an ion source into the PUMA trap for experiments on stable isotopes. Third, to allow the transportable PUMA apparatus to be connected and disconnected from the beamline, and finally to provide a pressure of better than 10^{-10} mbar to the trap assembly. The strict vacuum requirement is due to the need to suppress the annihilation of antiprotons with residual gas molecules in order to prolong the antiproton storage time and to reduce the rate of background events during the measurement. To meet the vacuum requirements, careful consideration was given to material selection and extensive simulations were performed in MOLFLOW+ to ensure a sufficiently low pressure at the end of the beamline. Overall, a pressure in the order of 10^{-11} mbar is possible, as indicated by measurements on sections of the beamline. During the in-beam validation runs at ELENA, the antiproton beamline successfully decelerated antiprotons from 100 keV to (3898 ± 3) eV, with a transmission of $(55 \pm 3)\%$. The beam can be focused to a spot with $\sigma_{\text{horiz}} = (3.0 \pm 0.1)\,\text{mm}$, and $\sigma_{\text{vert}} = (3.8 \pm 0.2)\,\text{mm}$, demonstrating that it can be guided into the PUMA Penning trap. The length of the decelerated bunch is (93 ± 3) ns, which agrees with the simulated length and is relevant for the efficiency of the second deceleration from 4 keV to a few 100 eV right in front of the trap.

As part of this work, a cold field emission electron source for the PUMA Penning trap was designed and built. It provides electrons that cool the antiprotons in the Penning trap by collisions to reduce their energy further, from a few 100 eV to a few eV. The electrons also provide constant cooling during plasma manipulation. With a voltage difference of less than 1 kV between the field emission point and the extractor, the electron source installed in the PUMA test trap produces a current of $100\,\text{nA}$. A magnetic field is needed to funnel the electrons out of the source, with a field of 0.2 T being sufficient. When increasing the magnetic field, a decrease in the extracted current has been found, which has to be investigated further. The decrease can be counteracted by increasing the extraction potential. The design of the electron source has been validated by the successful trapping of electrons in the PUMA test trap, and two more electron sources have been built for use in a test trap setup. Future characterization of the electron source will include an investigation of the effect on the vacuum and operation in a pulsed mode.

With the systems for the manipulation of the antiprotons' energy ready, the PUMA trap can be transported to CERN and connected to the antiproton beamline. This opens the door for nuclear physics experiments with trapped antiprotons and stable as well as unstable ions at CERN.

Bibliography

[1] Meng Wang et al. "The AME 2020 atomic mass evaluation (II). Tables, graphs and references*". In: *Chin. Phys. C* 45.3 (Mar. 2021), p. 030003. DOI: `10.1088/1674-1137/abddaf`.

[2] Roderick V Reid. "Local phenomenological nucleon-nucleon potentials". In: *Ann. Phys.* 50.3 (1968), pp. 411–448. DOI: `10.1016/0003-4916(68)90126-7`.

[3] Edward Gerjuoy and Julian Schwinger. "On Tensor Forces and the Theory of Light Nuclei". In: *Phys. Rev.* 61 (3-4 Feb. 1942), pp. 138–146. DOI: `10.1103/PhysRev.61.138`.

[4] Joseph V. Lepore. "Polarization of Neutrons and Protons by Scattering". In: *Phys. Rev.* 79 (1 July 1950), pp. 137–142. DOI: `10.1103/PhysRev.79.137`.

[5] J. L. Gammel and R. M. Thaler. "Spin-Orbit Coupling in the Proton-Proton Interaction". In: *Phys. Rev.* 107 (1 July 1957), pp. 291–298. DOI: `10.1103/PhysRev.107.291`.

[6] M. Lacombe et al. "Parametrization of the Paris $N-N$ potential". In: *Phys. Rev. C* 21 (3 Mar. 1980), pp. 861–873. DOI: `10.1103/PhysRevC.21.861`.

[7] R. B. Wiringa, V. G. J. Stoks, and R. Schiavilla. "Accurate nucleon-nucleon potential with charge-independence breaking". In: *Phys. Rev. C* 51 (1 Jan. 1995), pp. 38–51. DOI: `10.1103/PhysRevC.51.38`.

[8] Hideki YUKAWA. "On the Interaction of Elementary Particles. I". In: *J. Phys. Soc. Jpn. 3rd Series* 17 (1935), pp. 48–57. DOI: `10.11429/ppmsj1919.17.0_48`.

[9] R. Machleidt, K. Holinde, and Ch. Elster. "The bonn meson-exchange model for the nucleon—nucleon interaction". In: *Phys. Rep.* 149.1 (1987), pp. 1–89. DOI: `10.1016/S0370-1573(87)80002-9`.

[10] S.A. Coon et al. "The two-pion-exchange three-nucleon potential and nuclear matter". In: *Nucl. Phys. A* 317.1 (1979), pp. 242–278. DOI: `10.1016/0375-9474(79)90462-7`.

[11] Steven C. Pieper et al. "Realistic models of pion-exchange three-nucleon interactions". In: *Phys. Rev. C* 64 (1 June 2001), p. 014001. DOI: `10.1103/PhysRevC.64.014001`.

[12] Steven Weinberg. "Phenomenological Lagrangians". In: *Physica A: Statistical Mechanics and its Applications* 96.1 (1979), pp. 327–340. DOI: `10.1016/0378-4371(79)90223-1`.

[13] R. Machleidt and D.R. Entem. "Chiral effective field theory and nuclear forces". In: *Phys. Rep.* 503.1 (2011), pp. 1–75. DOI: `10.1016/j.physrep.2011.02.001`.

[14] L. Coraggio et al. "Reduced regulator dependence of neutron-matter predictions with perturbative chiral interactions". In: *Phys. Rev. C* 87 (1 Jan. 2013), p. 014322. DOI: `10.1103/PhysRevC.87.014322`.

[15] R Machleidt and F Sammarruca. "Chiral EFT based nuclear forces: achievements and challenges". In: *Phys. Scr.* 91.8 (July 2016), p. 083007. DOI: `10.1088/0031-8949/91/8/083007`.

[16] T.H.R. Skyrme. "The effective nuclear potential". In: *Nuclear Physics* 9.4 (1958), pp. 615–634. DOI: `10.1016/0029-5582(58)90345-6`.

[17] J. Bartel et al. “Towards a better parametrisation of Skyrme-like effective forces: A critical study of the SkM force”. In: *Nucl. Phys. A* 386.1 (1982), pp. 79–100. DOI: `10.1016/0375-9474(82)90403-1`.

[18] M. Beiner et al. “Nuclear ground-state properties and self-consistent calculations with the skyrme interaction: (I). Spherical description”. In: *Nucl. Phys. A* 238.1 (1975), pp. 29–69. DOI: `10.1016/0375-9474(75)90338-3`.

[19] J. Dechargé and D. Gogny. “Hartree-Fock-Bogolyubov calculations with the $D1$ effective interaction on spherical nuclei”. In: *Phys. Rev. C* 21 (4 Apr. 1980), pp. 1568–1593. DOI: `10.1103/PhysRevC.21.1568`.

[20] B. D. Carlsson et al. “Uncertainty Analysis and Order-by-Order Optimization of Chiral Nuclear Interactions”. In: *Phys. Rev. X* 6 (1 Feb. 2016), p. 011019. DOI: `10.1103/PhysRevX.6.011019`.

[21] G Hagen et al. “Emergent properties of nuclei from ab initio coupled-cluster calculations*”. In: *Phys. Scr.* 91.6 (May 2016), p. 063006. DOI: `10.1088/0031-8949/91/6/063006`.

[22] A. Lovato, N. Rocco, and R. Schiavilla. “Muon capture in nuclei: An ab initio approach based on Green’s function Monte Carlo methods”. In: *Phys. Rev. C* 100 (3 Sept. 2019), p. 035502. DOI: `10.1103/PhysRevC.100.035502`.

[23] B. S. Hu, Q. Wu, and F. R. Xu. “Ab initio many-body perturbation theory and no-core shell model*”. In: *Chin. Phys. C* 41.10 (Oct. 2017), p. 104101. DOI: `10.1088/1674-1137/41/10/104101`.

[24] Bruce R. Barrett, Petr Navrátil, and James P. Vary. “Ab initio no core shell model”. In: *Prog. Part. Nucl. Phys.* 69 (2013), pp. 131–181. DOI: `10.1016/j.ppnp.2012.10.003`.

[25] Takahiro Ohgoe and Masatoshi Imada. “Variational Monte Carlo method for electron-phonon coupled systems”. In: *Phys. Rev. B* 89 (19 May 2014), p. 195139. DOI: `10.1103/PhysRevB.89.195139`.

[26] Baishan Hu et al. “Ab initio predictions link the neutron skin of 208Pb to nuclear forces”. In: *Nature Physics* 18.10 (Oct. 2022), pp. 1196–1200. DOI: `10.1038/s41567-022-01715-8`.

[27] G.F. Burgio et al. “Neutron stars and the nuclear equation of state”. In: *Prog. Part. Nucl. Phys.* 120 (2021), p. 103879. DOI: `10.1016/j.ppnp.2021.103879`.

[28] X. Roca-Maza and N. Paar. “Nuclear equation of state from ground and collective excited state properties of nuclei”. In: *Prog. Part. Nucl. Phys.* 101 (2018), pp. 96–176. DOI: `10.1016/j.ppnp.2018.04.001`.

[29] James M. Lattimer and F. Douglas Swesty. “A generalized equation of state for hot, dense matter”. In: *Nucl. Phys. A* 535.2 (1991), pp. 331–376. DOI: `10.1016/0375-9474(91)90452-C`.

[30] K. Hebeler and A. Schwenk. “Chiral three-nucleon forces and neutron matter”. In: *Phys. Rev. C* 82 (1 July 2010), p. 014314. DOI: `10.1103/PhysRevC.82.014314`.

[31] S. Gandolfi, J. Carlson, and Sanjay Reddy. “Maximum mass and radius of neutron stars, and the nuclear symmetry energy”. In: *Phys. Rev. C* 85 (3 Mar. 2012), p. 032801. DOI: `10.1103/PhysRevC.85.032801`.

[32] T. Krüger et al. “Neutron matter from chiral effective field theory interactions”. In: *Phys. Rev. C* 88 (2 Aug. 2013), p. 025802. DOI: `10.1103/PhysRevC.88.025802`.

[33] J. Birkhan et al. “Electric Dipole Polarizability of ^{48}Ca and Implications for the Neutron Skin”. In: *Phys. Rev. Lett.* 118 (25 June 2017), p. 252501. DOI: `10.1103/PhysRevLett.118.252501`.

[34] H. Yasin et al. “Equation of State Effects in Core-Collapse Supernovae”. In: *Phys. Rev. Lett.* 124 (9 Mar. 2020), p. 092701. DOI: `10.1103/PhysRevLett.124.092701`.

[35] John Antoniadis et al. “A Massive Pulsar in a Compact Relativistic Binary”. In: *Science* 340.6131 (2013), p. 1233232. DOI: `10.1126/science.1233232`.

[36] E. Fonseca et al. “Refined Mass and Geometric Measurements of the High-mass PSR J0740+6620”. In: *Astrophys. J. Letters* 915.1 (July 2021), p. L12. DOI: `10.3847/2041-8213/ac03b8`.

[37] Roger W. Romani et al. “PSR J1810+1744: Companion Darkening and a Precise High Neutron Star Mass”. In: *Astrophys. J. Letters* 908.2 (Feb. 2021), p. L46. DOI: `10.3847/2041-8213/abe2b4`.

[38] Luca Baiotti. “Gravitational waves from neutron star mergers and their relation to the nuclear equation of state”. In: *Prog. Part. Nucl. Phys.* 109 (2019), p. 103714. DOI: `10.1016/j.ppnp.2019.103714`.

[39] X. Roca-Maza et al. “Neutron Skin of ^{208}Pb, Nuclear Symmetry Energy, and the Parity Radius Experiment”. In: *Phys. Rev. Lett.* 106 (25 June 2011), p. 252501. DOI: `10.1103/PhysRevLett.106.252501`.

[40] J. Heisenberg et al. “Elastic Electron Scattering by Pb^{208} And New Information About the Nuclear Charge Distribution”. In: *Phys. Rev. Lett.* 23 (24 Dec. 1969), pp. 1402–1405. DOI: `10.1103/PhysRevLett.23.1402`.

[41] B. Frois et al. “High-Momentum-Transfer Electron Scattering from ^{208}Pb”. In: *Phys. Rev. Lett.* 38 (4 Jan. 1977), pp. 152–155. DOI: `10.1103/PhysRevLett.38.152`.

[42] K. Tsukada et al. “First Elastic Electron Scattering from ^{132}Xe at the SCRIT Facility”. In: *Phys. Rev. Lett.* 118 (26 June 2017), p. 262501. DOI: `10.1103/PhysRevLett.118.262501`.

[43] G. Ewald et al. “Nuclear Charge Radii of ^{8,9}Li Determined by Laser Spectroscopy”. In: *Phys. Rev. Lett.* 93 (11 Sept. 2004), p. 113002. DOI: `10.1103/PhysRevLett.93.113002`.

[44] R. F. Garcia Ruiz et al. “Unexpectedly large charge radii of neutron-rich calcium isotopes”. In: *Nature Physics* 12.6 (June 2016), pp. 594–598. DOI: `10.1038/nphys3645`.

[45] R Neugart et al. “Collinear laser spectroscopy at ISOLDE: new methods and highlights”. In: *J. Phys. G Nucl. Part. Phys.* 44.6 (Apr. 2017), p. 064002. DOI: `10.1088/1361-6471/aa6642`.

[46] Felix Sommer et al. “Charge Radii of ^{55,56}Ni Reveal a Surprisingly Similar Behavior at $N = 28$ in Ca and Ni Isotopes”. In: *Phys. Rev. Lett.* 129 (13 Sept. 2022), p. 132501. DOI: `10.1103/PhysRevLett.129.132501`.

[47] Randolf Pohl et al. “The size of the proton”. In: *Nature* 466.7303 (July 2010), pp. 213–216. DOI: `10.1038/nature09250`.

[48] Randolf Pohl et al. “Laser spectroscopy of muonic deuterium”. In: *Science* 353.6300 (2016), pp. 669–673. DOI: `10.1126/science.aaf2468`.

[49] Julian J. Krauth et al. “Measuring the α-particle charge radius with muonic helium-4 ions”. In: *Nature* 589.7843 (Jan. 2021), pp. 527–531. DOI: `10.1038/s41586-021-03183-1`.

[50] G. Fricke et al. “Nuclear Ground State Charge Radii from Electromagnetic Interactions”. In: *At. Data Nucl. Data Tables* 60.2 (1995), pp. 177–285. DOI: `10.1006/adnd.1995.1007`.

[51] W. Nörtershäuser and I. D. Moore. “Nuclear Charge Radii”. In: *Handbook of Nuclear Physics*. Ed. by Isao Tanihata, Hiroshi Toki, and Toshitaka Kajino. Singapore: Springer Nature Singapore, 2020, pp. 1–70. DOI: `10.1007/978-981-15-8818-1_41-1`.

[52] T.W. Donnelly, J. Dubach, and Ingo Sick. "Isospin dependences in parity-violating electron scattering". In: *Nucl. Phys. A* 503.3 (1989), pp. 589–631. DOI: `10.1016/0375-9474(89)90432-6`.

[53] C. J. Horowitz. "Parity violating elastic electron scattering and Coulomb distortions". In: *Phys. Rev. C* 57 (6 June 1998), pp. 3430–3436. DOI: `10.1103/PhysRevC.57.3430`.

[54] D. H. Beck and R. D. McKeown. "PARITY-VIOLATING ELECTRON SCATTERING AND NUCLEON STRUCTURE". In: *Annu. Rev. Nucl. Part. Sci.* 51.1 (2001), pp. 189–217. DOI: `10.1146/annurev.nucl.51.101701.132312`.

[55] D. Antypas et al. "Isotopic variation of parity violation in atomic ytterbium". In: *Nature Physics* 15.2 (Feb. 2019), pp. 120–123. DOI: `10.1038/s41567-018-0312-8`.

[56] D. Adhikari et al. "Accurate Determination of the Neutron Skin Thickness of ^{208}Pb through Parity-Violation in Electron Scattering". In: *Phys. Rev. Lett.* 126 (17 Apr. 2021), p. 172502. DOI: `10.1103/PhysRevLett.126.172502`.

[57] H. De Vries, C.W. De Jager, and C. De Vries. "Nuclear charge-density-distribution parameters from elastic electron scattering". In: *At. Data Nucl. Data Tables* 36.3 (1987), pp. 495–536. DOI: `10.1016/0092-640X(87)90013-1`.

[58] B. Buck. "Calculation of Elastic and Inelastic Proton Scattering with a Generalized Optical Model". In: *Phys. Rev.* 130 (2 Apr. 1963), pp. 712–726. DOI: `10.1103/PhysRev.130.712`.

[59] G. Hagen and N. Michel. "Elastic proton scattering of medium mass nuclei from coupled-cluster theory". In: *Phys. Rev. C* 86 (2 Aug. 2012), p. 021602. DOI: `10.1103/PhysRevC.86.021602`.

[60] S. Hama et al. "Global Dirac optical potentials for elastic proton scattering from heavy nuclei". In: *Phys. Rev. C* 41 (6 June 1990), pp. 2737–2755. DOI: `10.1103/PhysRevC.41.2737`.

[61] S. Terashima et al. "Proton elastic scattering from tin isotopes at 295 MeV and systematic change of neutron density distributions". In: *Phys. Rev. C* 77 (2 Feb. 2008), p. 024317. DOI: `10.1103/PhysRevC.77.024317`.

[62] B. Krusche. "Nuclear mass form factors from coherent photoproduction of πmesons". In: *Eur. Phys. J. A* 26.1 (Oct. 2005), pp. 7–18. DOI: `10.1140/epja/i2005-10146-7`.

[63] F. Colomer et al. "Theoretical analysis of the extraction of neutron skin thickness from coherent π^0 photoproduction off nuclei". In: *Phys. Rev. C* 106 (4 Oct. 2022), p. 044318. DOI: `10.1103/PhysRevC.106.044318`.

[64] T. Suzuki et al. "Neutron Skin of Na Isotopes Studied via Their Interaction Cross Sections". In: *Phys. Rev. Lett.* 75 (18 Oct. 1995), pp. 3241–3244. DOI: `10.1103/PhysRevLett.75.3241`.

[65] S. Bagchi et al. "Neutron skin and signature of the N = 14 shell gap found from measured proton radii of 17−22N". In: *Phys. Lett. B* 790 (2019), pp. 251–256. DOI: `10.1016/j.physletb.2019.01.024`.

[66] C. M. Tarbert et al. "Neutron Skin of ^{208}Pb from Coherent Pion Photoproduction". In: *Phys. Rev. Lett.* 112 (24 June 2014), p. 242502. DOI: `10.1103/PhysRevLett.112.242502`.

[67] J. Zenihiro et al. "Neutron density distributions of ^{204,206,208}Pb deduced via proton elastic scattering at $E_p = 295$ MeV". In: *Phys. Rev. C* 82 (4 Oct. 2010), p. 044611. DOI: `10.1103/PhysRevC.82.044611`.

[68] E. Friedman. "Neutron skins of 208Pb and 48Ca from pionic probes". In: *Nucl. Phys. A* 896 (2012), pp. 46–52. DOI: `10.1016/j.nuclphysa.2012.09.007`.

[69] B. Kłos et al. “Neutron density distributions from antiprotonic ^{208}Pb and ^{209}Bi atoms”. In: *Phys. Rev. C* 76 (1 July 2007), p. 014311. DOI: `10.1103/PhysRevC.76.014311`.

[70] A. Tamii et al. “Complete Electric Dipole Response and the Neutron Skin in ^{208}Pb”. In: *Phys. Rev. Lett.* 107 (6 Aug. 2011), p. 062502. DOI: `10.1103/PhysRevLett.107.062502`.

[71] A. Trzci ńska et al. “Neutron Density Distributions Deduced from Antiprotonic Atoms”. In: *Phys. Rev. Lett.* 87 (8 Aug. 2001), p. 082501. DOI: `10.1103/PhysRevLett.87.082501`.

[72] F. J. Fattoyev, J. Piekarewicz, and C. J. Horowitz. “Neutron Skins and Neutron Stars in the Multimessenger Era”. In: *Phys. Rev. Lett.* 120 (17 Apr. 2018), p. 172702. DOI: `10.1103/PhysRevLett.120.172702`.

[73] I. Tanihata et al. “Measurements of Interaction Cross Sections and Nuclear Radii in the Light p-Shell Region”. In: *Phys. Rev. Lett.* 55 (24 Dec. 1985), pp. 2676–2679. DOI: `10.1103/PhysRevLett.55.2676`.

[74] Aumann, T. et al. “PUMA, antiProton unstable matter annihilation - PUMA collaboration”. In: *Eur. Phys. J. A* 58.5 (2022), p. 88. DOI: `10.1140/epja/s10050-022-00713-x`.

[75] Isao Tanihata. “Neutron halo nuclei”. In: *J. Phys. G Nucl. Part. Phys.* 22.2 (Feb. 1996), p. 157. DOI: `10.1088/0954-3899/22/2/004`.

[76] P. Descouvemont. “Halo structure of ^{14}Be in a microscopic ^{12}Be+n+n cluster model”. In: *Phys. Rev. C* 52 (2 Aug. 1995), pp. 704–710. DOI: `10.1103/PhysRevC.52.704`.

[77] K. J. Cook et al. “Halo Structure of the Neutron-Dripline Nucleus ^{19}B”. In: *Phys. Rev. Lett.* 124 (21 May 2020), p. 212503. DOI: `10.1103/PhysRevLett.124.212503`.

[78] K. Tanaka et al. “Observation of a Large Reaction Cross Section in the Drip-Line Nucleus $^{22}\mathbf{C}$”. In: *Phys. Rev. Lett.* 104 (6 Feb. 2010), p. 062701. DOI: `10.1103/PhysRevLett.104.062701`.

[79] G.A. Korolev et al. “Halo structure of 8B determined from intermediate energy proton elastic scattering in inverse kinematics”. In: *Phys. Lett. B* 780 (2018), pp. 200–204. DOI: `10.1016/j.physletb.2018.03.013`.

[80] Bernhard Maaß et al. “Towards laser spectroscopy of the proton-halo candidate boron-8”. In: *Hyperfine Interact.* 238.1 (Feb. 2017), p. 25. DOI: `10.1007/s10751-017-1399-5`.

[81] H-W Hammer, C Ji, and D R Phillips. “Effective field theory description of halo nuclei”. In: *J. Phys. G Nucl. Part. Phys.* 44.10 (Sept. 2017), p. 103002. DOI: `10.1088/1361-6471/aa83db`.

[82] G. Hagen, T. Papenbrock, and M. Hjorth-Jensen. “Ab Initio Computation of the $^{17}\mathbf{F}$ Proton Halo State and Resonances in $A = 17$ Nuclei”. In: *Phys. Rev. Lett.* 104 (18 May 2010), p. 182501. DOI: `10.1103/PhysRevLett.104.182501`.

[83] James S. Cohen. “Capture of antiprotons by some radioactive atoms and ions”. In: *Phys. Rev. A* 69 (2 Feb. 2004), p. 022501. DOI: `10.1103/PhysRevA.69.022501`.

[84] D. Gotta et al. “X-ray transitions from antiprotonic noble gases”. In: *Eur. Phys. J. D* 47.1 (Apr. 2008), pp. 11–26. DOI: `10.1140/epjd/e2008-00025-3`.

[85] G. R. Burbidge and A. H. de Borde. “The Mesonic Auger Effect”. In: *Phys. Rev.* 89 (1 Jan. 1953), pp. 189–193. DOI: `10.1103/PhysRev.89.189`.

[86] Alexander Schmidt. “Development of the PUMA Antiproton and Ion Trap”. en. PhD thesis. Darmstadt: Technische Universität Darmstadt, Jan. 2024, xv, 173 Seiten. DOI: `10.26083/tuprints-00026510`.

[87] A. Deloff and J. Law. “Strong-interaction effects in antiprotonic atoms”. In: *Phys. Rev. C* 10 (6 Dec. 1974), pp. 2657–2658. DOI: `10.1103/PhysRevC.10.2657`.

[88] P. Roberson et al. “Strong interaction and mass measurements using antiprotonic atoms”. In: *Phys. Rev. C* 16 (5 Nov. 1977), pp. 1945–1962. DOI: `10.1103/PhysRevC.16.1945`.

[89] J. Côté et al. “Nucleon-Antinucleon Optical Potential”. In: *Phys. Rev. Lett.* 48 (19 May 1982), pp. 1319–1322. DOI: `10.1103/PhysRevLett.48.1319`.

[90] Tsuguo Suzuki and Hajime Narumi. “Microscopic approach to the antiproton-nucleus optical potential”. In: *Nucl. Phys. A* 426.3 (1984), pp. 413–430. DOI: `10.1016/0375-9474(84)90156-8`.

[91] C.J. Batty, E. Friedman, and J. Lichtenstadt. “Optical potentials for low energy antiproton-nucleus interactions”. In: *Phys. Lett. B* 142.4 (1984), pp. 241–244. DOI: `10.1016/0370-2693(84)91190-0`.

[92] R. Lazauskas and J. Carbonell. “Antiproton-deuteron hydrogenic states in optical models”. In: *Phys. Lett. B* 820 (2021), p. 136573. DOI: `10.1016/j.physletb.2021.136573`.

[93] B. El-Bennich et al. “Paris $N\overline{N}$ potential constrained by recent antiprotonic-atom data and $\overline{n}p$ total cross sections”. In: *Phys. Rev. C* 79 (5 May 2009), p. 054001. DOI: `10.1103/PhysRevC.79.054001`.

[94] M. Leon and R. Seki. “Determination of the neutron halo from antiproton absorption”. In: *Phys. Lett. B* 48.3 (1974), pp. 173–175. DOI: `10.1016/0370-2693(74)90001-X`.

[95] W. M. Bugg et al. “Evidence for a Neutron Halo in Heavy Nuclei from Antiproton Absorption”. In: *Phys. Rev. Lett.* 31 (7 Aug. 1973), pp. 475–478. DOI: `10.1103/PhysRevLett.31.475`.

[96] L. Linssen et al. “Measurement of antiproton-proton small-angle elastic scattering at low momentum”. In: *Nucl. Phys. A* 469.4 (1987), pp. 726–748. DOI: `10.1016/0375-9474(87)90023-6`.

[97] P. Kroll and W. Schweiger. “Analysis of low-energy antiproton-proton forward scattering”. In: *Nucl. Phys. A* 503.3 (1989), pp. 865–884. DOI: `10.1016/0375-9474(89)90444-2`.

[98] R. Timmermans, Th. A. Rijken, and J. J. de Swart. “Antiproton-proton partial-wave analysis below 925 MeV/c”. In: *Phys. Rev. C* 50 (1 July 1994), pp. 48–73. DOI: `10.1103/PhysRevC.50.48`.

[99] L A Kondratyuk and M G Sapozhnikov. “Interaction of antiprotons with neutrons and nuclei at lear energies”. In: *Sov. J. Nucl. Phys. (Engl. Transl.); (United States)* 46:1 (July 1987).

[100] Jayanti Mahalanabis. “Determination of antiproton-neutron amplitude from elastic¯p-deuteron scattering at 600 MeV/c”. In: *Zeitschrift für Physik A Hadrons and Nuclei* 342.1 (Mar. 1992), pp. 101–105. DOI: `10.1007/BF01294494`.

[101] W. Brückner et al. “Search for a narrow resonance in antiproton-proton annihilation cross sections in the beam momentum range between 400 and 600 MeV/c”. In: *Phys. Lett. B* 197.3 (1987), pp. 463–468. DOI: `10.1016/0370-2693(87)90421-7`.

[102] D. Rohmann et al. “Measurement of the 4f strong interaction level width in light antiprotonic atoms”. In: *Zeitschrift für Physik A Atomic Nuclei* 325.3 (Sept. 1986), pp. 261–265. DOI: `10.1007/BF01294606`.

[103] Th. Köhler et al. “Precision measurement of strong interaction isotope effects in antiprotonic 16O, 17O, and 18O atoms”. In: *Phys. Lett. B* 176.3 (1986), pp. 327–333. DOI: `10.1016/0370-2693(86)90173-5`.

[104] P. L. McGaughey et al. “Dynamics of Low-Energy Antiproton Annihilation in Nuclei as Inferred from Inclusive Proton and Pion Measurements”. In: *Phys. Rev. Lett.* 56 (20 May 1986), pp. 2156–2159. DOI: `10.1103/PhysRevLett.56.2156`.

[105] J. Jastrzębski et al. “Signature of a neutron halo in 232Th from antiproton absorption”. In: *Nucl. Phys. A* 558 (1993), pp. 405–414. DOI: `10.1016/0375-9474(93)90409-Q`.

[106] D. Polster et al. “Light particle emission induced by stopped antiprotons in nuclei: Energy dissipation and neutron-to-proton ratio”. In: *Phys. Rev. C* 51 (3 Mar. 1995), pp. 1167–1180. DOI: `10.1103/PhysRevC.51.1167`.

[107] A Trzcińska et al. “Information on the nuclear periphery deduced from the properties of heavy antiprotonic atoms”. In: *Nucl. Instrum. Methods Phys. Res., Sect. B* 214 (2004). Low Energy Antiproton Physics (LEAP’03), pp. 157–159. DOI: `10.1016/j.nimb.2003.08.017`.

[108] Stephan Maury et al. “ELENA: the extra low energy anti-proton facility at CERN”. In: *Hyperfine Interact.* 229.1 (2014), pp. 105–115. DOI: `10.1016/0370-2693(74)90001-X`.

[109] Laurette Ponce et al. “ELENA - From Commissioning to Operation”. In: *JACoW IPAC* 2022 (2022), pp. 2391–2394. DOI: `10.18429/JACoW-IPAC2022-THOXGD1`.

[110] H. Kalinowsky. “Deceleration of antiprotons from MeV to keV energies”. In: *Hyperfine Interact.* 76.1 (Dec. 1993), pp. 73–80. DOI: `10.1007/BF02316707`.

[111] C. Amole et al. “The ALPHA antihydrogen trapping apparatus”. In: *Nucl. Instrum. Methods Phys. Res., Sect. A* 735 (2014), pp. 319–340. DOI: `10.1016/j.nima.2013.09.043`.

[112] M. Tajima et al. “Antiproton beams with low energy spread for antihydrogen production”. In: *J. Instrum.* 14.05 (May 2019), P05009. DOI: `10.1088/1748-0221/14/05/P05009`.

[113] A. Husson et al. “A pulsed high-voltage decelerator system to deliver low-energy antiprotons”. In: *Nucl. Instrum. Methods Phys. Res. A.* 1002 (2021), p. 165245. DOI: `10.1016/j.nima.2021.165245`.

[114] Claude Amsler et al. “Pulsed production of antihydrogen”. In: *Commun. Phys.* 4.1 (Feb. 2021), p. 19. DOI: `10.1038/s42005-020-00494-z`.

[115] B. M. Latacz et al. “Ultra-thin polymer foil cryogenic window for antiproton deceleration and storage”. In: *Rev. Sci. Instrum.* 94.10 (Oct. 2023), p. 103310. DOI: `10.1063/5.0167262`.

[116] K. Nordlund, M. Hori, and D. Sundholm. “Large nuclear scattering effects in antiproton transmission through polymer and metal-coated foils”. In: *Phys. Rev. A* 106 (1 July 2022), p. 012803. DOI: `10.1103/PhysRevA.106.012803`.

[117] N. Kuroda et al. “Confinement of a Large Number of Antiprotons and Production of an Ultraslow Antiproton Beam”. In: *Phys. Rev. Lett.* 94 (2 Jan. 2005), p. 023401. DOI: `10.1103/PhysRevLett.94.023401`.

[118] S.S. Fabbri and W. Bertsche. “Optimization of Antiproton Capture for Antihydrogen Creation in the ALPHA Experiment”. In: *Proc. IBIC’19* (Malmö, Sweden). International Beam Instrumentation Conferenc 8. JACoW Publishing, Geneva, Switzerland, Nov. 2019, pp. 637–641. DOI: `10.18429/JACoW-IBIC2019-WEPP040`.

[119] Jonas Fischer et al. “Design and characterization of an antiproton deceleration beamline for the PUMA experiment”. In: *Nucl. Instrum. Methods Phys. Res., Sect. B* 550 (2024), p. 165318. DOI: `10.1016/j.nimb.2024.165318`.

[120] F Herfurth et al. “A linear radiofrequency ion trap for accumulation, bunching, and emittance improvement of radioactive ion beams”. In: *Nucl. Instrum. Methods Phys. Res. A.* 469.2 (2001), pp. 254–275. DOI: `10.1016/S0168-9002(01)00168-1`.

[121] S. Coeck et al. “A pulsed drift cavity to capture 30keV ion bunches at ground potential”. In: *Nucl. Instrum. Methods Phys. Res. A.* 572.2 (2007), pp. 585–595. DOI: `10.1016/j.nima.2006.11.054`.

[122] J. Grund et al. “First online operation of TRIGA-TRAP”. In: *Nucl. Instrum. Methods Phys. Res. A.* 972 (2020), p. 164013. DOI: `10.1016/j.nima.2020.164013`.

[123] M. Schlaich et al. “A multi-reflection time-of-flight mass spectrometer for the offline ion source of the PUMA experiment”. In: *Int. J. Mass Spectrom.* 495 (2024), p. 117166. DOI: `10.1016/j.ijms.2023.117166`.

[124] P. Pérez et al. “The GBAR antimatter gravity experiment”. In: *Hyperfine Interact.* 233.1 (Aug. 2015), pp. 21–27. DOI: `10.1007/s10751-015-1154-8`.

[125] M.A. Fraser et al. “Beam Dynamics Studies of the ELENA Electrostatic Transfer Lines”. In: *Proc. 6th IPAC* (Richmond, VA, USA). International Particle Accelerator Conference 6. Geneva, Switzerland: JACoW, June 2015, pp. 385–388. DOI: `10.18429/JACoW-IPAC2015-MOPJE044`.

[126] M Martini and H Schönauer. *Emittance measurements in the CERN PS complex*. Tech. rep. Geneva: CERN, 1997.

[127] M. McLean et al. “Commissioning of the SEM-Grid Monitors for ELENA”. In: *Proc. IBIC'21* (Pohang, Rep. of Korea). International Beam Instrumentation Conference 10. JACoW Publishing, Geneva, Switzerland, Oct. 2021, TUPP14, pp. 223–226. DOI: `10.18429/JACoW-IBIC2021-TUPP14`.

[128] M. Taborelli and A. Mongelluzzop. *Vacuum firing of Stainless Steel*. CERN EDMS. 2017.

[129] Katharina Battes, Christian Day, and Volker Hauer. “Systematic study of the outgassing behavior of different ceramic materials”. In: *J. Vac. Sci. Technol. B* 39.3 (Apr. 2021), p. 034202. DOI: `10.1116/6.0000954`.

[130] C Benvenuti. “Extreme Vacua: Achievements and Expectations”. In: *Phys. Scr.* 1988.T22 (Jan. 1988), p. 48. DOI: `10.1088/0031-8949/1988/T22/006`.

[131] Scott R. Wilson. “Numerical modeling of vacuum systems using electronic circuit analysis tools”. In: *J. Vac. Sci. Technol. A* 5.4 (July 1987), pp. 2479–2483. DOI: `10.1116/1.574876`.

[132] CY Christina Yin Vallgren, PC Paolo Chiggiato, and JF Jose Antonio Ferreira Somoza. “Electrical Network Analysis for Vacuum Profile of MedAustron”. In: (2012).

[133] ChoiWon-Shik et al. “Calculation of Pressure Profiles in a Molecular Flow Regime using LTSpice IV”. In: *Appl. Sci. Converg. Technol.* 25.4 (July 2016), pp. 67–72.

[134] *LTspice*. `https://www.analog.com/en/design-center/design-tools-and-calculators/ltspice-simulator.html`. [Online; accessed 22-November-2023]. 2023.

[135] M. Saitoh et al. “Influence of vacuum gauges on outgassing rate measurements”. In: *J. Vac. Sci. Technol. A* 11.5 (Sept. 1993), pp. 2816–2821. DOI: `10.1116/1.578646`.

[136] Roberto Kersevan and Marton Ady. “Recent developments of Monte-Carlo codes Molflow+ and Synrad+”. In: (2019), TUPMP037. DOI: `10.18429/JACoW-IPAC2019-TUPMP037`.

[137] Martin Knudsen and J. R. Partington. “The Kinetic.Theoryof Gases. Some Modern Aspects”. In: *J. Phys. Chem.* 39.2 (1935), pp. 307–307. DOI: `10.1021/j150362a021`.

[138] M. J. Borchert et al. “A 16-parts-per-trillion measurement of the antiproton-to-proton charge–mass ratio”. In: *Nature* 601.7891 (Jan. 2022), pp. 53–57. DOI: `10.1038/s41586-021-04203-w`.

[139] D W Williams and W T Williams. “Effect of electrode surface finish on electrical breakdown in vacuum”. In: *J. Phys. D: Appl. Phys.* 5.10 (Oct. 1972), p. 1845. DOI: `10.1088/0022-3727/5/10/314`.

[140] D.C. Faircloth. “Technological Aspects: High Voltage”. In: (2013). Contribution to the CAS-CERN Accelerator School: Ion Sources, CERN-2013-007, pp. 381–419. DOI: `10.5170/CERN-2013-007.381`.

[141] *micro channel plate with magnification of a triple cascade (simplified) – german labels*. https://commons.wikimedia.org/wiki/File:Mcp-de.svg. [Online; accessed 10-April-2024]. 2024.

[142] Toshitaka Niwase et al. “Development of a β-TOF detector: An enhancement of the α-TOF detector for use with β-decaying nuclides”. In: *Prog. Theor. Exp.* 2023.3 (Mar. 2023), 031H01. DOI: `10.1093/ptep/ptad039`.

[143] Wolfgang Bartmann et al. “The ELENA facility”. In: *Philos. Trans. R. Soc. A* 376.2116 (2018), p. 20170266. DOI: `10.1098/rsta.2017.0266`.

[144] S. L. Rolston and G. Gabrielse. “Cooling antiprotons in an ion trap”. In: *Hyperfine Interact.* 44.1 (Mar. 1989), pp. 233–245. DOI: `10.1007/BF02398673`.

[145] Leon Brillouin. “A Theorem of Larmor and Its Importance for Electrons in Magnetic Fields”. In: *Phys. Rev.* 67 (7-8 Apr. 1945), pp. 260–266. DOI: `10.1103/PhysRev.67.260`.

[146] M. Hobein et al. “Evaporative Cooling and Coherent Axial Oscillations of Highly Charged Ions in a Penning Trap”. In: *Phys. Rev. Lett.* 106 (1 Jan. 2011), p. 013002. DOI: `10.1103/PhysRevLett.106.013002`.

[147] E. M. Hollmann, F. Anderegg, and C. F. Driscoll. “Confinement and manipulation of non-neutral plasmas using rotating wall electric fields”. In: *Phys. Plasmas* 7.7 (2000), pp. 2776–2789. DOI: `10.1063/1.874128`.

[148] F. Major, V. Gheorghe, and G. Werth. *Charged Particle Traps: Physics and Techniques of Charged Particle Field Confinement*. Springer, Berlin, Heidelberg, 2005.

[149] M. Vogel. *Particle Confinement in Penning Traps: An Introduction*. Springer International Publishing AG, 2018.

[150] Jr. L. Spitzer. *Physics of Fully Ionized Gases*. Interscience publishers, Inc., New York, 1956.

[151] Guo-Zhong Li, Shenheng Guan, and Alan G. Marshall. “Sympathetic cooling of trapped negative ions by self-cooled electrons in a fourier transform ion cyclotron resonance mass spectrometer”. In: *J. Am. Soc. Mass Spectrom.* 8.8 (1997), pp. 793–800. DOI: `10.1016/S1044-0305(97)84131-1`.

[152] X. Feng et al. “Capture and cooling of antiprotons”. In: *Hyperfine Interact.* 109.1 (Aug. 1997), pp. 145–152. DOI: `10.1023/A:1012601300032`.

[153] Daniel Krasnický. “Antiproton Capture and Cooling for Production of Cold Antihydrogen”. PhD thesis. Università degli Studi di Genova, 2013.

[154] A. V. Crewe et al. “Electron Gun Using a Field Emission Source”. In: *Rev. Sci. Instrum.* 39.4 (1968), pp. 576–583. DOI: `10.1063/1.1683435`.

[155] Ralph Howard Fowler and L. Nordheim. “Electron emission in intense electric fields”. In: *Proc. R. Soc. Lond. A* 119.781 (1928), pp. 173–181. DOI: `10.1098/rspa.1928.0091`.

[156] Matthew Redshaw et al. “Fabrication and characterization of field emission points for ion production in Penning trap applications”. In: *Int. J. Mass Spectrom.* 379 (2015), pp. 187–193. doi: `10.1016/j.ijms.2015.01.006`.

[157] J. P. Ibe et al. “On the electrochemical etching of tips for scanning tunneling microscopy”. In: *J. Vac. Sci. Technol.* 8.4 (1990), pp. 3570–3575. doi: `10.1116/1.576509`.

[158] Anne-Sophie Lucier. “Preparation and Characterization of Tungsten Tips Suitable for Molecular Electronics Studies”. MA thesis. McGill University Montréal, 2004.

[159] Jonas Fischer. “Plasma Diagnostics and Electron Source for PUMA”. MA thesis. Technische Universität Darmstadt, 2019.

[160] Keigo Kasuya et al. “Stabilization of a tungsten ⟨310⟩ cold field emitter”. In: *J. Vac. Sci. Technol. B* 28.5 (Sept. 2010), pp. L55–L60. doi: `10.1116/1.3488988`.

[161] I. Buribaev and B. B. Shishkin. “Field emission of electrons from tungsten in a magnetic field”. In: *Soviet Physics - Solid State* 12.11 (1971), pp. 2678–2679.

[162] P.J. Kennedy and A.Y. Muir. “Modification of field-emission currents from tungsten by external magnetic fields”. In: *Solid State Commun.* 27.3 (1978), pp. 279–281. doi: `10.1016/0038-1098(78)90035-2`.

[163] F. J. Blatt. “Field Emission in a Magnetic Field”. In: *Phys. Rev.* 131 (1 July 1963), pp. 166–169. doi: `10.1103/PhysRev.131.166`.

[164] S. Lebedynskyi et al. “DC vacuum breakdown in an external magnetic field”. In: *Nucl. Instrum. Methods Phys. Res., Sect. A* 908 (2018), pp. 318–324. doi: `10.1016/j.nima.2018.08.061`.

[165] S. O. Lebedynskyi et al. *The effect of a magnetic field on the motion of electrons for the field emission process description*. 2017. arXiv: `1702.02713 [quant-ph]`.

A. Beamline Parts

Table A.1.: The parts of the beamline (see Fig. A.1).

item	description
1.1	CF100-63 zero length reducer
1.2	CF63 tube 21cm
1.3	CF63-40 cross
1.4	Pfeiffer IKR070 gauge
1.5	VAT 57132-GE02 valve
1.6	VAb WBCF 63/29 bellow
1.7	CF250-63 zero length reducer
1.8	screw cover
1.9	Vacom HV125R-CE-CU39 high-voltage feedthrough
1.10	VAb custom chamber
1.11	VAb custom chamber
1.12	CF160-100 reducer
1.13	CF100 blind flange
1.14	SAES D2000-10 ion-NEG pump (behind)
1.15	CF100 T piece
1.16	CF40 SHV feedthrough
1.17	CF100-40 zero length reducer
1.18	CF160 blind flange
2.1	VAT 48236-CE44 valve
2.2	CF160-63 reducer
2.3	CF160 tube 20cm (einzel lens)
2.4	Agilent VacIon 300 StarCell ion pump
2.5	CF160 6-way cross
2.6	VAb LD 160-150 linear feedthrough
2.7	CF100 9xSHV feedthrough (Q-bender)
2.8	SEM grid
2.9	CF160 cross + 2xCF200
2.10	CF200 blind flange
3.1	CF63 cross
3.2	CF63-40 zero length reducer
4.1	SAES Z1000 NEG cartridge
4.2	CF160-63 cross

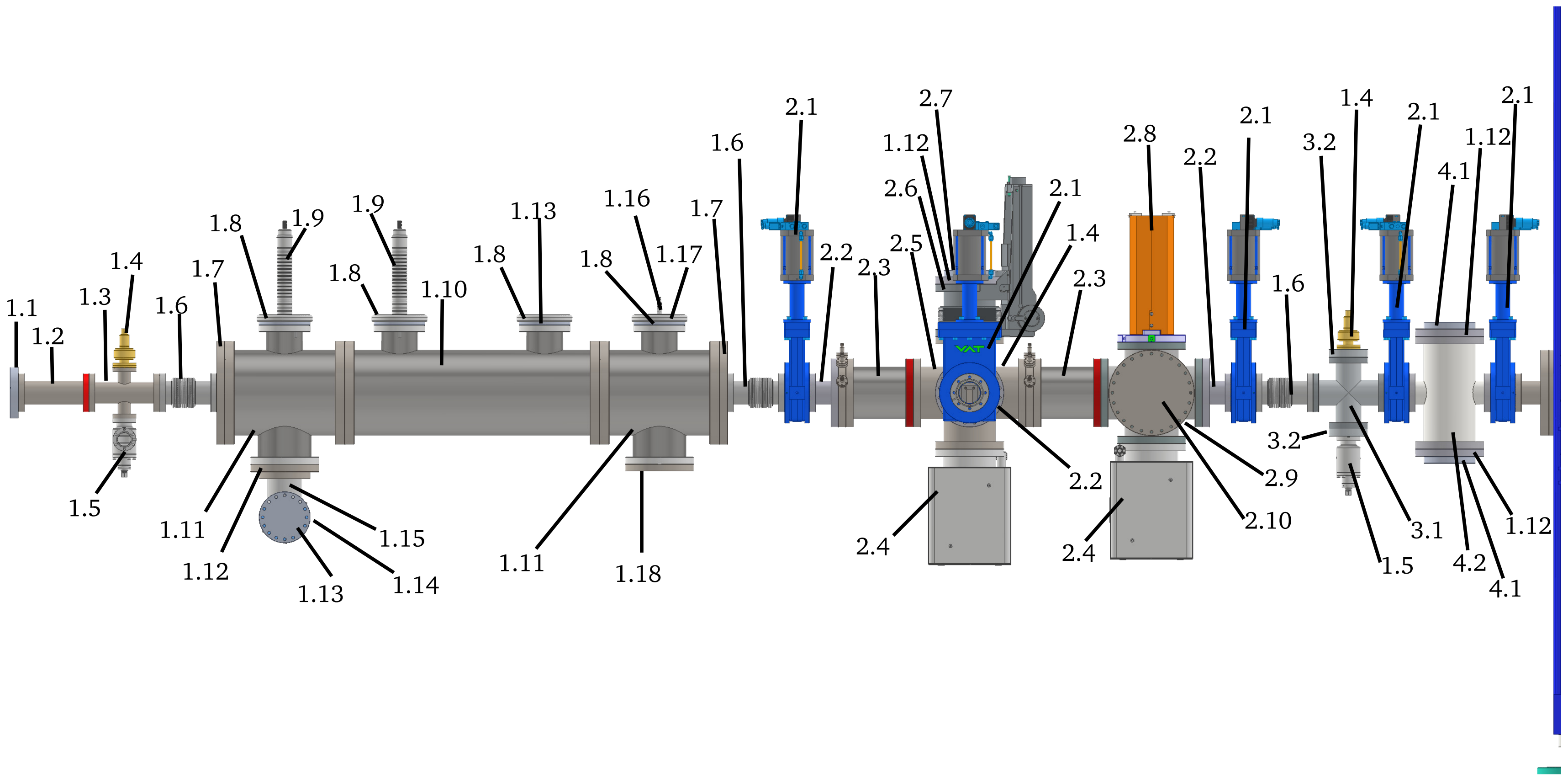

Figure A.1.: Overview over the PUMA antiproton beamline. The details can be found in table A.1.

B. Pulsed Drift Tube Technical Drawings

The following drawings are of

1. drift tube
2. floated einzel lens electrode
3. grounded einzel lens electrode
4. triple junction guard ring
5. holder rod grounded electrodes
6. holder bar einzel lens
7. holder bar drift tube
8. holder hoop
9. holder rod floated electrodes

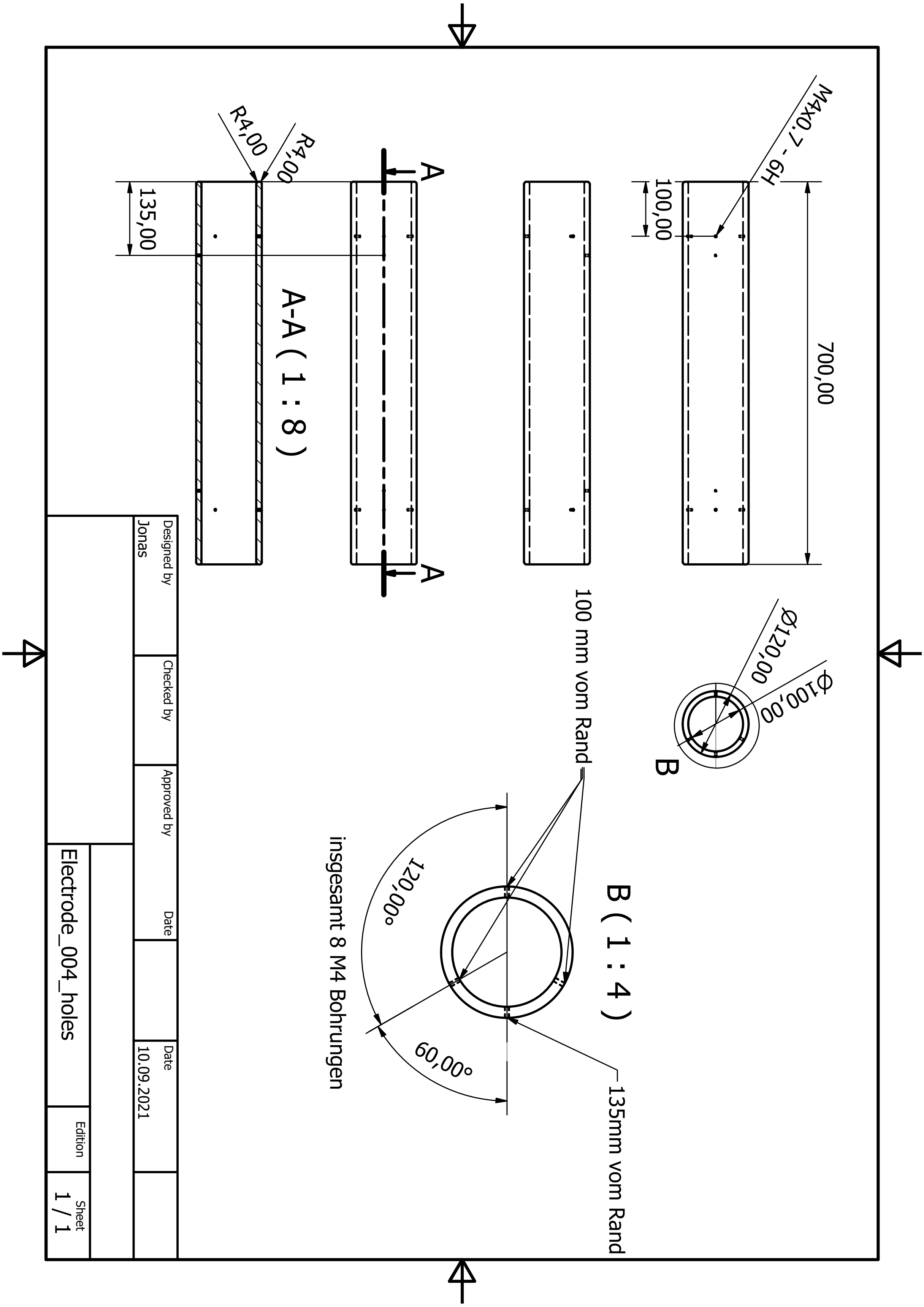
A
A
A-A (1 : 8)
R4,00
R4,00
135,00
100,00
700,00
M4x0.7 - 6H
Ø120,00
Ø100,00
B
B (1 : 4)
100 mm vom Rand
135mm vom Rand
120,00°
60,00°
insgesamt 8 M4 Bohrungen
Designed by
Jonas
Checked by
Approved by
Date
Date
10.09.2021
Electrode_004_holes
Edition
Sheet
1 / 1

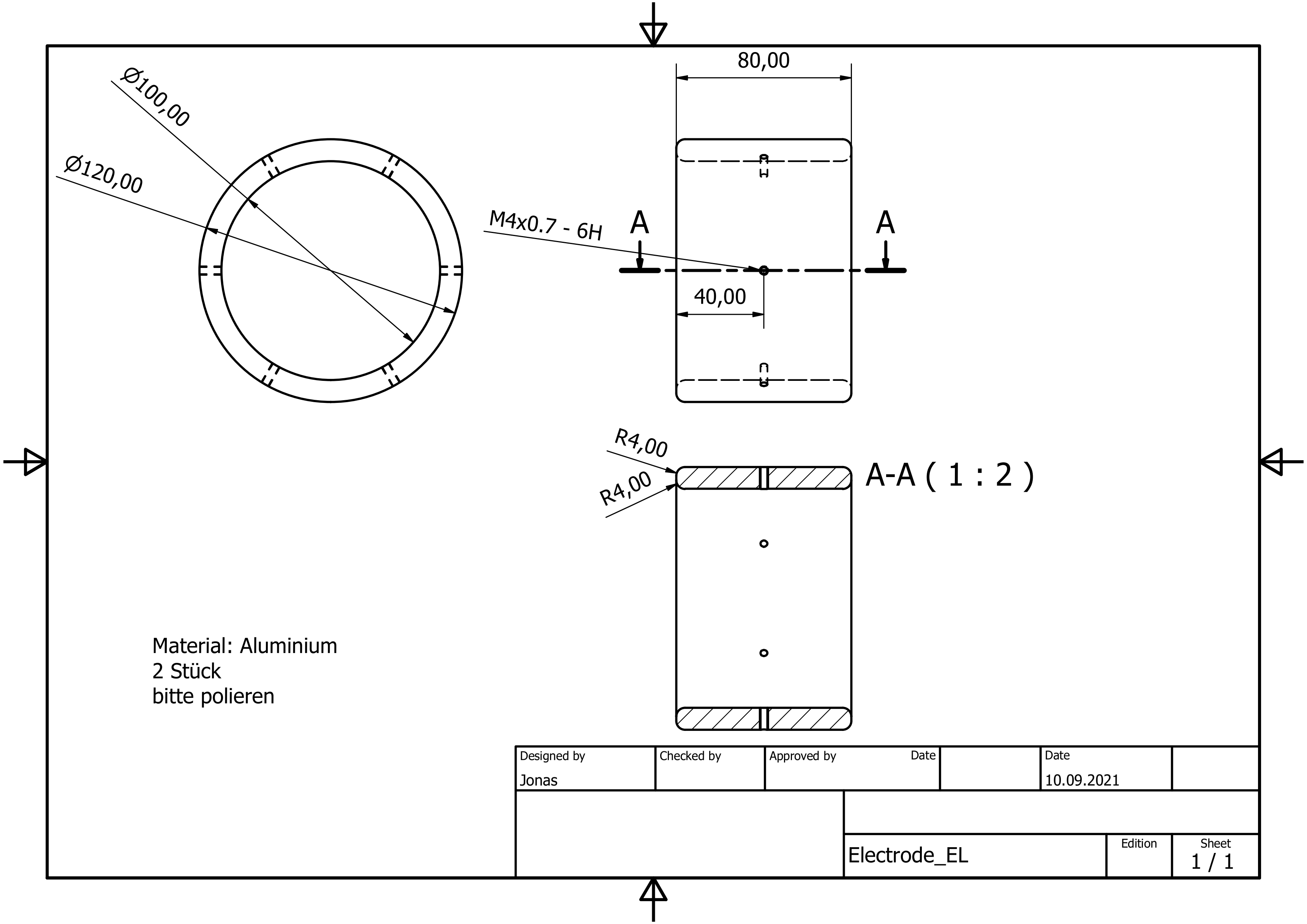

Material: Aluminium
2 Stück
bitte polieren

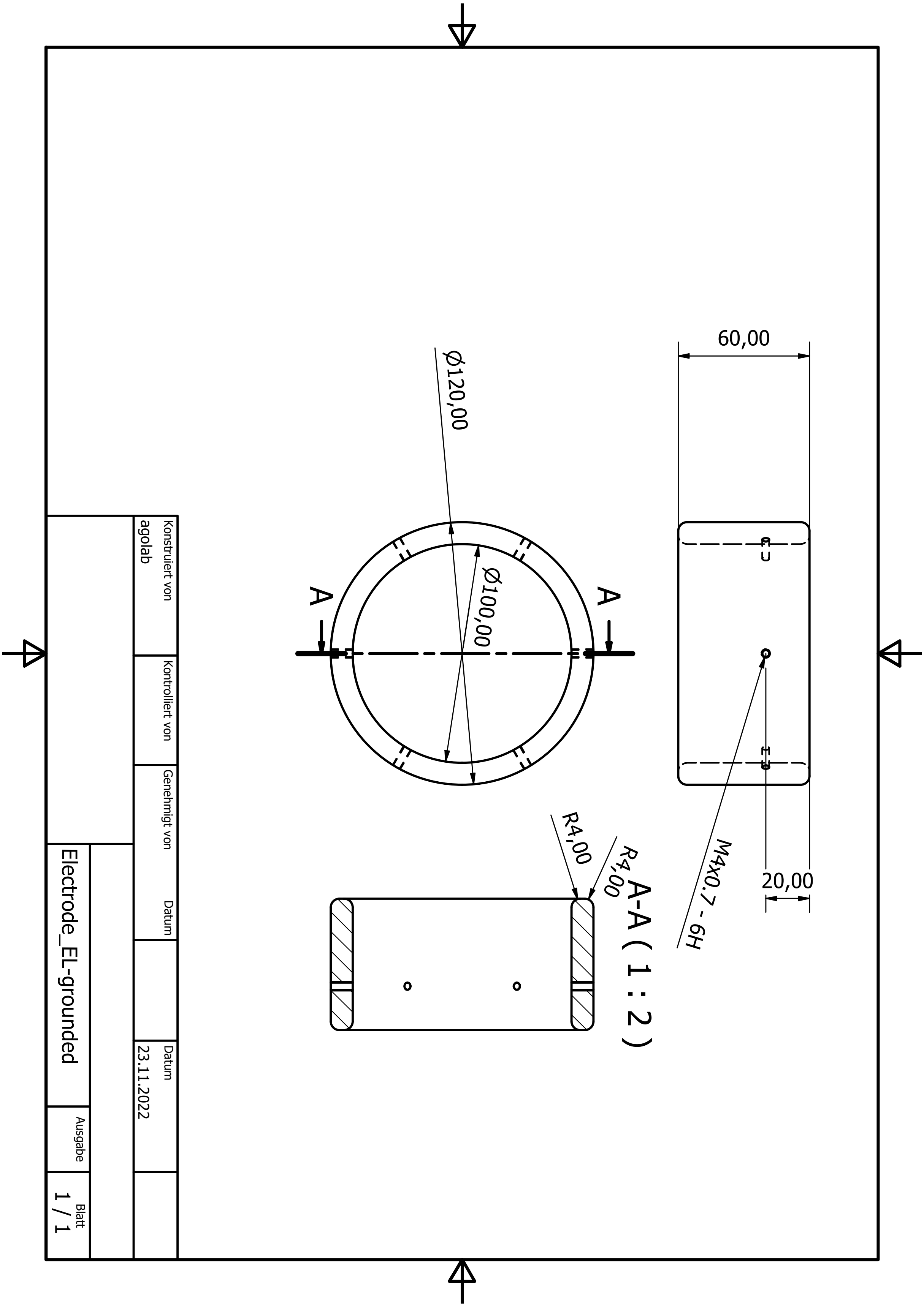
60,00
Ø120,00
Ø100,00
A
A
R4,00
R4,00
A-A (1 : 2)
M4x0.7 - 6H
20,00
Konstruiert von
agolab
Kontrolliert von
Genehmigt von
Datum
Datum
23.11.2022
Electrode_EL-grounded
Ausgabe
Blatt
1 / 1

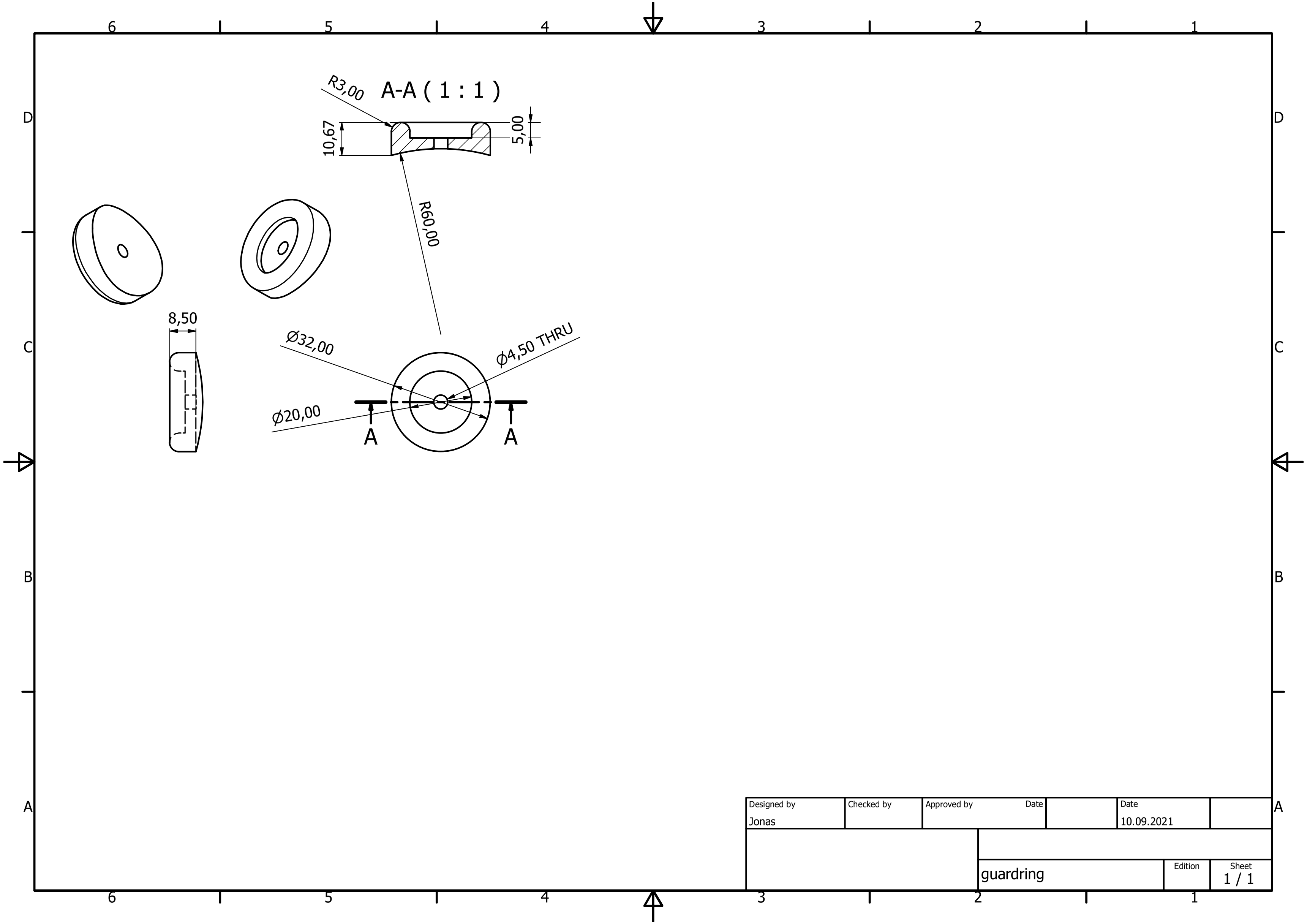
A-A (1 : 1)
R3,00
10,67
5,00
R60,00
8,50
Ø32,00
Ø20,00
Ø4,50 THRU
A
A
6
5
4
3
2
1
D
C
B
A
Designed by
Jonas
Checked by
Approved by
Date
Date
10.09.2021
guardring
Edition
Sheet
1 / 1

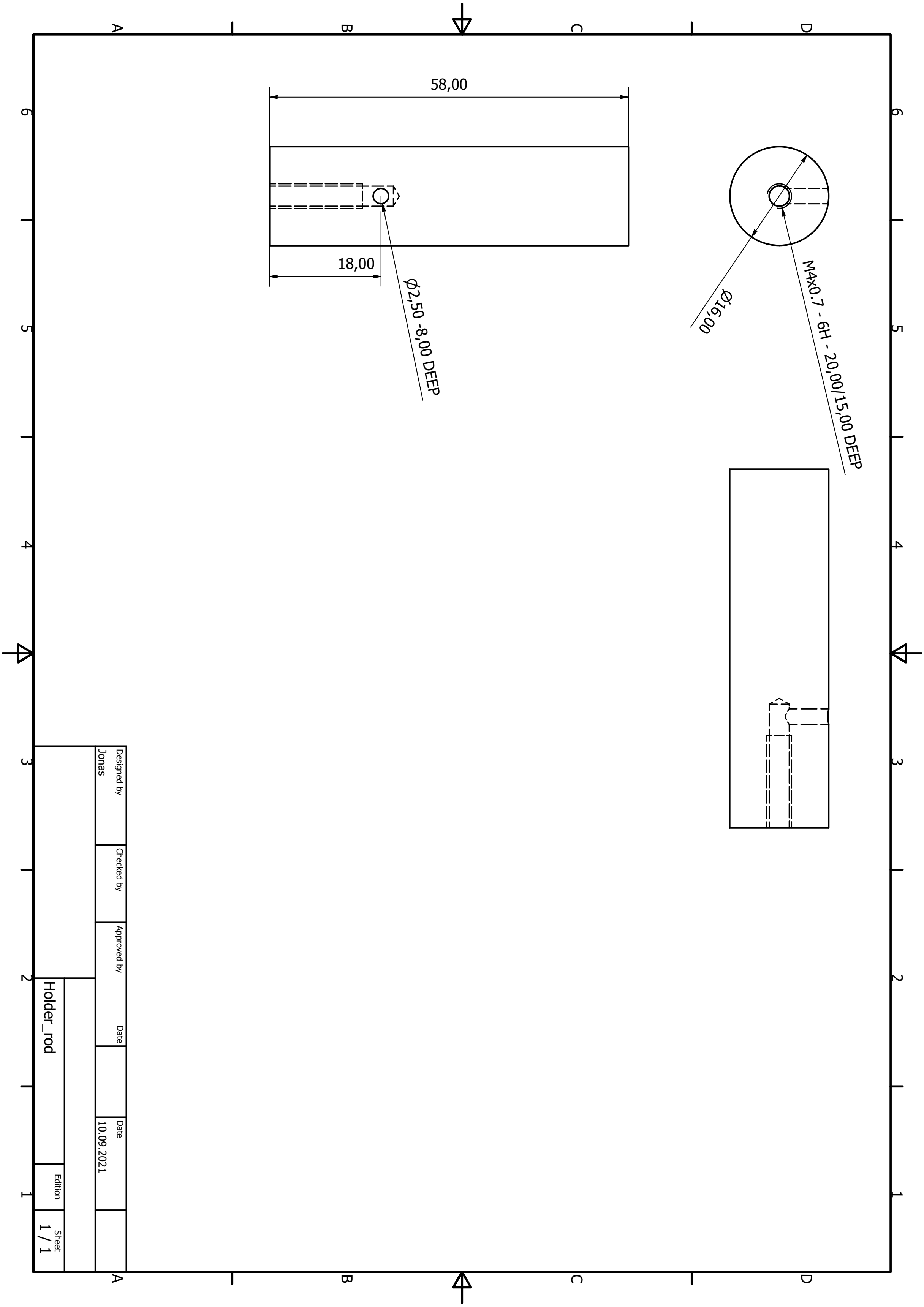

58,00
18,00
⌀2,50 -8,00 DEEP
⌀16,00
M4x0.7 - 6H - 20,00/15,00 DEEP
Designed by
Jonas
Checked by
Approved by
Date
Date
10.09.2021
Holder_rod
Edition
Sheet
1 / 1
A
B
C
D
1
2
3
4
5
6

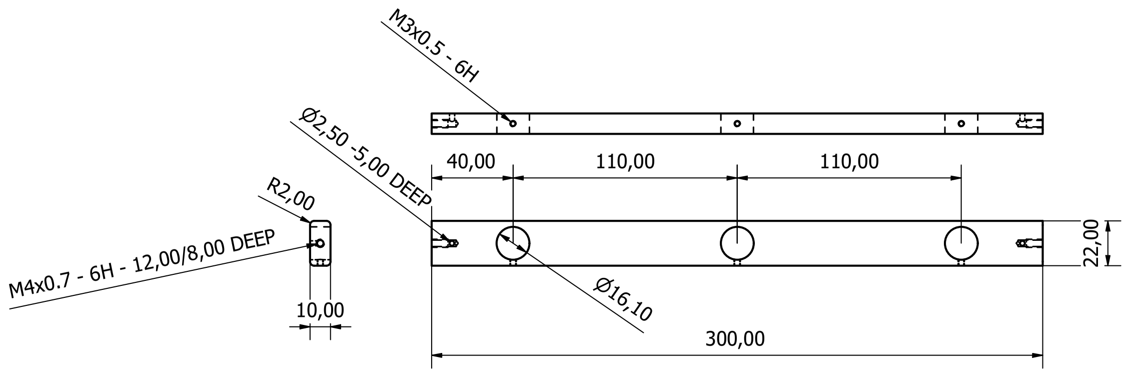

Designed by	Checked by	Approved by	Date	Date
Jonas				10.09.2021

	Edition	Sheet
holding-bar_02		1 / 1

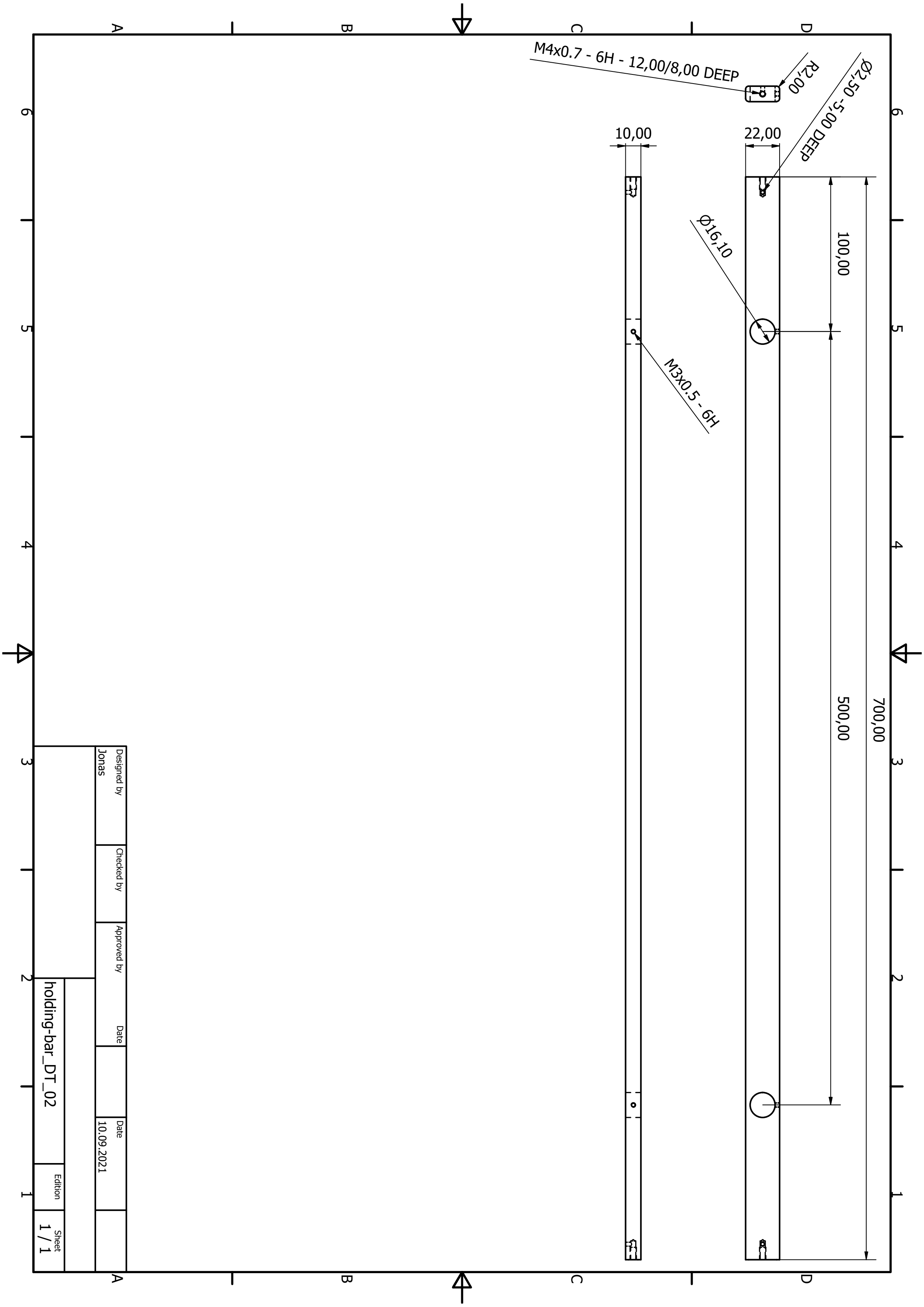
M4x0.7 - 6H - 12,00/8,00 DEEP
R2,00
Ø2,50 -5,00 DEEP
10,00
22,00
Ø16,10
100,00
M3x0.5 - 6H
500,00
700,00
Designed by
Jonas
Checked by
Approved by
Date
Date
10.09.2021
holding-bar_DT_02
Edition
Sheet
1 / 1

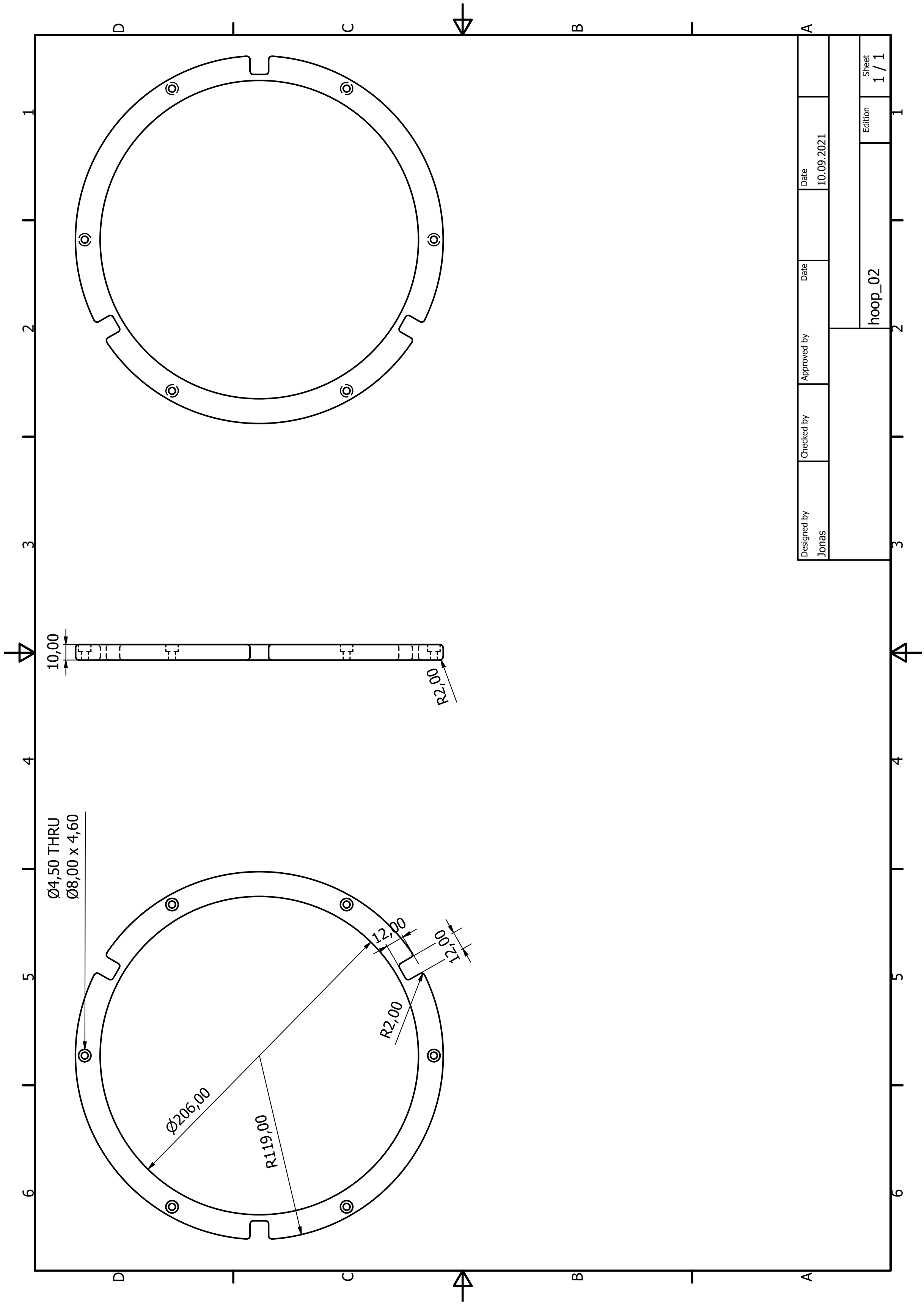
Ø4,50 THRU
Ø8,00 x 4,60
Ø206,00
R119,00
R2,00
12,00
12,00
10,00
R2,00
A
B
C
D
1
2
3
4
5
6
Designed by
Jonas
Checked by
Approved by
Date
Date
10.09.2021
hoop_02
Edition
1
Sheet
1 / 1

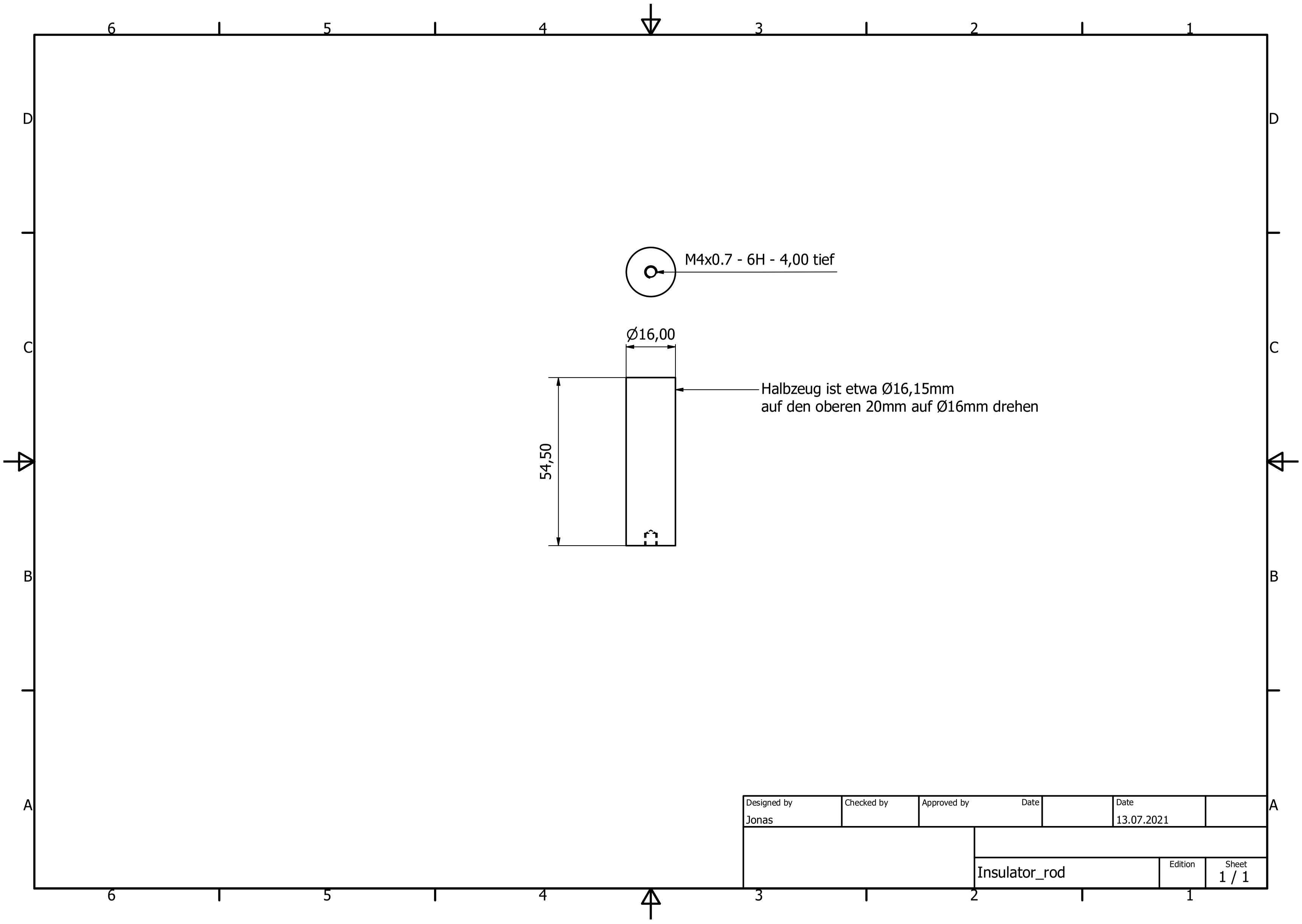
M4x0.7 - 6H - 4,00 tief
Ø16,00
54,50
Halbzeug ist etwa Ø16,15mm
auf den oberen 20mm auf Ø16mm drehen
Designed by
Jonas
Checked by
Approved by
Date
Date
13.07.2021
Insulator_rod
Edition
Sheet
1 / 1
6
5
4
3
2
1
D
C
B
A

C. Field Emission Electron Source Technical Drawings

The following drawings are of

1. source body
2. extractor
3. FEP base
4. lid
5. aperture
6. insulators

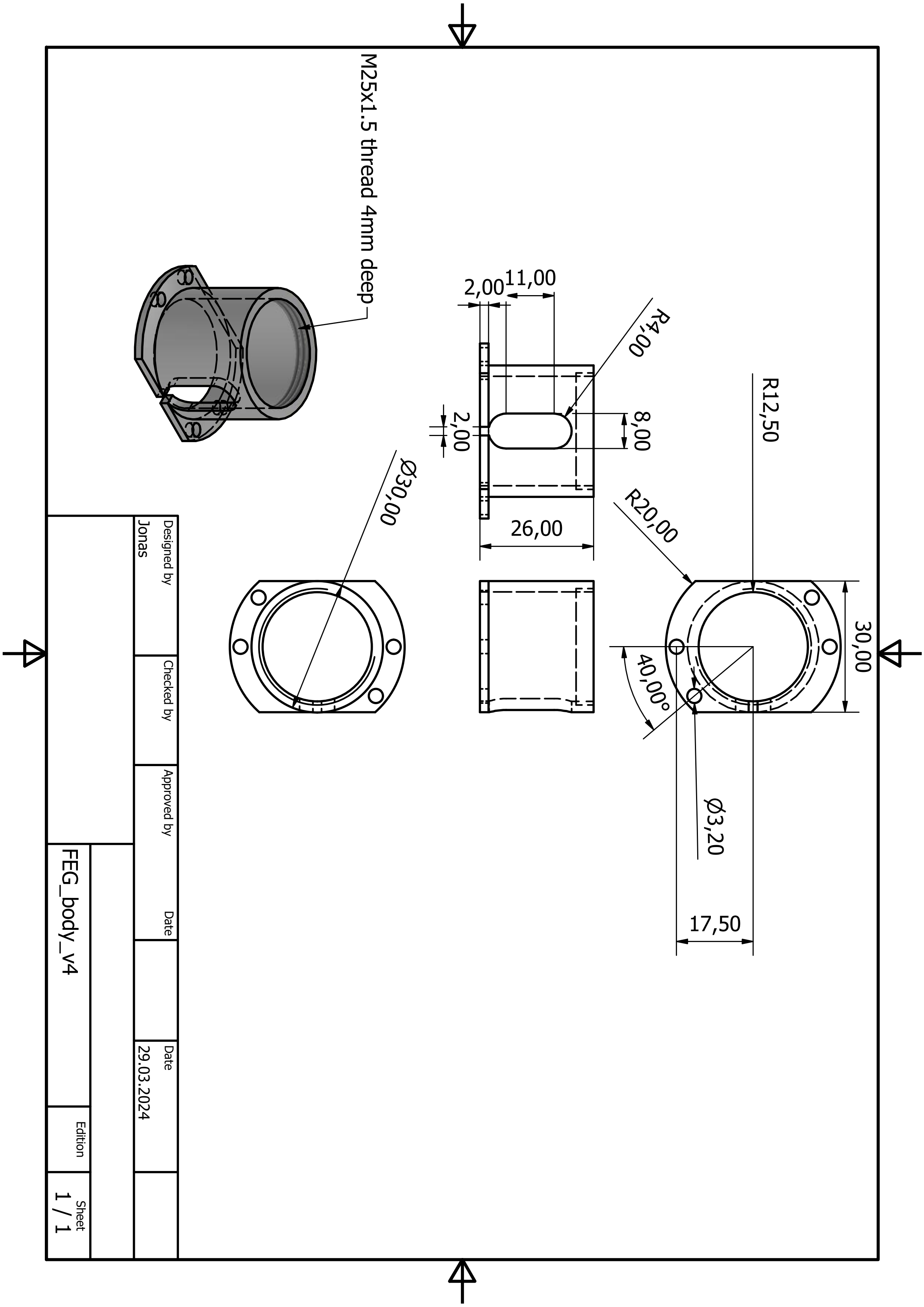
M25x1.5 thread 4mm deep
2,00
11,00
R4,00
R12,50
2,00
8,00
Ø30,00
26,00
R20,00
30,00
40,00°
Ø3,20
17,50
Designed by
Jonas
Checked by
Approved by
Date
Date
29.03.2024
FEG_body_v4
Edition
Sheet
1 / 1

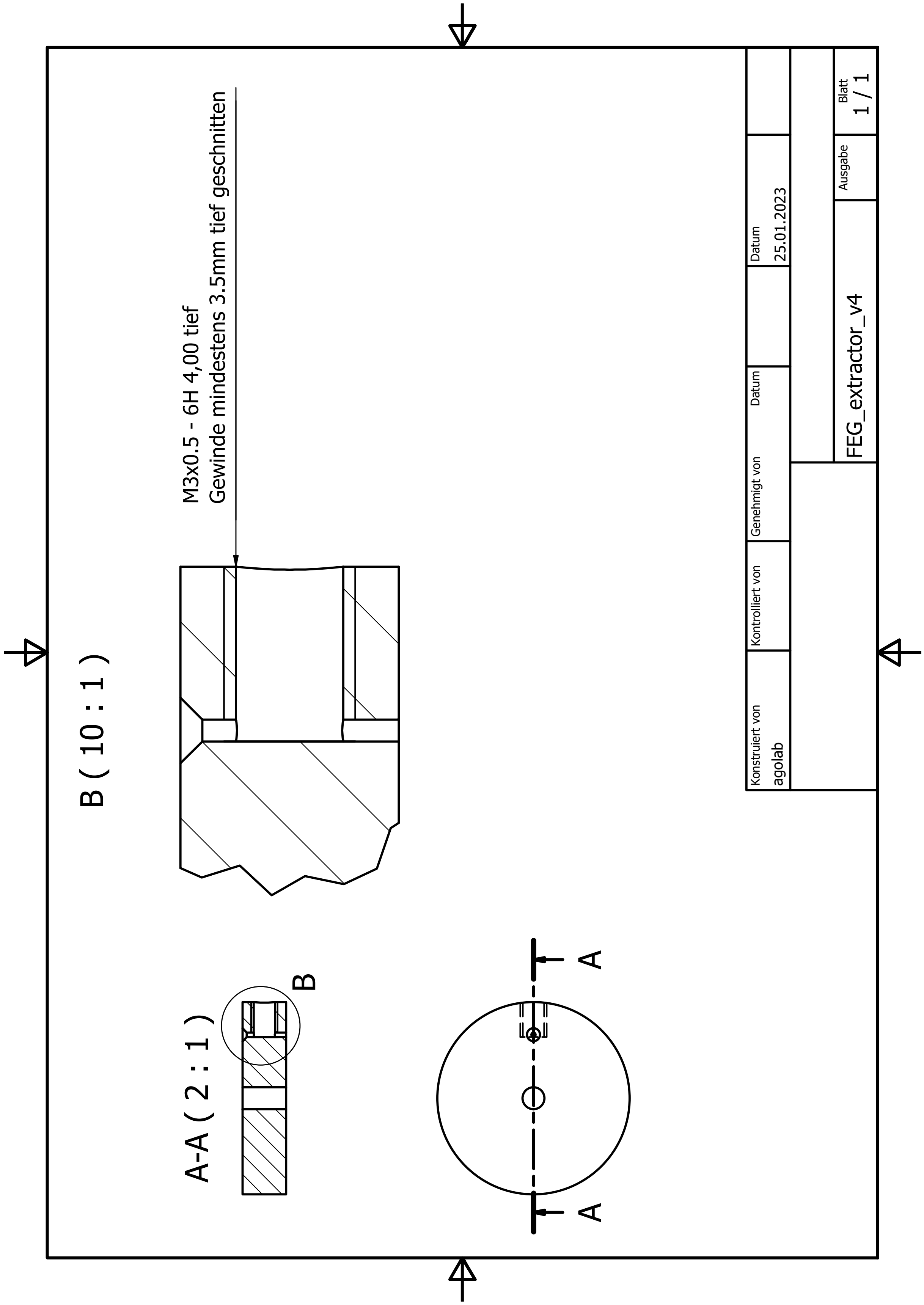
M3x0.5 - 6H 4,00 tief
Gewinde mindestens 3.5mm tief geschnitten
B (10 : 1)
A-A (2 : 1)
B
A
A
Konstruiert von
agolab
Kontrolliert von
Genehmigt von
Datum
Datum
25.01.2023
FEG_extractor_v4
Ausgabe
Blatt
1 / 1

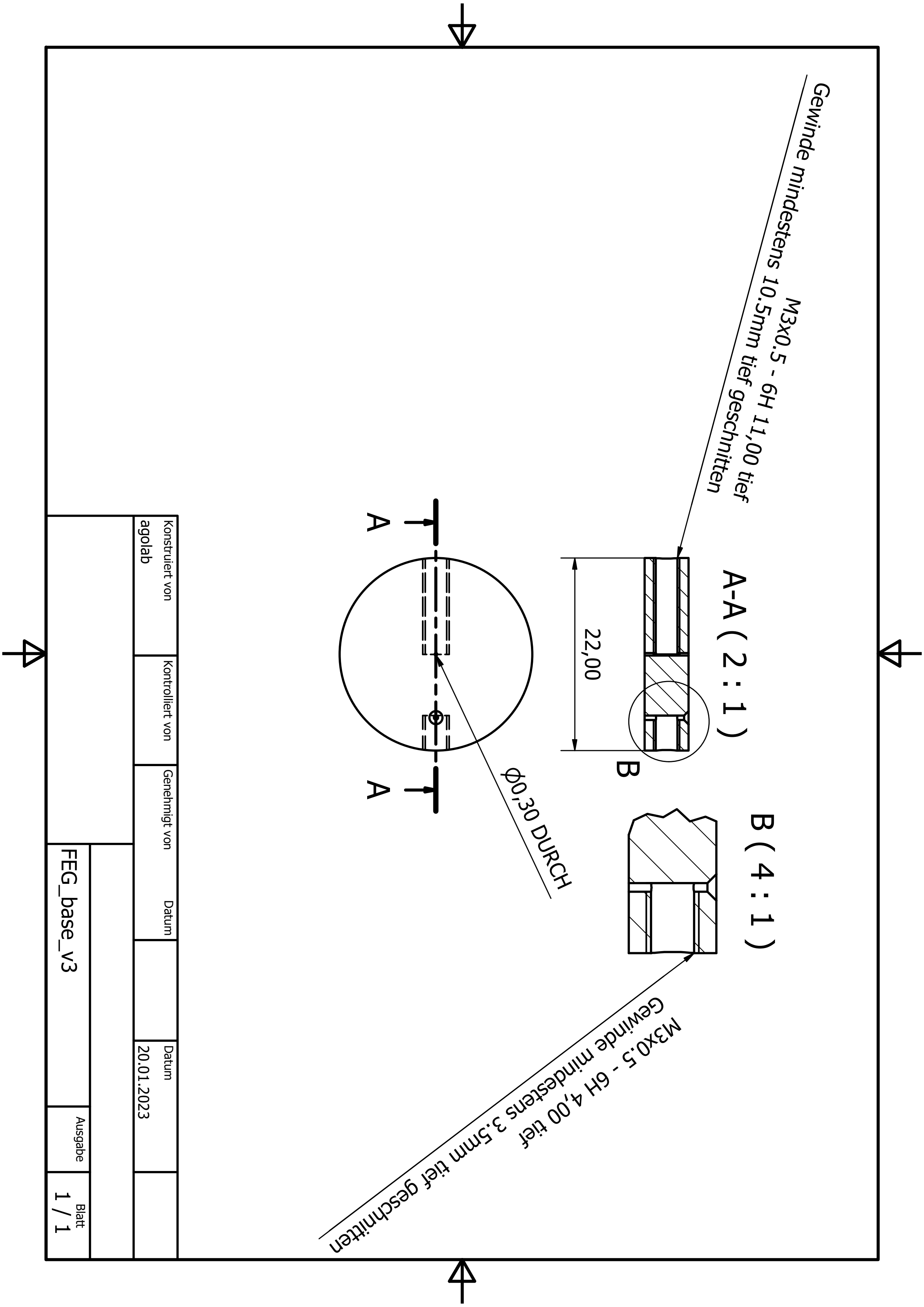
M3x0.5 - 6H 11,00 tief
Gewinde mindestens 10.5mm tief geschnitten
A-A (2 : 1)
22,00
B
B (4 : 1)
A
A
Ø0,30 DURCH
M3x0.5 - 6H 4,00 tief
Gewinde mindestens 3.5mm tief geschnitten
Konstruiert von
agolab
Kontrolliert von
Genehmigt von
Datum
Datum
20.01.2023
FEG_base_v3
Ausgabe
Blatt
1 / 1

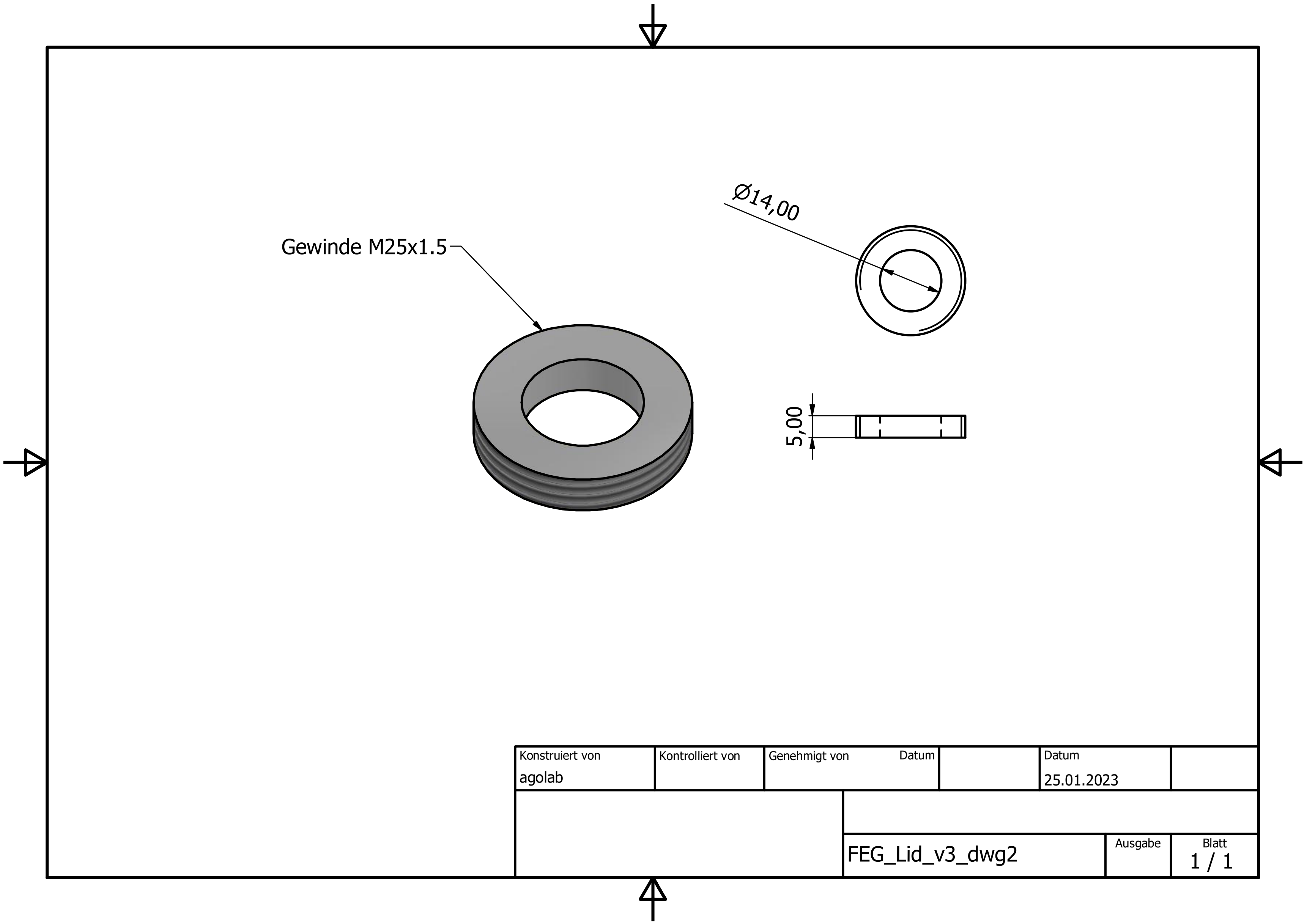

Konstruiert von agolab	Kontrolliert von	Genehmigt von	Datum		Datum 25.01.2023	
		FEG_Lid_v3_dwg2			Ausgabe	Blatt 1 / 1

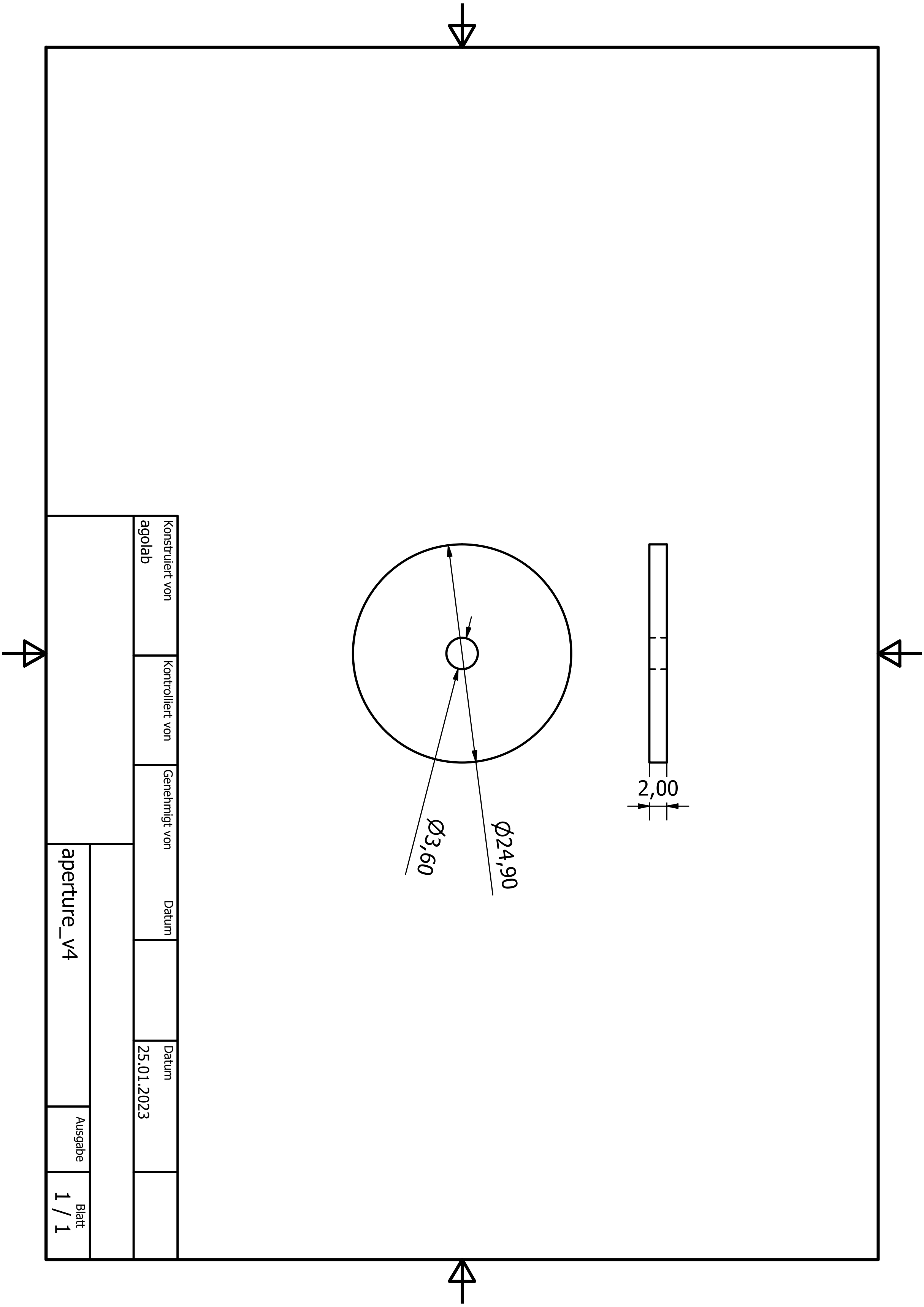
Konstruiert von
agolab
Kontrolliert von
Genehmigt von
Datum
Datum
25.01.2023
aperture_v4
Ausgabe
Blatt
1 / 1
Ø24,90
Ø3,60
2,00

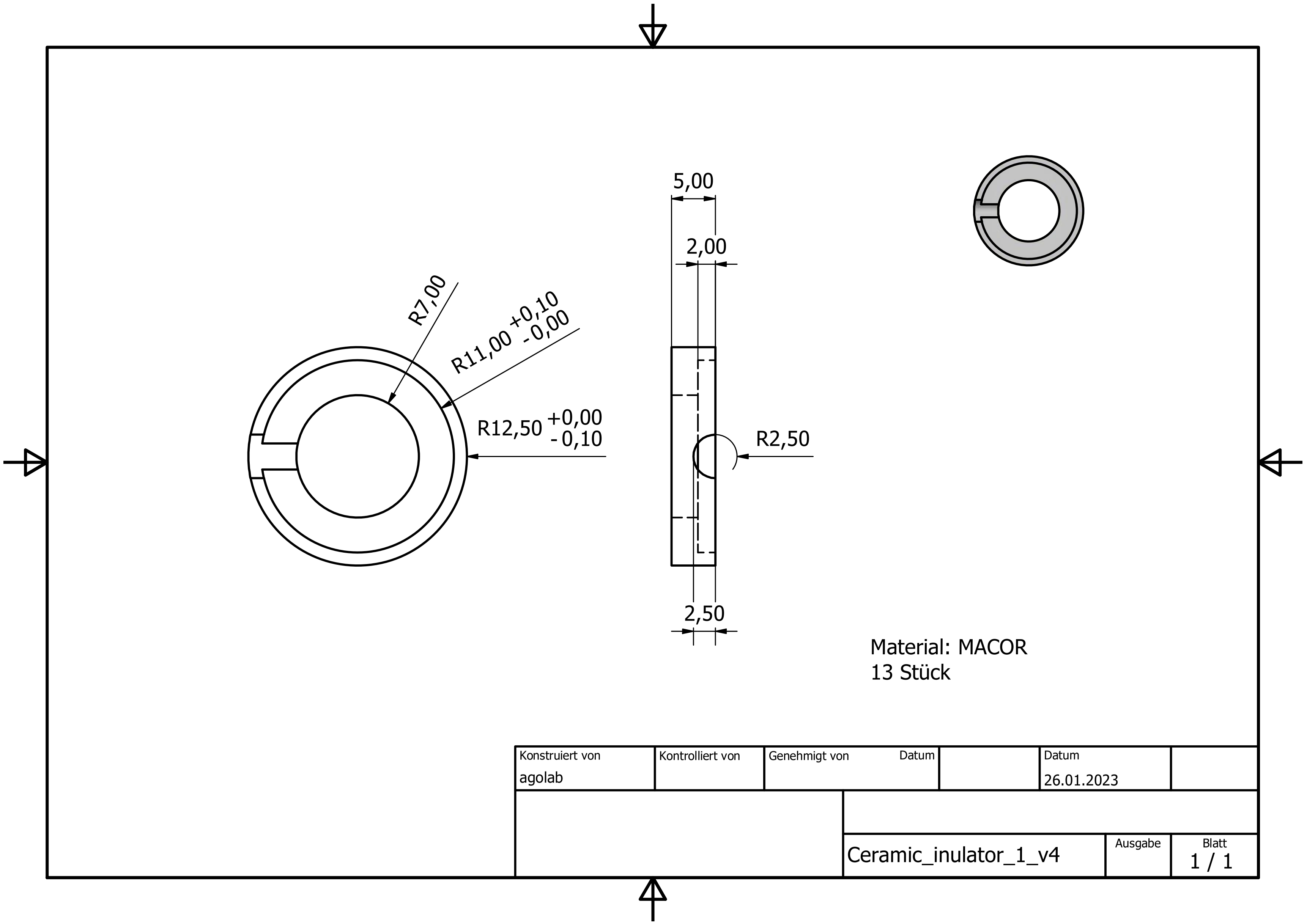
R7,00
R11,00 +0,10 -0,00
R12,50 +0,00 - 0,10
5,00
2,00
2,50
R2,50
Material: MACOR
13 Stück
Konstruiert von
agolab
Kontrolliert von
Genehmigt von
Datum
Datum
26.01.2023
Ceramic_inulator_1_v4
Ausgabe
Blatt
1 / 1

Acknowledgments

I want to thank Professor Alexandre Obertelli for the opportunity to work at CERN and for the guidance I received during my PhD. I also thank Frank Wienholtz, who was kind enough to share his knowledge with me. I thank the PUMA team, particularly Moritz Schlaich, Alexander Schmidt, Clara Klink, Ravi Sangani and Sabrina Zacarias, and my non-PUMA colleagues Simone Velardita and Christina Xanthopoulou. I want to thank Jose Antonio Ferreira Somoza for his guidance in vacuum design and Alexandre Sinturel for his help during the construction of the beamline. Finally, I thank anyone who has read this far and thereby earned my gratitude.